Ministère de l'Enseignement Supérieur et de la Recherche Scientifique
Université Hassiba Benbouali de Chlef
Faculté des Sciences Exactes et Informatique
Département de Physique

THÈSE

Présentée pour l'obtention du diplôme de

DOCTORAT EN SCIENCES

Spécialité : Physique

Par

TRAICHE MOHAMMED

Thème :

Study of thermo-photovoltaic cells based on quantum nanostructures of III-V materials

Soutenue le 30/06/2025, devant le jury composé de :

BOURAHLA Saida	Professeur	Université de Chlef	Président
RACHED Habib	Professeur	Université de Chlef	Rapporteur
BOUHANI BENZIANE Hamida	MCA	Université de Chlef	Examinateur
DERGAL Samiha	Professeur	Université de Tlemcen	Examinateur
BENTOUAF Ali	Professeur	Université de Saida	Examinateur
DJERMOUNE Mustapha	Professeur	Université de S-B Abes	Examinateur
MOKADEM Azzedine	Professeur	Université D'Oran	Invité

Abstract

In this work, we investigate the performance of a new generation of thermo-photovoltaic (TPV) cells engineered from hybrid quantum nanostructures based on III–V semiconductor materials. The main objective of our research is to exploit the synergistic integration of narrow band-gap antimonides with the unique optoelectronic properties of III–V alloys, thereby enabling ultra-broadband absorption extending from the visible to the far-infrared domain. This spectral versatility opens the pathway for significantly enhanced photoelectric conversion efficiency, surpassing the limits of conventional photovoltaic technologies. The novelty of this study lies in the nanotechnology-driven design of the active medium: by tailoring the dimensional confinement of carriers in 0D quantum dots, 1D quantum wires, and 2D quantum wells, it becomes possible to precisely control absorption, carrier transport, and thermal management. Such nanostructuration not only broadens the optical response but also enhances phonon scattering and thermal stability, key challenges in high-performance TPV systems. The proposed approach thus provides a multifunctional platform that unites photovoltaic and thermoelectric effects within a single hybrid device, this research demonstrates a pathway toward highly efficient, spectrally versatile, and thermally robust energy conversion devices, positioning hybrid nanostructured TPVs as a disruptive technology in the future of renewable and sustainable energy.

Key words:

Thermo-photovoltaic (TPV) cells, Hybrid quantum nanostructures, III–V semiconductor materials, Nanostructuration, Phonon scattering, Photovoltaic, thermoelectric effects, engineering.

الملخص

في هذا العمل، نقوم بدراسة أداء جيل جديد من الخلايا الحرارية-الفوتوفولطية المبنية على البُنى النانوية الكمية الهجينة المكوّنة من مواد شبه موصلة من عائلة المركبات III-V. يتمثل الهدف الأساسي في الاستفادة من التكامل بين الأنتيمونيات ضيقة فجوة الطاقة وما تمتلكه من خصائص فيزيائية وكيميائية فريدة لمثل هاته التطبيقات و الخصائص البصرية-الإلكترونية المتميزة للمواد المختلط III-V، وذلك من أجل تحقيق امتصاص طيفي واسع للغاية يمتد من المجال المرئي إلى الأشعة تحت الحمراء البعيدة، مما يفتح آفاقاً جديدة لرفع كفاءة التحويل الكهروضوئي بشكل يتجاوز حدود الخلايا الفوتوفولطية التقليدية. تتمثل أهمية هذا البحث على التصميم النانوي للبنية الفعالة، حيث يُمكّن التحكم في الأبعاد الكمومية ذات البعد المعدوم، البعد الواحد أو ثنائية البعد من ضبط آليات الامتصاص والنقل الإلكتروني وإدارة الخصائص الحرارية بدقة عالية .إن هذه البُنى النانوية لا تتيح فقط توسيع الاستجابة الطيفية، بل تعزز كذلك من تشتت الفونونات وثبات الخصائص الحرارية، وهي عوامل أساسية لتطوير أنظمة حرارية-فوتوطوفلطية عالية الأداء. ومن ثم، فإن هذا النهج يوفّر منصة متعددة الوظائف تجمع بين التأثيرات الفوتوفولطية والحرارية-الفولتية ضمن جهاز هجين واحد، مما يجعل الخلايا الحرارية-الفوتوفولطية النانوية الهجينة تكنولوجيا واعدة ومغيّرة لقواعد اللعبة في مستقبل الطاقة المتجددة والمستدامة.

الكلمات المفتاحية:

الخلايا الحرارية الضوئية (TPV)؛ نانوالهياكل الكمومية الهجينة؛ مواد أشباه الموصلات III–V؛ الهيكلة النانوية؛ تشتت الفونونات؛ الأثار الكهروضوئية (الفوتوفولتية)؛ الأثار الكهروحرارية ؛ الهندسة.

To my parents MOHAMMED & FATIMA

TOUSSAMA

To FATIMA & FARAH

Acknowledgment

First and foremost, I offer my deepest gratitude to God (الحمد لله), the ultimate source of strength and wisdom, for granting me the perseverance and fortitude to complete this thesis.

I wish to express my profound appreciation to the late advisor Professor Abdelkader ALI-BENAMARA (رحمه الله), may God have mercy on him, whose influence and dedication have left a lasting impact on my academic journey.

I am sincerely grateful to my advisor, Professor Habib Rached, for his generous support, timely and invaluable guidance throughout my Ph.D. studies and research, particularly during the final stages. His motivation and extensive knowledge have been instrumental, and it has been a true privilege to collaborate with him.

I would like to express my sincere gratitude to the distinguished members of the jury for their time and valuable evaluation of my work: Prof. Saida BOURAHLA (President), Dr. Hamida BOUHANI BENZIANE, Prof. Mustapha DJARMOUNE, and Prof. Ali BENTOUAF (Examiners). Your insightful comments and constructive feedback have greatly contributed to enhancing this dissertation. It is an honor to have such esteemed scholars assess my thesis.

This dissertation would not have been possible without the assistance and encouragement of many kind individuals. I extend my thanks to all my friends and colleagues from both the Faculties of Technology and Exact Sciences, as well as the faculty members of UHBC, for their continuous support.

I am deeply thankful to my family, and especially to my beloved son Oussama and my daughters Fatima and Farah, whose love and encouragement have been a constant source of strength and inspiration throughout this journey.

Finally, I am profoundly indebted to **my parents** for their unconditional love, care, and patience. Their unwavering support has made the challenges of completing my Ph.D. journey meaningful and achievable. Without their encouragement, overcoming the difficulties of these years would not have been possible.

Table of content

General Introduction 1

Chapter I: General introduction to thermoelectricity

I. Introduction 5

II. Electromagnetic radiation 5

III. Solar radiation 9

III.1. Ultra-violet radiation 10

III.2. Visible radiation 10

III.3. Infrared radiation 10

IV. Radiation-matter interaction photoelectric effect 11

IV.1. Photon detection versus thermal detection 11

V. Photo electric absorption phenomena 12

V.1 The principle of thermophotovoltaic 13

VI. Thermoelectricity 14

VI.1. Seebeck effect 14

VI.2. Seebeck coefficient with transport coefficients 15

VI.3. Electrical conductivity 17

VII. Peltier effect 18

VIII. Thermal conductivity 19

IX. Thomson effect 20

X. Thermoelectric figure of merit 21

X.1. Efficiency of thermoelectric module 24

XI. Conclusion 25

Chapter II: Nanostructuration effect interband & intersubband quantum photodetector

I. Introduction 27

II. Conventional thermoelectric materials 27

III. Nanostructured materials for thermoelectric 30

III.1. Nanowires 30

III.2. Quantum dots 31

III.2.1. Size dependence of density of state in quantum dots 31

III.3. Superlattices 33

IV. Density of states influence on opto-electric and thermoelectric nanostructured materials 33

IV.1. Density of states for different dimensions 34

V. Phonon scattering and reduced thermal conductivity 38

V.1. Phonon mean free path 38

VI. Photon detection in nanostructures superlattice 39

VII. Quantum nanostructured cascade photodetector 40

VIII. Conclusion 46

Chapter III: Thermophotovoltaique cells based on III-V materials design and simulation

I. Introduction 48

II. Properties III-V materials based antimonides 48

II.1. Structural properties 48

II.2. Electronic properties 50

II.3. Energy variation as function of temperature 52

III. Material optimization 57

III.1. Band-edge alignments 61

IV. Device design and fabrication 61

V. Schrodinger equation resolution for quantum well 63

VI. Linear optical properties of quantum wells 64

VII. Conclusion 66

Chapter IV: Characterization of quantum cascade photodetectors

I. Introduction 68

II. Energy states in a well InGaAsSb/AlGaAsSb 68

III. Nanophotonics with 2D transitions 73

III.1. Intersubband transition in conduction band 73

III.2. Light and heavy holes intersubband transition 74

III.3. Interband transitions in quantum well 76

IV. Band-edge alignments of cascade superlattice photon-absorber 77

V. Relationship between absorption and cell thickness 79

VI. The quantum multi-stage PIN cell calculation model 82

VII. Conclusion 85

General Conclusion 87

Bibliography 91

List of figures

Figure I.1: Blackbody radiation curves for different temperatures (T = 300 K, 400 K, 500 k, 600 k and 700 K) based on Planck's law. 08

Figure I.2: Distribution of solar radiation across different wavelengths "American Society for Testing and Materials" ASTM G173-03 Reference Spectra. 09

Figure I.3: Photon absorption in direct and indirect bandgap semiconductor. 12

Figure I.4: Seebeck effect for thermoelectric material. 14

Figure I.5: Variation of Seebeck coefficient S (μV/K) as function of temperature T (K), for different kind of materials Semiconductor PN and metal. 16

Figure I.6: Peltie effect for PN junction. 19

Figure I.7: Coupled seebeck and peltier effect in one module used for power generation and cooling generation. 21

Figure I.8: Carrier concentration Log10 (n, p). 22

Figure II.1: Figure of merit as a function of temperature of various conventional thermoelectric materials and nanostructured materials. 28

Figure II.2: A coupled nanowire photodetector and photoemitter based on III-V materials Using template-assisted selective epitaxy TASE. 31

Figure II.3: Shows how size of quantum dots affects electronics and optoelectronics proprieties. 32

FigureII.4: Density of states (DOS) as a function of energy for different material dimensions: 3D-bulk materials, 2D-quantum wells, 1D-nanowires or nanotubes, 0D-quantum dots, and temperature dependency. 36

Figure II.5: Contrast between conventional thermoelectric materials and nanostructured materials as function of temperature. 37

Figure II.6: Working principle of solar cell with p-n junction structure and (b) loss mechanism in standard p-n junction. 39

Figure II.7: Strategies to enhance thermoelectric performance by engineering the band structure of alloyed host materials to reduce the energy disparity between light and heavy carrier bands, hence improving Seebeck coefficients and power factors.can be executed on either the valence band or conduction band, respectively, for p-type and n-type carriers. 40

Figure II.8: Illustration of the photon absorption and cascading effect in an interband cascade photodetector figure from. 41

Figure II.9: The schematic diagram for finite quantum well type-I a) illustrations of permitted Intersubband and Interband transitions b) the density of states for Intersubband and Interband transitions. 42

Figure II.10: The variation of Auger recombination and SRH (Shockley-Read-Hall) recombination as a function of the quantum well width at different temperatures. 44

Figure III.1: Zinc blende crystal structure of GaSb. 49

Figure III.2: Variation of total energy versus volume of unit cell volume for GaSb. 50

Figure III.3: Variation of total energy versus volume of unit cell volume for InSb. 51

Figure III.4: Band diagram and density Of State for GaAs, InAs, GaSb and InSb. 52

Figure III.5: Variation of the Energy gap as function of temperature variation. 53

Figure III.6: a) Temperature dependence of Seebeck coeficient in GaSb b) Temperature dependence of mobility in GaSb. 54

Figure III.7: Band position of GaAs, InAs, InSb, and GaSb binary systems, the values are obtained from Ref. cited in the table bellow. 55

Figure III.8: Calculation of the AlxGa1-xAsySb1-y /In0.2Ga0.8AsxSb1-x maille parameter as function of composition. 57

Figure III.9: Variations of the gap energy as a function of x (% In) and for different y (% As). 59

figure III.10: Variations of the gap energy as a function of x (% Al) and for different y (% As). 60

Figure III.11: Structure of a pin thermophotovoltaic solar cell with multi quantum wells using cascade nanostructure for photovoltaic cell and micro cascade structure to improve thermoelectric conversion. 62

Figure IV.1: The level of confinement in the conduction band as a function of the width of the well for the quaternary InGaAsSb / AlGaAsSb. 69

Figure IV.2: The level of confinement in the valence band as a function of the width of the well for the quaternary InGaAsSb / AlGaAsSb. 70

Figure IV.3: The level of confinement in the conduction band and in the valence band, as a function of the well width and of the level of confinement ΔEC and ΔEV for the quinary InGaAsNSb / AlGaAsSb, for two different concentrations. 71

Figure IV.4: External quantum efficiency (EQE) of maximum power conversion efficiency that a QCD can achieve for optimal transitions as a function of the QW width for the case of $In_{0.2}Ga_{0.8}As_{0.45}Sb_{0.55}/Al_{0.45}Ga_{0.55}As_{0.3}Sb_{0.7}$. 72

Figure IV.5: Intersubband transitions in conduction-confined energies for electrons as function of barrier thicknesses at 300 K. 74

Figure IV.6: Intersubband transitions in valence-confined energies for heavy and light holes as function of barrier thicknesses at 300 K. 75

Figure IV.7: Interband transitions between different confined subband states of CB and VB as a function of QW width at 300 K. 76

Figure IV.8: Self-consistently calculated conduction band structure of three QC 2D nanostructure with different z and the magnitude squared wave function for each sub bands in active region is illustrated. 78

Figure IV.9: Self-consistently calculated conduction band structure of multiple QW of a QC structure for one full period, surrounded by adjacent parts of barriere. 78

Figure IV.10: Calculated signal current and photocurrent as function of width which is represented by number of stages. 80

Figure IV.11: Calculated conversion efficiency vs normalized absorber thickness for different values of αL with an incident power density equal 50 W/cm^2. 81

Figure IV.12: comparison of the J–V characteristics of a conventional PV and TPV under various temperature differences (ΔT). 83

Figure IV.13: The comparison of the calculated output power for a simple summation of the PV and and QCPD's TPV as a function of (ΔT). 84

List of tables

Table II.1 Figure of merit ZT for different materials. 29

Table II.2 Electronic density of states of semiconductors with 3, 2, 1, and 0 degrees of freedom for electron propagation. 34

Table III.1: Survey of thermophotovoltaic technologies grouped according to absorber material. 56

Figure III.2: The scheme of the layer's composition in the investigated samples. 61

List of Symbols

$\vec{E}$ Electric field.

$\vec{B}$ Magnetic field.

ρ Charge density.

J Current density.

ϵ_0 Permittivity of free space.

μ_0 Permeability of free space.

h Planck's constant (6.626×10^{-34} J·s).

c The speed of light.

λ Wavelength.

k_b Boltzmann constant.

T Temperature (k)

T_{amb} Ambient temperature.

A surface area.

σ_{sb} Stefan-Boltzmann constant.

ASTM American Society for Testing and Materials.

k wave vector.

PV PhotoVoltaic.

TPV ThermoPhotoVoltaic.

q: Charge of the carrier.

$\sigma\ (E)$: Energy-dependent electrical conductivity.

$f(E)$ Fermi-Dirac distribution function.

E_F fermi level energy.

S Seebeck coefficient.

S_{ab} is the thermoelectric power of a couple.

$f_0(\varepsilon_k)$ is the Fermi–Dirac distribution function.

ε_k band energy at k-point.

v_k the group velocity.

τ_k relaxation time due to scattering with phonons and/or disorders/impurities.

Z is the atomic number.

π_{ab} Peltier coefficient of a couple.

κ Thermal conductivity.

κ_e Electrons thermal conductivity.

κ_l Lattice thermal conductivity.

L Lorentz factor.

m^* Effective mass.

τ Thomson factor

zT figure-of-merit.

PF Power Factor.

DOS density of state.

m_0 mass of the electron.

E_g gap energy.

QD Quantum dots.

NW NanoWire.

QW Quantum Well.

C_v specific heat capacity per unit volume.

v_v speed of phonon vibration.

τ_{carrier} the carrier lifetime.

QWIP Quantum Wells Infrared Photodetector.

QCD Quantum Cascade Detectors

τ_{auger} Auger recombination.

τ_{SRH} Shockley-Read-Hall (SRH) recombination.

φ_n stationary states.

$\hat{H}$ Hamiltonian operator.

L_z: the width of the well.

ΔE_C conduction offset band.

ΔE_V valence offset band.

α_{2D} 2D absorption coefficient.

n_s the active QW's 2-D doping density.

n is the refractive index of the QCD.

φ_n the function of the position along the growth direction $\mathcal{Z}$.

Γ the half-width of the intersubband transition's Lorentzian absorption shape.

HH heavy hole.

LH light hole.

W_c the active region cell thickness.

A_{opt} the optical area of the device.

QE_m the effective quantum efficiency in the N_{th} stage.

T_{fs} is the front-side temperature.

T_{bs} is the back-side.

USL ultimate limits state.

G_{op}: optical generation current.

G_{th}: thermal generation current.

A_{cnr}: non radiative coefficient generation.

J_G Generation current.

J_R Recombination current.

V_d The diffusion voltage.

V_{oc} Open-circuit voltage.

J_{sc} short-circuit current.

N_C the state density of electrons of the conduction band.

N_V the state density of holes of the valence band.

τ_c the lifetime of the carriers.

τ_{tr} the transition time.

p_e is the amount of movement necessary for the carriers to cross the active zone.

GENERAL INTRODUCTION

GENERAL INTRODUCTION

Current challenges to combat global warming, and to preserve the quality of the air we breathe by reducing carbon emissions and lowering greenhouse gas emissions, by generating power using solar energy, which is cleaner and more ecologically friendly alternative to generating power using fossil fuels or nuclear energy, which emit enormous amounts of carbon dioxide CO_2 and other pollutants into the atmosphere. So, the new solar technologies on the horizon promise to increase solar energy utilization by lowering costs and enhancing efficiency. In doing so, it not only lessens reliance on fossil fuels but also safeguards the environment. With the largest solar potential in the Mediterranean, Algeria boasts some of the world's highest solar resources due to its geographic position and high sunshine rate abroad huge area especially uninhabited area such as sahara.

Our goal is to improve photovoltaic solar cell performance by broadening the absorption spectrum of solar radiation not only by absorbing visible radiation but also by absorbing the low energy domain from Near Infrared (NIR) to Mid-Infrared (MIR) and Far Infrared (FIR), which represent about 45% of the total spectrum of solar energy that reaches the ground, traditional solar cells perform extremely badly or not at all in this spectrum.

To that end, we suggest designing thermo-photovoltaic solar cells that utilize three separate and complementary methods for conversion:

1. Photovoltaic Generator (PG) it is direct optical absorption of the maximum of photons emitted by the sun, photons carrying just the right energy are absorbed by trapped electrons by using nanostructured materials, this absorption will be guaranteed.
2. Thermoelectric Generators (TG) Indirect thermal absorption this process takes place due to the thermoelectric qualities, The energy conversion efficiency of thermoelectric devices is primarily determined by the dimensionless figure of merit (ZT) of thermoelectric materials, which includes both electrical and phonon transport features. the investigation of high figure of merit thermoelectric materials continues to rely heavily on experimental efforts. These thermoelectric processes are also employed to absorb the energy released in the form of phonons by the hot carriers of high photo energy formed in the cell, which have generally

negative consequences in traditional photovoltaic cells: heating phenomena that degrade performance, specifically, the extremely strong thermoelectric power of the antimonide materials involved.

3. Investigate the thermoelectric properties of nanostructured materials, the limitations in efficiency are understood by considering several important practical factors. These factors are identified to be closely associated with a short carrier lifetime, high dark saturation current density, small absorption coefficient, and limited diffusion length. But with the appearance of nanostructured materials, we can achieve high figures of merit (ZT) by reducing thermal conductivity while retaining or increasing electrical conductivity and the Seebeck coefficient. Numerous synthesis and characterization approaches to create and tune nanostructures to improve thermoelectric performance are employed.

Narrow bandgap materials are commonly used in conventional photodetectors, which detect infrared light by interband absorption. In this study we will focus on intersubband photodetectors using III-V compound semiconductors with mixing materials those with a larger bandgap was spurred by the difficulties associated with the creation and processing of materials with small band gaps. To create confined energy states in the device's valence or conduction bands or both, quantum wells (QWs) or quantum dots (QDs) integrated into materials with larger bandgaps are used. Infrared detection depends on the excitation of carriers from occupied energy levels in the conduction or valence band to unoccupied levels within the same band. The active area of the device is doped to provide free charge carriers. So, we must arrange them in nanometric quantum heterostructures composed of successions of wells and quantum barriers that generate the energies required for radiation absorption as well as the potentials.

Despite being sensitive to normal incidence radiation, p-type Quantum well infrared photodetectors (QWIPs) show minimal absorption. QWIPs made from indirect bandgap n-type semiconductors have been studied to address this limitation. AlAs/AlGaAs multiple quantum wells (MQWs) on oriented substrates have been successfully used to create QWIPs, which operate in the 5–20 μm range. Al-free material systems avoid oxidation, high temperature growth requirements, deep-level defects, and other processing issues associated with Al-containing materials. For quantum well infrared photodetectors (QWIPs), the following GaSb-based, material have been studied.

The first chapter will be devoted to understanding the basic concepts of photovoltaic energy conversion, as well as the three thermoelectric effects and an overview of the diverse applications of thermoelectric materials. We will introduce the figure of merit and the essential parameters to be managed in order to obtain high conversion efficiency.

The second chapter will offer a brief explanation of thermoelectric materials, as well as the general properties of III-V materials, and the synthesis methods will be summarized. The last portion of this chapter will focus on new research methodologies targeted at increasing their thermoelectric performance.

Chapter three will present the research of the crystal structure of antimony-based III-V compounds. Subsequently, we will explore the stability of these materials at the nanoscale, as well as the influence of nanostructuring and the engineering of this technique on the thermoelectric properties of the proposed compounds. We will present the cascade structure and its advantages for boosting photoelectric and thermoelectric detection and conversion performance.

The fourth chapter, emphasis advanced photodetectors that rely on quantum engineering of the electronic band structure to detect photons with energies below the semiconductor bandgap, succeeding photon detection across a wide spectral range—from the visible to the infrared—making them ideal for innovative technological applications. we analyze the optoelectronic and thermoelectric properties of QCDs, including interband and intersubband transitions, lattice thermal conductivity, and electronic transport characteristics.

Chapter I

General introduction to thermoelectricity

I. Introduction

The interaction between radiation and matter plays a fundamental role in numerous fields of science and technology, spanning several major domains of physics. Depending on the type and energy of the radiation, as well as the physical properties of the material it encounters, radiation can undergo various interaction mechanisms. These interactions may involve energy transfer, particle creation or annihilation, absorption, scattering, or attenuation. Their description often relies on classical physics laws, but many advanced applications require a unified treatment that combines concepts from quantum mechanics and electromagnetic theory. Such a framework is essential for predicting and understanding how radiation behaves in different materials [1].

In this chapter, however, we will limit our attention to those interactions that lead primarily to energy transfer in the form of heat or electrical power. Particular emphasis is placed on the mechanisms by which absorbed energy is converted into usable electrical energy an effect that forms the basis of thermoelectric phenomena [2]. Previous studies have attempted to correlate thermoelectric power with temperature, often relying on complex models [3]. Our goal here is to present a clear and accessible foundation for understanding the physical principles governing thermoelectricity. This chapter is structured as follows:
First, we provide a brief historical overview of the discovery of thermoelectric effects. Next, we describe the three fundamental thermoelectric phenomena. We then introduce the basic operating principles of thermoelectric devices and generators. Finally, we outline the key criteria for selecting efficient thermoelectric materials, which will serve as a basis for the following chapters.

II. Electromagnetic radiation

Electromagnetic radiation (EMR) denotes to the energy propagated as electromagnetic waves. These waves are characterized by electric and magnetic fields, there exist an immense range of wavelengths with different frequencies, the electric field (E) and the magnetic field (B) oscillate perpendicular to each other and to the direction in which the wave propagates, they are synchronized to be always perpendicular. The electromagnetic radiation is ruled by the fourth fundamental equations of Maxwell, these equations are:

Maxwell-Gauss's equation for electric field: this rule describes the relationship between a static electric field ($\vec{E}$) and the electric charges that produced by $\vec{E}$.

$$\nabla\vec{E} = \frac{\rho}{\epsilon_0} \qquad \text{I.1}$$

Maxwell-Thomson's Law for magnetic field: this rule demonstrates that the total magnetic flux through any closed surface is zero, or that the magnetic field is a solenoidal field, so the magnetic field is generated by a configuration called a dipole, which has no magnetic charge.

$$\nabla\vec{B} = 0 \qquad \text{I.2}$$

Maxwell-Faraday's Law of Induction: Explains how a changing magnetic field induces an electric field.

$$\nabla\vec{E} = \frac{\partial\vec{B}}{\partial t} \qquad \text{I.3}$$

Maxwell-Ampère's Law (with Maxwell's correction): Describes how a variation of magnetic field creates an electric field, and how the variation of an electric field creates a magnetic field. Therefore, these equations allow for the circulation of self-sustaining electromagnetic waves.

$$\nabla\vec{E} = \mu_0\vec{J} + \mu_0\epsilon_0\frac{\partial\vec{E}}{\partial t} \qquad \text{I.4}$$

Where:

$\vec{E}$ is the electric field

$\vec{B}$ is the magnetic field

ρ is the charge density

J is the current density

ϵ_0 is the permittivity of free space

μ_0 is the permeability of free space

Maxwell's equations lead to the understanding that both the electric and magnetic fields of an electromagnetic wave satisfy the wave equation, and these fields oscillate in phase with each other.

The magnitude of the electric field ($\vec{E}$) and magnetic field ($\vec{B}$) are related by:

$$|E| = c|B| \qquad \text{I.5}$$

This relationship indicates that the strength of the electric and magnetic components of the wave is proportional, with c representing the speed of light in a vacuum.

The intensity (I) of an electromagnetic wave refers to the power per unit area carried by the wave, and it can be expressed as:

$$I = \frac{1}{2}\epsilon_0 c E_0^2 \qquad \text{I.6}$$

Where E_0 is the amplitude of the electric field. Intensity is directly proportional to the square of the electric field amplitude, meaning stronger electric fields result in higher intensity.

The behavior of an electromagnetic wave, specifically the electric field $\vec{E}$, is given by the following wave equation:

$$\nabla^2 \vec{E} - \frac{1}{c^2}\frac{\partial^2 \vec{E}}{\partial t^2} = 0 \qquad \text{I.7}$$

Here, $\boldsymbol{\nabla^2}$ represents the Laplacian (spatial derivatives), and the term $\frac{\partial^2 E}{\partial t^2}$ is the second derivative of **E** with respect to time. This equation captures how the electric field oscillates and propagates through space.

In general, objects emit electromagnetic radiation only if his temperature is higher than zero. Ideally, the spectral radiance follows Planck's law. In this case, the power emitted of the object is similar of the power of a blackbody given by [06]:

$$P_\lambda(\lambda, T) = \frac{2hc^2}{\lambda^5}\frac{1}{exp\left(\frac{hc}{\lambda k_b T}\right)-1} \qquad \text{I.8}$$

h is the Planck's constant, c is the speed of light, λ is wavelength, k_b is Boltzmann constant, and T is the temperature (k).

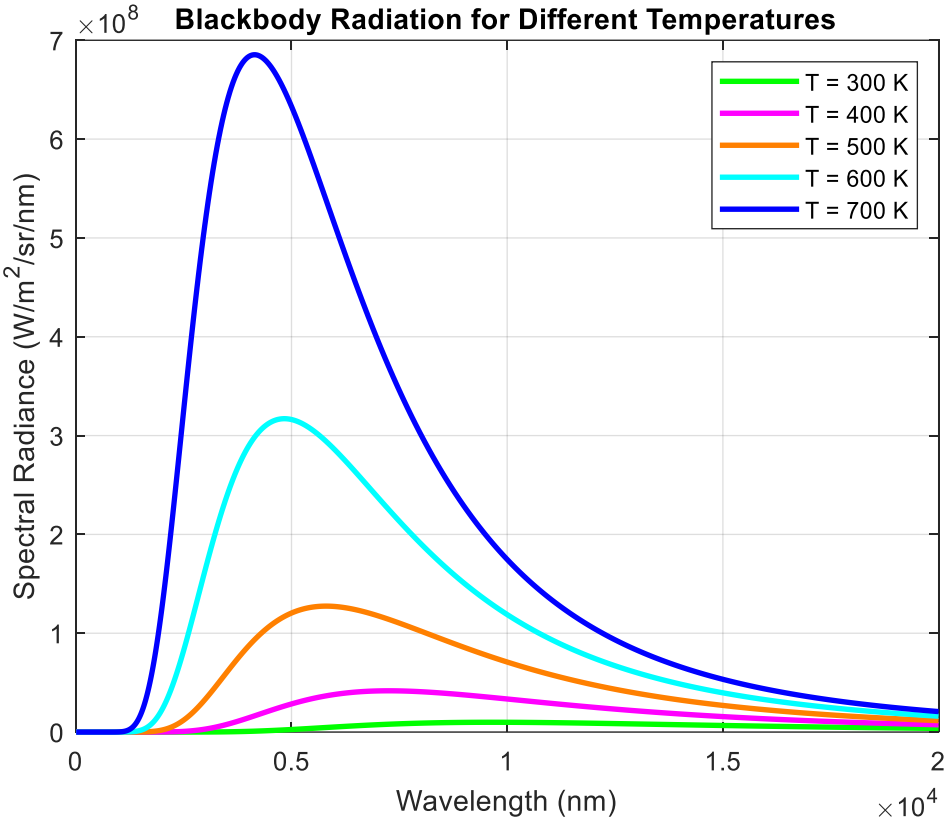

Figure I.1: Blackbody radiation curves for different temperatures (T = 300 K, 400 K, 500 k, 600 k and 700 K) based on Planck's law.

The graph shows the variation of spectral radiance emitted by blackbody as a function of wavelength for a given temperature. We observe that the Peak Wavelength Shifts Left as Temperature Increases, when the temperature was higher than the ambient temperature the power of the object, can be obtained by integrating Planck's radiation formula:

$$\frac{P}{A} = 2hc^2\left[\int_0^{\infty}\frac{d\lambda}{\lambda^5 exp\left(\frac{hc}{\lambda k_b T}\right)-1} - \int_0^{\infty}\frac{d\lambda}{\lambda^5 exp\left(\frac{hc}{\lambda k_b T_{amb}}\right)-1}\right] \qquad \text{I.9}$$

where A is the surface area and T_{amb} is the ambient temperature. This function is calculated by Stephan Boltzmann for a black body radiation and the final form written as:

$$\frac{P}{A} = \sigma_{sb}(T^4 - T_{amb}^T) \qquad \text{I.10}$$

Where σ_{sb} is the Stefan-Boltzmann constant.

III. Solar radiation

Solar radiation is made up of electromagnetic waves of very different natures, UV radiation mostly absorbed by the upper atmospheric layers only about 6% reach the surface of the earth, somewhere visible radiation represents approximately 47% of the solar spectrum, but also photons which are less energetic and which are located in infrared range represent approximately 45% of the solar spectrum. An important feature of infrared radiation is that it is mostly absorbed out by water vapor and carbon dioxide in the atmosphere in front of the earth surface, as shown in Figure 02.

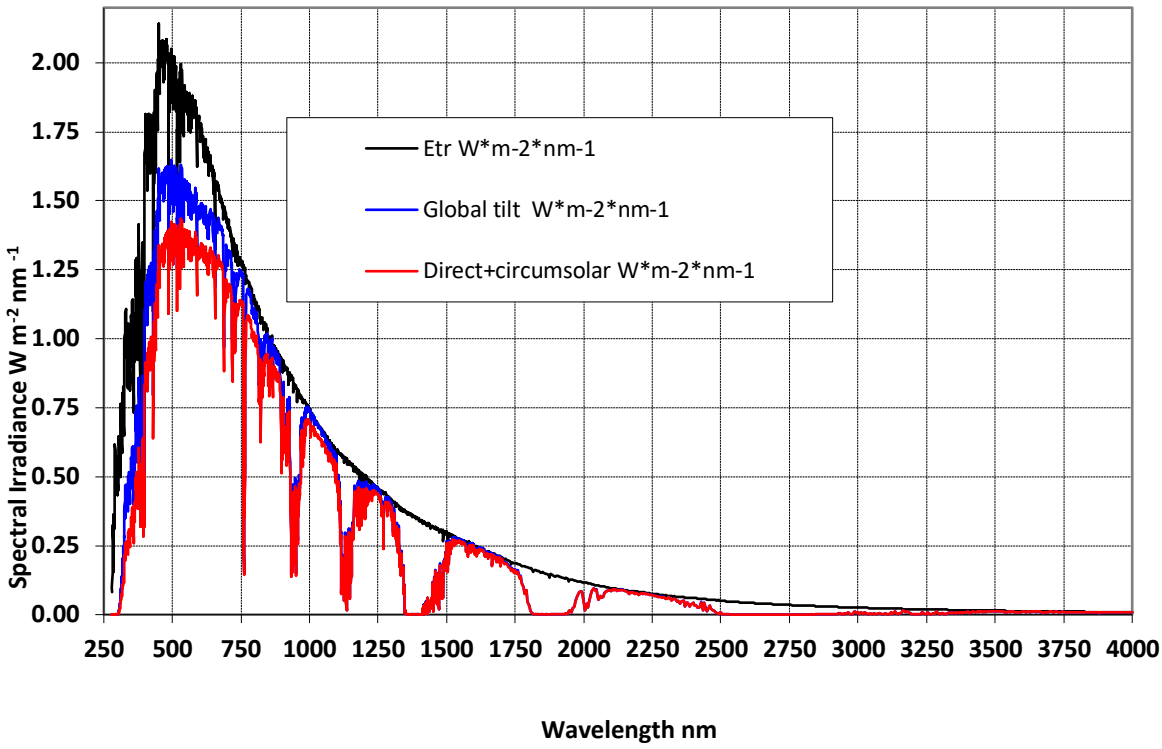

Figure I.2: Distribution of solar radiation across different wavelengths

"American Society for Testing and Materials" ASTM G173-03 Reference Spectra

The electromagnetic spectrum in figure 02 refers to the full range of possible light frequencies of electromagnetic radiation.

The Energy of electromagnetic wave is a function of wave length given by the relation

$$E = h\,{}^{c}/_{\lambda} \qquad \text{I.11}$$

Where h is Planck's constant (h ≈ 6.626 × 10^{-34} J·s). Furthermore, the relationship between the wavelength (λ) and frequency is expressed by:

$$\lambda = {}^{hc}/_{E} \qquad \text{I.12}$$

Spectral radiance in figure 02 ASTM G173 is a uniform reference solar spectrum that is widely used for various energy-related calculation, this Spectral irradiance represents the solar radiation reaching the surface of the earth under typical conditions after passing through the atmosphere. The spectrum is divided into several parts based on wave length.

III.1. UltraViolet radiation

UltraViolet (UV) radiation the most part of natural UV radiation is absorbed by Earth's atmosphere less than 6% of Ultar-Violet type A and type B (UVA) and (UVB) can reach the earth's surface, UV radiation can be classified into three arrays:

- Ultar-Violet type A (UVA) 315 - 400 nm Least energetic but penetrates deep into the skin, causing aging and long-term damage.
- Ultar-Violet type B (UVB) 280 - 315 nm Causes sunburn and is the primary culprit behind skin cancer.
- Ultar-Violet type C (UVC) 100 - 280 nm Most harmful but totally absorbed by Earth's atmosphere, and does not reach the surface.

III.2. Visible radiation

Visible solar radiation, is the portion of the electromagnetic spectrum that the human eye can perceive. It falls between wavelengths of approximately 380 nm (violet) and 750 nm (red), as shown in figure 02 the sun emits the most radiation in the visible range, peaking at around 450 nm to 500 nm.

III.3. Infrared radiation

InfraRed (IR) radiation described as photons with low energies about some meV to some eV, IR radiation can be subdivided into many arrays according to wavelength:

- Near-Infrared (NIR) – ~0.75–1.4 µm (just beyond visible red).
- Short-Wave IR (SWIR) – ~1.4–3 µm.
- Mid-Wave IR (MWIR) – ~3–8 µm.
- Long-Wave IR (LWIR) – ~8–15 µm.
- Far-IR (FIR) – ~15–1000 µm (overlaps with sub-millimeter/terahertz)

Based on these divisions many detectors technology can be defined, where the most traditional photovoltaique designed to absorb visible and only small part of near-infrared light to generate electricity, However, a significant portion of the Sun's energy in the infrared (IR) spectrum cannot be converted to energy by using this kind of panels. Developing solar cells that can efficiently convert infrared radiation into electricity has been a major focus in new generation photovoltaic research. The aim is to Combining visible and IR-absorbing materials by using specific materials and structures can operate in large range of solar spectrum from visible to Mid-InfraRed [07].

IV. Radiation-matter interaction "photoelectric effect"

The radiation-matter interaction is based on the "photoelectric effect", a physical phenomenon discovered in 1839 by the French scientist Edmond Becquerel, who noticed that certain substances produce an electric current when exposed to light. However, this phenomenon would not be properly understood until 1905 in the framework of the quantum theory of the photoelectric effect developed by Albert Einstein based on the ideas developed in 1900 by Max Planck in his theory of black body radiation [03].

IV.1. Photon detection versus thermal detection

Thermoelectric detectors are categorized into two types: photon detectors and thermal detectors. Photon detection becomes obvious when incoming photons of energy $E = hv$ are absorbed by the detecting material usually semiconductors, resulting in the excitation of free electron-hole pairs. Typically, the material is either a bulk semiconductor or a low-dimensional substance such as nanostructured materials. The electrical power originates from the alteration in electron dispersion

within the detector. Otherwise, thermal detection is characterized as the process by which a measurable attribute of the detecting substance alters owing to the temperature increase of that material caused by radiation absorption. The primary thermal processes are the thermoelectric effect.

V. Photo-electric absorption phenomena

Absorption can occur either through an intra-band or inter-band process. Inter-band absorption occurs during an electronic transition from an initial state (E_V, k_V) in the valence band to a state (E_C, k_C) in the conduction band (Figure I.3).

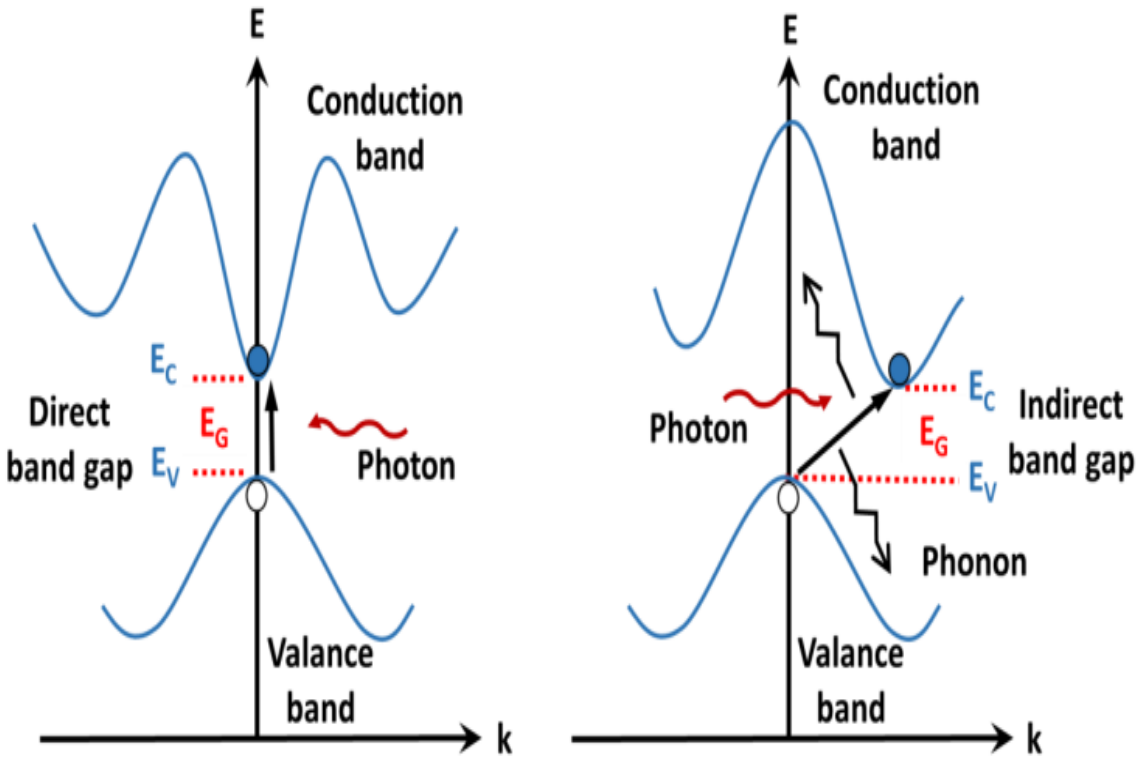

Figure I.3: Photon absorption in direct and indirect bandgap semiconductor [5].

This transition is supposed to be direct if the energy and wave vector conservation conditions decree that: $k_V = k_C$. While an indirect transition, can exist if the absorption is accompanied by the emission or absorption of a phonon, and in this case, the relationship becomes:

- The photoelectric effect refers to the capacity of matter to release free electrons, known as photoelectrons, upon exposure to light. Heinrich Hertz initially saw and described it in 1887. Classical Maxwell's wave theory posits that when light flux rises, the energy required for electron ejection or emission from the medium also increases.
- The photovoltaic effect is a specific instance of the photoelectric effect, was identified and articulated some years before Hertz's findings. In 1839, Alexandre Becquerel discovered the photovoltaic phenomenon while examining the influence of light on electrolytic cells. This phenomenon refers to the generation of a potential difference in a substance when subjected to light exposure.

V.1 The principle of thermophotovoltaics

Photovoltaics (PV) is the general term for the conversion of electromagnetic radiation into electrical energy by exploiting the photovoltaic effect. Photovoltaic cells typically use the sun as the radiation source. Thermophotovoltaics (TPV) refers to the specific case of power generation from radiation of a spectrum whose maximum lies at longer wavelengths ("thermal radiation") than that of the sun. A heat source heats an emitter, which radiates its energy toward the PV cells.

The type of heat source is arbitrary, as long as it is capable of continuously supplying energy to keep the emitter at the desired temperature. By using an emitter with specific radiation properties, spectral matching can be achieved both on the side of the emitter and on that of the PV cells. This represents a significant advantage over conventional solar photovoltaics. This bilateral spectral adaptation between emitter and filter enables, in principle, higher cell efficiencies than in solar photovoltaics. To maximize the electrical efficiency of a thermophotovoltaic system, optimal spectral matching between the emitter and the PV cells must be achieved. As mentioned, this adaptation is possible on both sides through the selection of suitable materials. Planck's radiation law describes the spectral power density equation I.8.

VI. Thermoelectricity

Thermoelectric conversion denotes the process of transforming heat energy to electrical energy mainly derived from thermal radiation. This process could be used in a variety of applications, from powering sensors and devices in remote areas to capturing waste heat from industrial processes or even car engines to generate electricity. The direct radiation heat flux is concentrated in the infrared spectrum (780 nm - 1000 µm) and transmits as infrared photons (photon of low energy). This is done using thermoelectric materials that exploit three separate thermoelectric phenomena, which will be detailed below [11].

VI.1. Seebeck effect

Seebeck coefficient has the major contribution into the thermoelectric material performance. The Seebeck effect was discovered in 1821 by the German physicist Thomas Johan Seebeck. It describes the phenomenon of the appearance of an electric potential difference along a material subjected to a temperature gradient is known as the Seebeck effect [12].

The Seebeck effect can be also characterized a couple formed by two materials of different nature and which are subjected to a temperature difference.

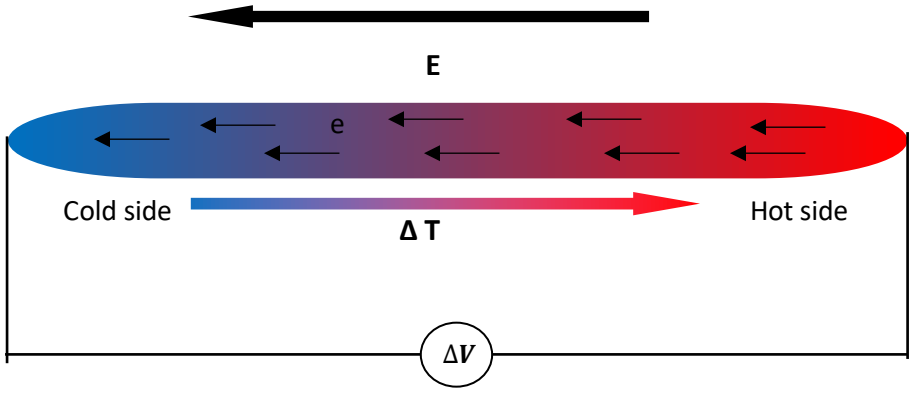

Figure I.4: Seebeck effect for thermoelectric material.

The Seebeck coefficient can be derived from the general form for the Mott relation is [13]:

$$S = \frac{k_B}{q} \cdot \frac{\int \sigma(E) \cdot (E - E_F) \cdot \frac{\partial f(E)}{\partial T} dE}{\int \sigma(E) \cdot \frac{\partial f(E)}{\partial E} dE} \qquad \text{I.13}$$

k_B: Boltzmann constant q: Charge of the carrier σ (E): Energy-dependent electrical conductivity, f(E): Fermi-Dirac distribution function. E: Energy, E_F fermi level energy

This form implies that the Seebeck coefficient is proportional to the Fermi level's location linked to the band edge, where the fermi level is defined as function of carrier concentration, So in Terms of Carrier Concentration for non-degenerate semiconductors, the Seebeck coefficient is related to carrier concentration by the relation:

$$S = \frac{k_B}{q}\left[\ln\left(\frac{2\pi m^* k_B T}{h^2}\right) + \ln\left(\frac{1}{n}\right)\right] \qquad \text{I.14}$$

It can be seen from the equation I.13, the Seebeck coefficient can be changed by tuning the effective mass and carrier concentration [14], from equations I.13 & I.14 to improve thermoelectric power of materials by maximizing Seebeck effect we need materials with higher effective mass and optimized doping levels which lead to a material of high electric conductivity.

VI.2. Seebeck coefficient with transport coefficients

A martials with high electric conductivity is typically a degenerate semiconductors or metals, the Seebeck coefficient depends on the transport coefficients, which consider the scattering mechanisms [13]:

$$S = -\frac{\pi^2 k_B^2 T}{3q}\left(\frac{\partial ln\sigma(E)}{\partial E}\Big|_{E=E_F}\right) \qquad \text{I.15}$$

Where: $\sigma(E)$: Energy-dependent electrical conductivity, E_F: Fermi energy.

As shown in equation I.15 the Seebeck coefficient is temperature-dependent. At Low Temperatures: The Seebeck coefficient is proportional to the temperature T due to the $\frac{\partial f}{\partial T}$ term in equation I.13. At High Temperatures: The exponential term dominates as shown in figure I.5 in semiconductors, leading to $S \propto ln\frac{1}{n}$ in equation I.15.

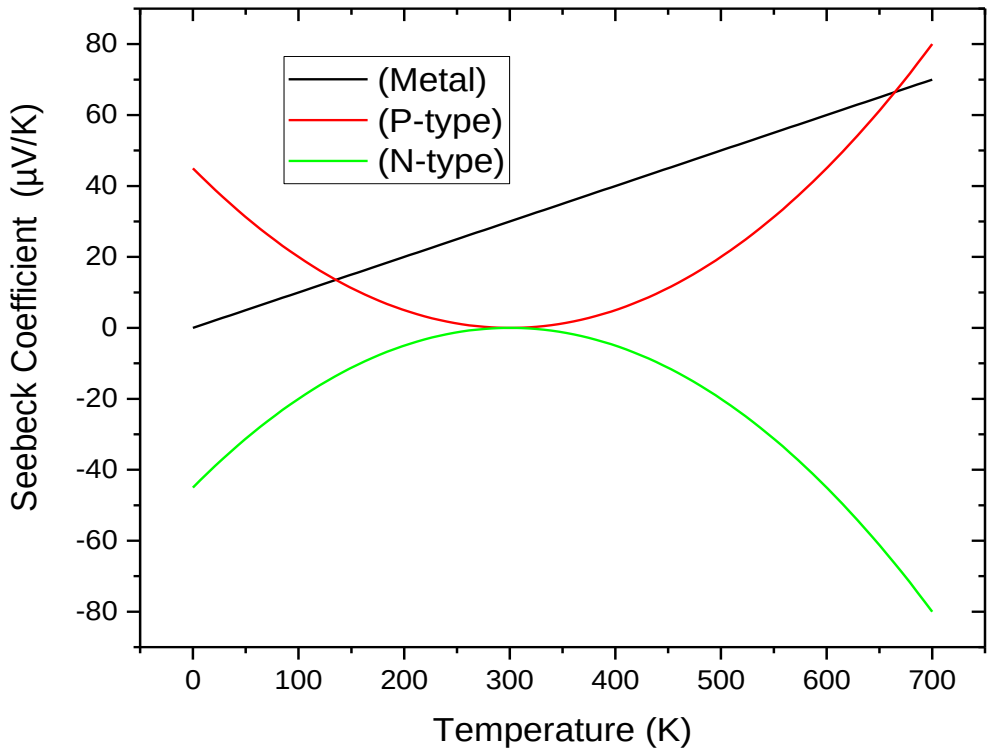

Figure I.5: Variation of Seebeck coefficient S (µV/K) as function of temperature T (K), for different kind of materials Semiconductor PN and metal.

Figure I.5 shows the variation of Seebeck coefficient in metal where a linear variation of S proportional with temperature variation. For semiconductor P-type a parabolic behavior due to the dependence of carrier concentration on temperature, with positive values of *S*. On the other hand, for N-type semiconductor a similar parabolic behavior but with negative values of S, indicating that electrons dominate as charge carriers. This behavior highlights the significance of material selection in optimizing thermoelectric devices. So, the sign of the Seebeck coefficient depends on the type of charge $S < 0$, indicates that the charge carriers are electrons, or $S > 0$ indicates that the charge carriers are holes.

we revealed the relationship between the type of semiconductor N or P, where the Seebeck coefficient should be negative for N type S/C and positive for P type S/C and the temperature

dependence of Seebeck coefficient. So in case of couple of two semiconductor materials, for PN junction the Seebeck coefficient of the couple is given by the relation:

$$S_{ab} = S_b - S_a \qquad \text{I.16}$$

S_{ab} is the thermoelectric power of the couple formed by two different materials a and b.

VI.3. Electrical conductivity

Materials used for this purpose, are specially designed to have high electrical conductivity. In the Boltzmann transport theory, the electrical conductivity σ, and Seebeck coefficient S, are expressed as [04]:

$$\sigma = e^2 \sum_k \left(-\frac{\partial f_0(\varepsilon_k)}{\partial \varepsilon_k}\right) v_k v_k \tau_k \qquad \text{I.17}$$

$$S = \frac{e}{\sigma T} \sum_k \left(-\frac{\partial f_0(\varepsilon_k)}{\partial \varepsilon_k}\right) (\varepsilon_k - \varepsilon_F) v_k v_k \tau_k \qquad \text{I.18}$$

Where $f_0(\varepsilon_k)$ is the Fermi–Dirac distribution function given by:

$$f_0(\varepsilon_k) = 1/[\exp((\varepsilon_k - \varepsilon_F)/k_B T) + 1] \qquad \text{I.19}$$

ε_k is the band energy at k-point;

ε_F is the Fermi energy;

$v_k = (1/\hbar)\nabla_k \varepsilon_k$ is the group velocity;

τ_k is the relaxation time due to scattering with phonons and/or disorders/impurities

The photoelectric effect cross-section per atom, τ, is approximately given by [03]:

$$\tau(h\nu, Z) = k \frac{Z^n}{h\nu^m} \qquad \text{I.20}$$

k is a constant, Z is the atomic number,

n is an exponent in the range 3.6-5.3, being largest for low atomic numbers,

m is an exponent in the range 2.5-3.5, again being largest for low atomic numbers

The applications of various forms of radiation in technological fields are touched upon as well

Solar energy conversion is the process of converting the energy of photons emitted by the sun in the form of electromagnetic waves into electrical energy. To achieve this operation, proper optoelectronic devices known as "solar cells" must be implemented. In this study, we are interested in solar thermo-photovoltaic cells, which are a popular topic due to the highly attractive potential for considerable improvements in the future of TPV performance. The basic concept behind these thermo-photovoltaic is combine two types of solar photodetectors [16]; photovoltaic and thermo-voltaic. To fully understand how these devices work, it is necessary to explain the physical principle of each of the two sensors.

VII. Peltier effect

The Peltier effect was discovered in 1834 by the French physicist Jean-Charles Peltier [15]. Unlike the Seebeck effect, the Peltier effect occurs between two materials of the same type but different nature (N-type and P-type) when an electric current is passed through a junction connecting these two materials. Depending on the type of doping and the direction of the current, we have either an absorption or a release of heat.

The dissipated or absorbed heat flux is given by [17]:

$$Q = \pi_{ab} I = (\pi_b - \pi_a) I \qquad \text{I.21}$$

π_{ab} Peltier coefficient [JA^{-1}].

π_{ab} can be positive or negative. If a current imposed in the direction A → B causes heat to be released at B and absorbed at A, then the Peltier coefficient of the junction π_{ab} is positive. Otherwise, π_{ab} is negative. When a temperature gradient is applied to both sides of an elementary thermoelectric couple as shown in figure 06, an electric power is created when the PN couple are connected to an external load to broad the circuit, The efficiency of the thermoelectric generator is defined by the ratio of the electrical power generated by the thermoelectric module to the thermal power Q given off by the heat source.

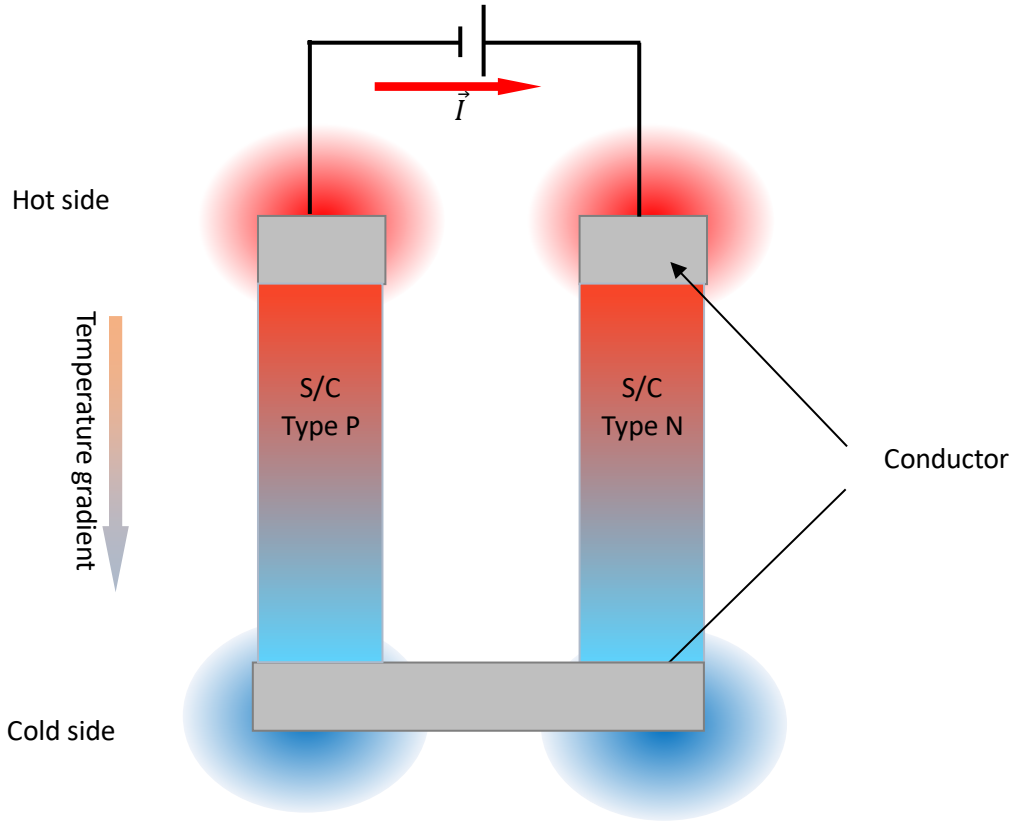

Figure I.6: Peltie effect for PN junction.

VIII. Thermal conductivity

In a crystalline solid, heat transfer can be realized by the movement of charge carriers (electrons) κ_e and lattice vibrations (phonons) κ_l, where the total thermal conductivity is therefore defined as the sum of these two factors

$$\kappa = \kappa_e + \kappa_l \qquad \text{I.22}$$

κ_e depends on the charge carrier concentration and is directly related to the electrical conductivity

$$\sigma = \frac{1}{\rho} = n.e.\mu \qquad \text{I.23}$$

n the charge carrier concentration, e the electron charge and μ the charge carrier mobility

$$\mu = \frac{e\tau}{m^*} \qquad \text{I.24}$$

we obtain

$$\kappa_e = L.n.\frac{e^2\tau}{m^*}T \qquad \text{I.25}$$

L is the Lorentz factor. For a free electron gas, L is a constant defined by the relation

IX. Thomson effect

The Thomson effect was discovered in 1851 by the English physicist William Thomson. It demonstrates that the two preceding effects, the Seebeck effect and the Peltier effect, are related to each other. where a material either can absorbs or releases heat depending on the direction of current flow which is related to the temperature gradient. This effect is important in thermoelectric applications, such as in thermoelectric generators or cooling devices, because it contributes to the overall thermoelectric efficiency and performance.

As discussed in section V and VI It is typically seen in materials where the electrical conductivity and thermal conductivity are highly coupled and can highly impact the overall design of thermoelectric devices.

So, the Thomson effect describes the relationship between the temperature gradient and the electric current applied simultaneously on a segment dx, where the heat flow gradient is given by.

$$\frac{dQ}{dX} = \tau I \frac{dT}{dX} \qquad \text{I.26}$$

τ is the Thomson factor depending on the type of material

Considering that the Seebeck coefficient, electrical resistivity and thermal conductivity are independent of temperature, for couple of two materials a and b τ_{ab} is given by the relation:

$$\tau_{ab} = \tau_a - \tau_b = T\frac{dS_{ab}}{dT} \qquad \text{I.27}$$

Due to the above-mentioned discoveries, it is achievable to produce an electric current by establishing a temperature gradient (Seebeck effect) or to either generate heat or cool by using a junction between two materials based on the current's direction (Peltier effect) [08].

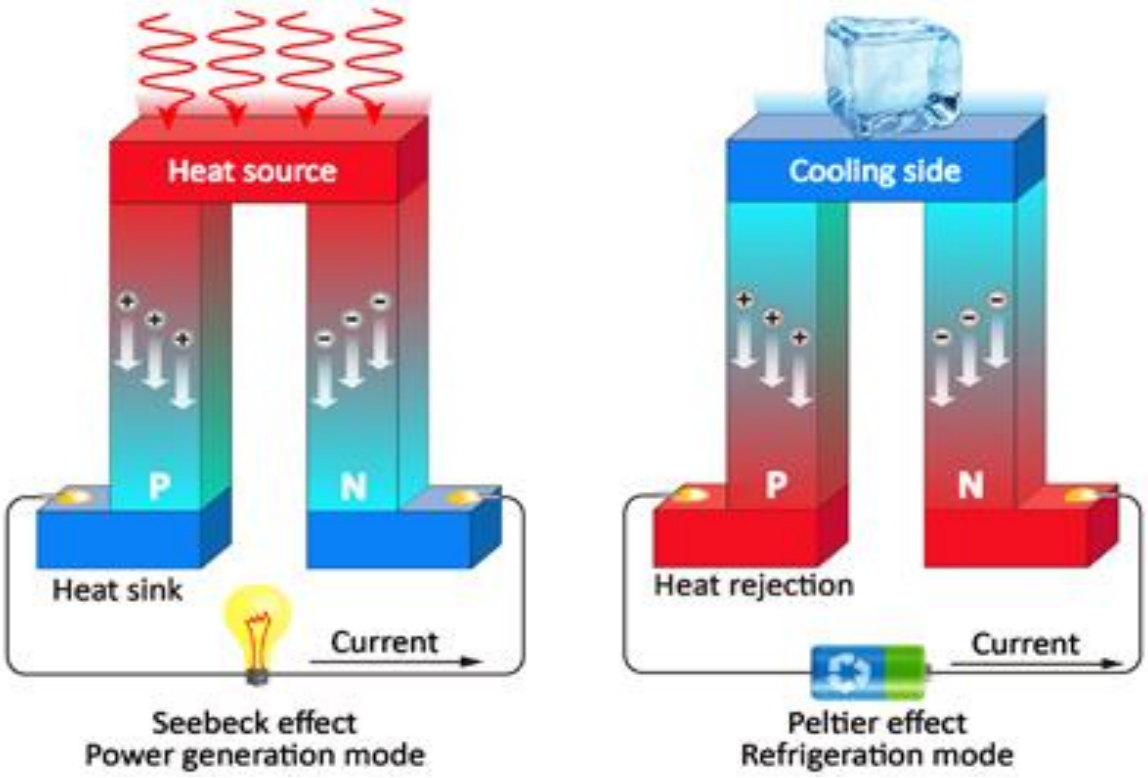

Figure I.7: Coupled seebeck and peltier effect in one module used for power generation and cooling generation.

X. Thermoelectric figure of merit

Consequently, it is essential to possess a pair of materials for the creation of a thermoelectric module. N-type and p-type semiconductor materials are often utilized as shown in figure I.7, to construct a thermoelectric module, it is essential to utilize N pairs of N-type and P-type semiconductor materials, which are electrically coupled in series and thermally in parallel.

The efficiency of a thermoelectric material depends primarily on the thermoelectric materials figure-of-merit, known as zT this allows us to evaluate the performance of a material or even a module. It depends on different parameters as shown in the equation I.28

The thermoelectric performance depends on the efficiency of the thermoelectric material for transforming heat into electricity.

$$ZT = TS^2 \frac{\sigma}{\mathcal{K}} = T \frac{PF}{\mathcal{K}} \qquad \text{I.28}$$

To optimize a material's performance, a high Seebeck coefficient and electrical conductivity, as well as low thermal conductivity, are required.

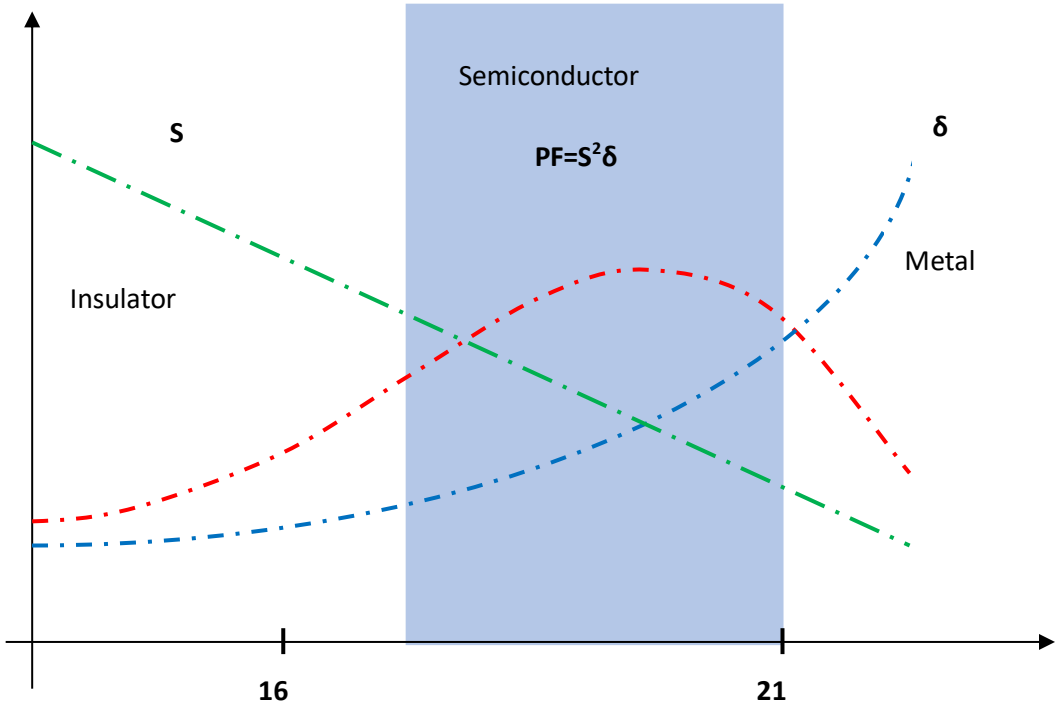

Figure I.8 : Carrier concentration Log_{10} (n, p).

A material that encounters all the of thermoelectric characteristics at bulk state cannot reach high value of zT due to the correlation between the different parameters of materials. As shown in figure I.8 insulators have a high Seebeck coefficient and low thermal conductivity, but their electrical conductivity is low, which extremely reduces their figure of merit (ZT). For metals, high electrical

conductivity is observed at the expense of the other two parameters. This therefore results in a low figure of merit. doping also makes it possible to select the desired type of conduction and to enhance the Seebeck coefficient, ultimately leading to an increase in the figure of merit.
The electrical and thermal contact resistance is considered ideal and that the steady state is reached, the efficiency of a module composed of an n-type semiconductor and a p-type semiconductor is written:

$$S = \frac{\pi^2 k_B^2 T}{3e} \times \frac{d \ln \sigma(E)}{dE}\Big|_E = E_F \qquad \text{I.29}$$

So, the Seebeck coefficient is proportional to the first derivative of the density of state (DOS) in the vicinity of the Fermi level [18].

$$S \propto \frac{1}{DOS(E)} \times \frac{dDOS(E)}{dE}\Big|_E = E_F \qquad \text{I.30}$$

A high Seebeck coefficient, at a given charge carrier concentration, is obtained when the derivative of the density of states, i.e. the slope near the Fermi level, is large. A high density of states can be the consequence of many bands present at the Fermi level or flat bands with a large effective mass m^* [14]. The electrical conductivity σ is determined by the mobility of the charge carriers, μ, which is itself influenced by their effective mass.

A detailed theoretical analysis of the variation of the factor ZT with temperature and carrier concentration is particularly complex because it requires precise knowledge of the energy spectra of phonons and charge carriers, as well as their scattering mechanisms, some of this feature can be obtained from solving the Boltzmann transport equation by assuming a parabolic band model, by taking into consideration the relaxation time approximation. The calculations confirm that the most interesting properties are obtained for semiconductors having their Fermi level, E_F, located a few $k_B T$ from a band edge (conduction or valence). They also suggest that a high ZT can be obtained via the optimization of the parameter β, defined by the relation:

$$Z \propto \beta \propto \left(\frac{m^*}{m_0}\right)^{\frac{3}{2}} \frac{\mu}{k_l} \qquad \text{I.31}$$

where m^* is the reduced effective mass of electrons or holes, m_0 is the mass of the electron in vacuum, μ is the intrinsic mobility of charge carriers, and κ_e is the lattice thermal conductivity. Thus, large values of the parameter β can potentially lead to high figures of merit. Equation (I.31)

shows that it is also important from a thermoelectric point of view to optimize the mobility of charge carriers and their effective mass. This relationship indicates that semiconductors with a hefty effective mass, high mobility, and low lattice thermal conductivity represent the best candidates [19]. However, these requirements tend to be mutually incompatible (high mobility is usually linked to a low effective mass, for example, as emphasized in Equation (I.31), and it then becomes difficult to derive additional information from this model for the optimization of conventional thermoelectric material. At this scale here is a compilation of attributes that serves as a framework for the exploration of good thermoelectric materials:

- Achieve a charge carrier concentration ranging from 10^{18} to 10^{21} cm^{-3}
- Maintain a narrow band gap at ambient temperature T
- Enhance $\mu\ \kappa_e$ by creating solid solutions, in which increased disorder significantly scatters phonons due to mass or charge fluctuations in the lattice.
- Decrease lattice thermal conductivity κ_l by employing multi-element compounds characterized by high atomic mass, large unit cell dimensions, and low Debye temperature;
- Foster a high effective mass of charge carriers and a pronounced variation in the density of states at the Fermi level to optimize thermoelectric power.
- Maximize $(m^*/m_0)\ \mu$ using compounds with multi-valley band structures while preserving charge carrier mobility. Raised up mobility can be reached in compounds of atoms with little electronegativity disparity. Significant disparities indicate a pronounced ionic nature of atomic bonds and often result in substantial scattering of carriers by optical phonons.

X.1. Efficiency of thermoelectric module

The energy conversion efficiency η of thermocouple in electricity generation mode. is given by the ratio of the useful electrical power P delivered in a load device to the thermal power ϕ_c extracted from the heat source [19], so to maximize these two ratios depend only on the difference of temperature between the two side T_H (T hot) and T_C (T cold), the efficiency of a coupe PN characterized with figure of merit ZT_{pn} expressed in K^{-1} by the relation:

$$\eta_{max} = \frac{T_C - T_f}{T_C} \times \frac{\sqrt{1+Z_{pn}T_m}-1}{\sqrt{1+Z_{pn}T_m}+\frac{T_f}{T_c}} \qquad \text{I.32}$$

Where $T_m = (T_H + T_C/2)$

XI. Conclusion

In this first chapter we describe the theoretical basics essential for understanding the challenges within this study domain. Although these can be summarized as optimizing the ZT figure of merit, all the theoretical considerations we have developed clearly demonstrate the difficulties encountered in this area. The diverse criteria illustrate that the macroscopic and/or microscopic factors involved in the optimization of thermoelectric materials are incompatible, thus, the challenge resides in the interdependence of the properties defining this figure of merit: raised carrier concentration leads to reduced electrical resistivity but tends to reduce thermoelectric power and augment electronic thermal conductivity, thereby increasing total thermal conductivity. This discovery provides a significant issue that must be addressed to get the optimal balance among these three variables for the enhancement of the ZT factor. For this purpose, several selection criteria have been established empirically by examining the performance of several classes and families of materials we will explore all that in the next section.

Chapter II

Nanostructuration effect interband & intersubband quantum photodetector

I. Introduction

Conventional materials continue to be utilized in contemporary equipment, including refrigeration and energy generation. Although discovered several decades ago (1950-1960), the materials addressed in this section remain the focus of ongoing research, intended to enhancing their thermoelectric characteristics by nanostructuring thermoelectric materials. The materials mostly consist of III-V based alloys such as bismuth-antimony alloys. They may be categorized based on their ideal temperature working range. Figure II.1 illustrates the temperature progression of the ZT factor for the most effective conventional n- and p-type materials [20]. All these materials are semiconductors with a narrow band gap ($0 < E_g < 1\ eV$), and the majority satisfy the conditions outlined in the preceding chapter. In the last two decades, several approaches have been commonly used (nanostructuring [21,22], multi-scale systems [23], modification of the band structure with resonant effects [22], the search for systems with multi-valley structures [24], the concept of "Phonon-glass electron-single-crystal (PGEC). Here, we will only address some of these approaches. On the first hand, nanostructuring to reduce the lattice thermal conductivity and, on the other, the use of composite materials. These approaches are relevant because they allow certain families of materials such as bismuth-antimony alloys, which have a relatively a good thermal propriety, to strive with conventional thermoelectric materials without suffering their drawbacks (costly, scarce, and/or toxic). But these are not the only approaches; doped alloys are also widely studied because they allow the charge carrier concentration to be modified. Overall, these three approaches can be grouped under a single "label," the concept of a multi-scale material [20].

II. Conventional thermoelectric materials

Materials with interesting thermoelectric performance are mainly semiconductors and semimetals. There are different families of thermoelectric materials such as skutterudites, silicides, oxides, Half Heuslers, double half heuslers and many others.

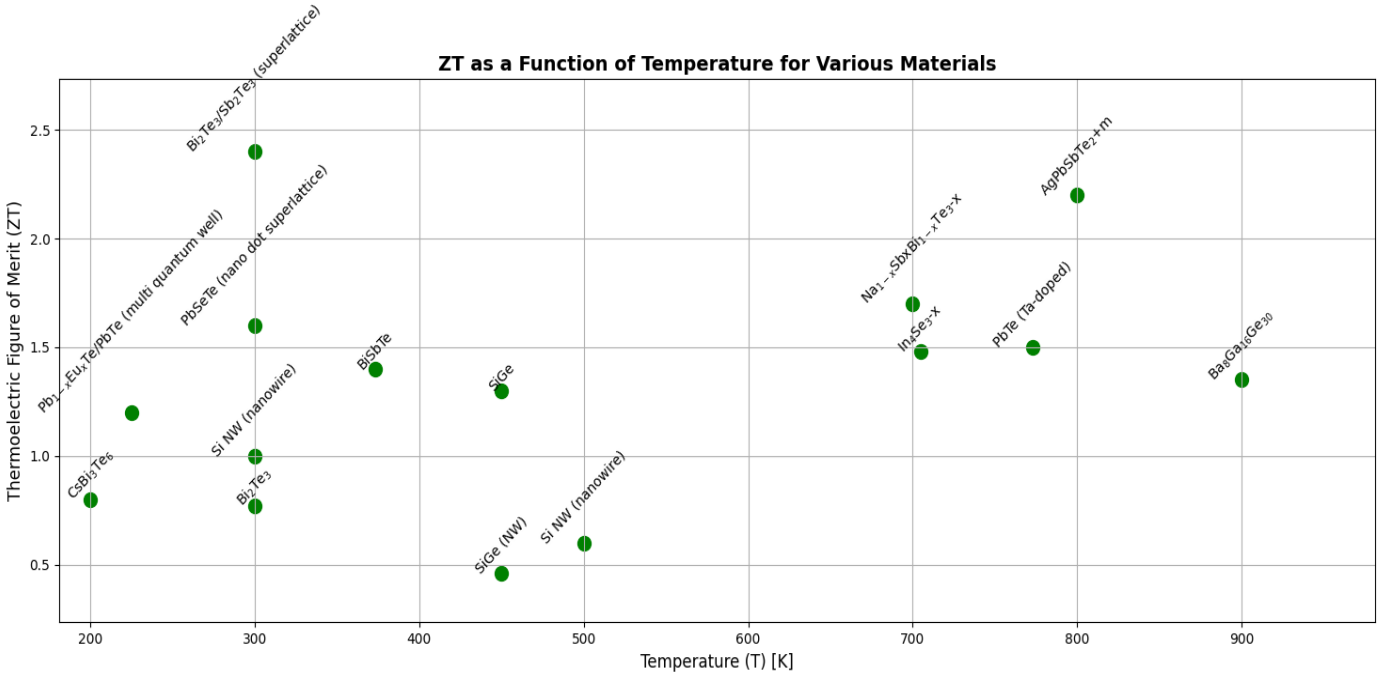

Figure II.1 Figure of merit as a function of temperature of various conventional thermoelectric materials and nanostructured materials.

Figure II.1 presents some thermoelectric materials. this figure shows that the performance of thermoelectric materials is optimal over a restricted temperature range. Thus, a thermoelectric material is chosen based on its intended application, the temperature range in which the thermoelectric module will be used.

It has been shown by various authors that the addition of a small amount of one or more chemical elements leads to an increase in the power factor, Aloys based on bismuth and antimony have been recognized as excellent thermoelectric materials for power production in temperature ranges suitable for global applications, Recent research has demonstrated that exceptionally high figure of merit values may be attained by leveraging the convergence of valence bands where a high value of zT can reach 2.4 as shown in table II.1. For this reason, we will pay particular attention to its electronic band structure, a brief presentation of its topological and superconducting

properties will be the focus of the following section before concluding with a presentation of the transport properties of material based on Sb/Bi materials and the strategies used so far to improve its thermoelectric performance.

Table II.1: Figure of merit ZT for different materials.

Material	ZT	T (K)	Year	Reference
Bi_2Te_3/Sb_2Te_3 (superlattice)	2.4	300	2012	28
PbSeTe (nano dot superlattice)	1.6	300	2016	29
$AgPbSbTe_{2+m}$	2.2	800	2004	30
Bi_2Te_3	0.77	300	1958	31
$Pb_{1-x}Eu_xTe/PbTe$ (multi quantum well)	1.2	225	1996	32
$CsBi_3Te_6$	0.8	200	2000	33
Si NW (nanowire)	1.0	300	2008	34
Si NW (nanowire)	0.6	500	2008	35
BiSbTe	1.4	373	2008	36
$Na_{1-x}Sb_xBi_{1-x}Te_{3-x}$	1.7	700	2006	37
In_4Se_{3-x}	1.48	705	2009	38
PbTe (Ta-doped)	1.5	773	2008	39
$Ba_8Ga_{16}Ge_{30}$	1.35	900	2006	40
SiGe	1.3	1173	2008	41
SiGe (NW)	0.46	450	2012	42
SnSe	2.1	300	2014	43
$Hf_{0.75}Zr_{0.25}NiSn_{0.975}Sb_{0.025}$	0.82	1000	2017	44
$(Bi_{0.2}Sb_{0.8})_2Te_3$	2.3	300	2020	45

III. Nanostructured materials for thermoelectric

When the material is nanostructured, doped, or even composite, real optimization potential appears because the thermal conductivity is reduced [46]. Therefore, we chose to study a material with nanostructured properties. Indeed, reducing the dimensionality within the system mainly modifies the thermal conductivity, and more specifically the lattice thermal conductivity, which represents the largest contribution, without altering the electronic properties. Figure II.1 shows that nanostructuring thermoelectric materials can lead to an important increase in the figure of merit. It should be noted that this is not always the case. Indeed, reducing grain size reduces thermal conductivity but the number of interfaces increases, it also becomes more difficult for electrons to move between them. Thus, it is possible that the effect is counterbalanced by an increase in electrical resistivity. Another alternative will be explored in this work is the use of composite materials, which can influence thermoelectric properties.

Nanostructured thermoelectric materials have been developed in various forms, including nanowires, quantum dots, thin films, and superlattices. These materials have shown significant improvements in thermoelectric efficiency due to the reduced thermal conductivity and improved electronic properties, but for some domain of applications it's not advantageous as shown in the table II.1 for the SiGe and SiGe (NW).

III.1. Nanowires

Nanowires are one-dimensional nanostructures that exhibit quantum confinement effects, where electron motion is restricted to one dimension. These nanowires exhibit enhanced Seebeck coefficients and reduced thermal conductivity, which improves the ZT value. By adjusting the wire diameter, researchers can control the carrier concentration and carrier mobility, optimizing electrical conductivity. For example, in materials like Bi_2Te_3, PbTe, and SiGe, nanowires have been shown to have significantly lower thermal conductivity than their bulk counterparts.

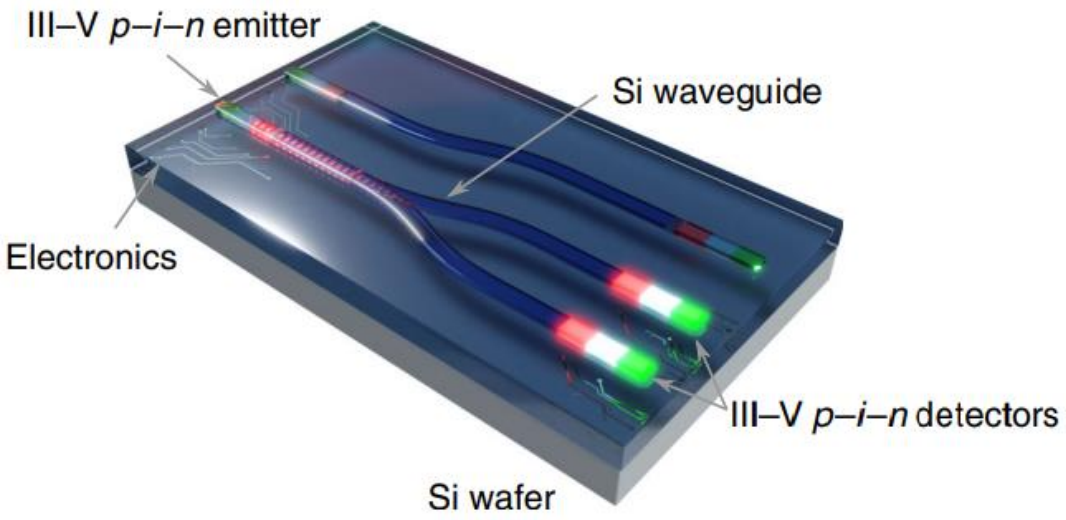

Figure II.2 A coupled nanowire photodetector and photoemitter based on III-V materials Using template-assisted selective epitaxy TASE figure from [47].

III.2. Quantum Dots

Quantum dots (QDs) are nanoscale semiconductor materials that exhibit discrete energy levels due to quantum confinement figure II.3. These discrete energy levels can enhance the density of states near the Fermi level, improving the Seebeck coefficient. In materials like PbTe and Bi2Se3, quantum dots embedded in a matrix have shown improvements in ZT values by lowering thermal conductivity while enhancing the electrical conductivity and Seebeck coefficient [48].

III.2.1. Size dependence of density of state in quantum dots:

As the size of the quantum dot decreases, the spacing between energy levels increases, which lead to a more pronounced quantization of the DOS. For very small dots, the DOS becomes highly discrete with only a few energy levels available.

As the dot size decreases, the energy spacing increases, and the DOS becomes more discrete. Thus, the dot size increases, the energy levels become closer, and the DOS transitions to the bulk material form, resembling a continuous density of states.

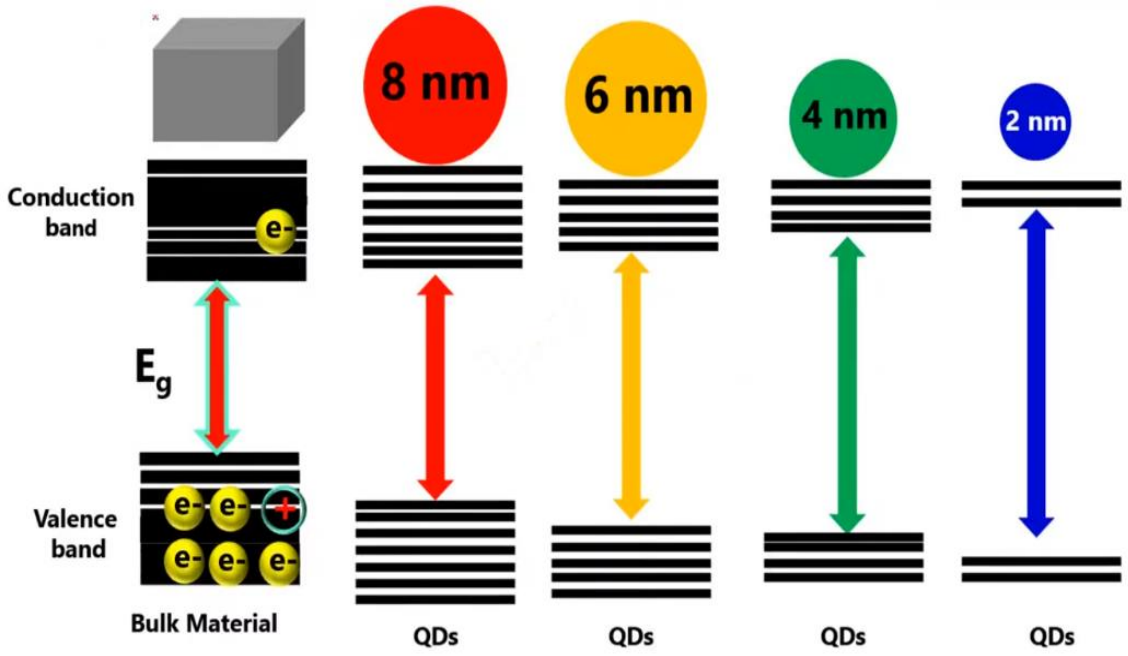

Figure II.3 Shows how size of quantum dots affects electronics and optoelectronics proprieties [49].

However, when the material is nanostructured, doped, or converted into a composite, a real optimization potential emerges, since its thermal conductivity can be reduced. For this reason, we selected a material that inherently exhibits nanostructuring due to its synthesis method. Indeed, reducing the dimensionality of the system primarily affects thermal conductivity specifically, the lattice contribution, while preserving the electronic properties. Another strategy for maximizing the figure of merit is to optimize the charge carrier concentration.

III.3. Superlattices

Superlattices nanostructure consist of alternating 2D layers of materials with different thermoelectric properties. These layers are often engineered at the nanoscale. By optimizing the geometry and the thickness of each layer, phonon scattering will be enhanced, thermal conductivity will be reduced while electrical conductivity can be improved or maintained. Using Materials like

Bi_2Te_3/Sb_2Te_3 or any other thermoelectric materials such as III-Sb based materials even other kind of optoelectronic materials like skutterudites or half-Heusler as superlattices have shown a significant improvement in ZT. This improvement is outcome of controlling the electron-phonon interactions at the interfaces. 2D thin films and other low-dimensional structures of complex superlattice have attracted much attention in research. Among the several thin film techniques are beat approaches and molecular beam epitaxy. High-quality superlattice have been produced by laser deposition, sputtering, metal-organic chemical vapor deposition, and chemical solution deposition depend type of alloys material and the chemical proprieties of materials a varied range of synthesis techniques beyond those. In the next chapter we will discuss particular synthesis and characterization and engineering investigations on thermoelectric superlattice.

IV. Density of states influence on optoelectric and thermoelectric nanostructured materials

By increase in the density of states at the Fermi level in nanostructured materials leads to an increase in the effective charge mass without changing their concentration [50]. This results in an increase in the Seebeck coefficient. Also, the possibility of exploiting phonon scattering at grain boundaries leads to a reduction in thermal conductivity [51]. The idea is to synthesize and use nanostructured materials, whose dimensions are well below 100 nm. The reduction in thermal conductivity in nanostructured materials was discussed by Hicks and Dresselhaus in 1993 for the superlattice structures of quantum wells (2D) and nanowires or nanotubes (1D) [52]. In this work, we proposed an important improvement in the figure of merit by an order of scale in nanostructured materials, thermoelectric properties can be improved compared to those of conventional bulk (3D) materials, due to the reduction in dimensions by significant changes in the density of electronic states [52] Figure II.4.

IV.1. Density of states for different dimensions

The density of state function describes the number of states that are possible in a system and is essential for determining the carrier concentration and energy distributions of carriers within a semiconductor

In semiconductors, the free motion of carriers is limited to two, one, and zero spatial dimensions. When applying semiconductor statistics to systems of these dimensions, the density of states in quantum wells (2D), quantum wires (1D), and quantum dots (0D) must be known.

Table II.2 Electronic density of states of semiconductors with 3, 2, 1, and 0 degrees of freedom for electron propagation.

Degrees of Freedom	Dispersion (Kinetic Energy)	Density of States	Effective Density of States
3D (bulk)	$E = \frac{\hbar^2}{2m^*}\left(k_x^2 + k_y^2 + k_z^2\right)$	$\rho_{dos}^{3D} = \frac{1}{2\pi^2}\left(\frac{2m^*}{\hbar^2}\right)^{3/2}\sqrt{E - E_C}$	$N_C^{3D} = \frac{1}{\sqrt{2}}\left(\frac{m^*KT}{\pi\hbar^2}\right)^{3/2}$
2D (well)	$E = \frac{\hbar^2}{2m^*}\left(k_x^2 + k_y^2\right)$	$\rho_{dos}^{2D} = \frac{m^*}{\pi\hbar^2}\sigma(E - E_C)$	$N_C^{2D} = \frac{m^*}{\pi\hbar^2}KT$
1D (wire)	$E = \frac{\hbar^2}{2m^*}\left(k_x^2\right)$	$\rho_{dos}^{1D} = \frac{m^*}{\pi\hbar}\sqrt{\frac{m^*}{E - E_C}}$	$N_C^{1D} = \sqrt{\frac{m^*}{2\pi\hbar^2}KT}$
0D (Dot)	$\langle E_K \rangle$	$\rho_{dos}^{1D} = 2\delta(E - E_C)$	$N_C^{0D} = 2$

As mentioned in chapter 1: equation I.30 to express the ZT enhancement mathematically across different dimensions, we can analyze how the density of states (DOS) and transport coefficients the mobility affects the figure of merit:

$$S \propto \frac{1}{DOS(E)} \times \left.\frac{dDOS(E)}{dE}\right|_{E = E_F} \qquad \text{II.1}$$

This means that in 1D and 0D systems, the high-pitched features in the DOS can enhance significantly through numerous mechanisms:

$$\sigma = q^2 \int \mu\,(E)\,\rho\,(E)\,\left(\frac{\partial f}{\partial E}\right)\,dE \qquad \text{II.2}$$

The derivative of the conductivity with energy depends heavily on the shape of the DOS near the Fermi level:

$$ZT \propto \frac{\left(\frac{d\ln\sigma(E)}{dx}\right)^2}{k/(\sigma\,T)} \qquad \text{II.3}$$

3D (Bulk Materials)

- Limited ZT due to the direct dependency with material proprieties S, σ, and κ. Typical ZT ~ 1

2D (Quantum Wells)

- Quantum confinement modifies the density of states near the Fermi level.
- Possibility to enhance the Seebeck coefficient S without severely reducing σ.
- Phonon scattering at interfaces can reduce lattice thermal conductivity κ_l.

1D (Quantum Wires)

- Improved density of states due to 1D subbands further increases S.
- Higher electron filtering and energy-dependent transport.
- Further phonon boundary scattering lead to lower thermal conductivity.

0D (Quantum Dots)

- Discrete energy levels (delta-function-like DOS).
- Strong potential for very high S.
- Carrier energy filtering is most effective.
- Extremely strong phonon scattering lead to very low κ.
- ZT enhancement possible, but practical challenges (low electrical conductivity, carrier tunneling big issues).

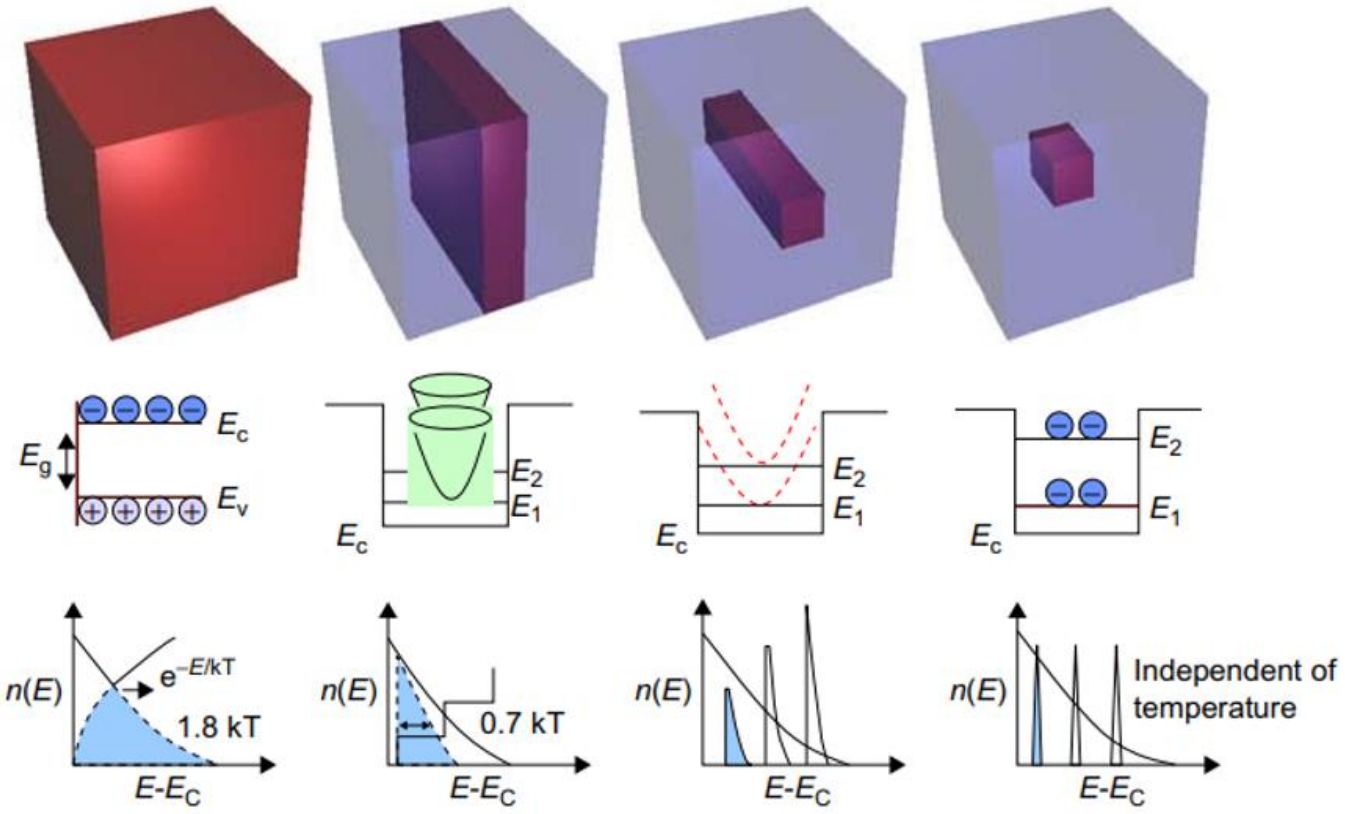

Figure II.4 Density of States (DOS) as a function of energy for different material dimensions: 3D-bulk materials, 2D-quantum wells, 1D-nanowires or nanotubes, 0D-quantum dots, and temperature dependency.

An increase in the density of states at the Fermi level, due to quantum confinement effects, leads to an increase in the Seebeck coefficient (equation chapiter 1 I.29), without reducing the electrical conductivity [52]. Furthermore, the lattice thermal conductivity can be significantly reduced by phonon scattering at interfaces and grain boundaries to decrease the phonon mean free path [52]. Based on this study a multitude of investigations on nanostructured materials have been conducted, which lead to an exciting finding. They achieved significant improvement in enhancing the figure of merit ZT, with values beyond the value of ZT=1 [53][54].

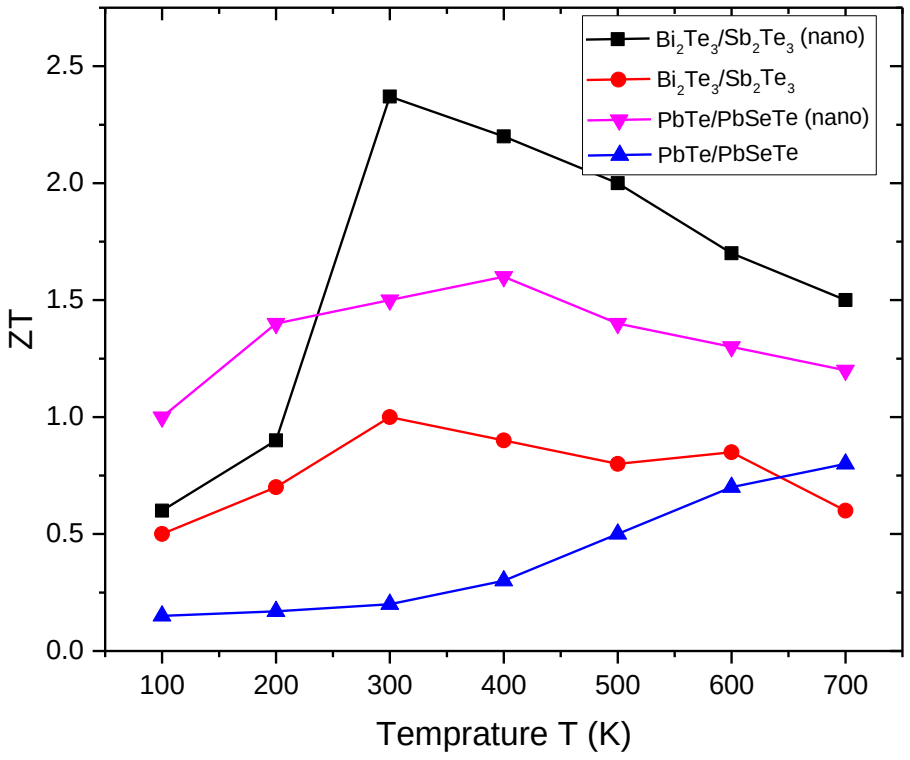

Figure II.5 Distinction between conventional thermoelectric materials and nanostructured materials as function of temperature.

Figure II.5 summarizes the findings derived from p-type superlattices of Bi_2Te_3/Bi_2Te_2, [53], and quantum well superlattices of PbTe/PbSeTe [54]. Nevertheless, these findings have yet to be simulated. Recently, the merit figure of the nano-composite $Bi_xSb_{2-x}Te_3$ has been reported to have increased by 40% compared to typical bulk materials, resulting in a merit figure ZT = 1.45 at near ambient temperature [55].

V. Phonon scattering and reduced thermal conductivity

In materials, phonons are quanta of lattice vibrations, and they are the primary carriers of heat in non-metallic materials (such as semiconductors, insulators, and ceramics). The heat conduction in these materials relies on the movement and scattering of phonons. In nanostructured materials, the

thermal conductivity (κ_l) is often significantly reduced compared to bulk materials. This reduction occurs because the phonons experience enhanced scattering at the interfaces, grain boundaries, and surfaces of the nanostructures [56]. the lattice thermal conductivity K_l depends on the phonon mean free path λ, and its expression is:

$$\kappa_l = \frac{1}{3} C_v v_v \lambda \qquad \text{II.4}$$

C_v is the specific heat capacity per unit volume, v_v is the speed of phonon vibration =speed of sound.

V.1. Phonon mean free path

The phonon mean free path (λ) is a measure of the average distance of phonon travels before it is scattered by imperfections, interfaces, or boundaries in the material. The phonon mean free path (λ) in nanostructured materials is typically much smaller than in bulk materials due to the presence of nanostructures (such as nanoparticles, thin films, or nanowires). The reduction of thermal conductivity in nanostructured materials is due to this decreased phonon mean free path [57].

For photoelectric efficiency, the carrier lifetime τ_{carrier} plays a key role. A longer carrier lifetime indicates fewer recombination, leading to improved photoconversion efficiency. The carrier lifetime is given by:

$$\tau_{carrier} = \frac{1}{recombination} \qquad \text{II.5}$$

For photoelectric materials, the diffusion coefficient D is related to the phonon scattering through the Einstein relation:

$$D = \mu K_B T \qquad \text{II.6}$$

The mobility μ is related to scattering, and scattering is influenced by the phonon mean free path λ, the diffusion coefficient D and consequently the efficiency of photoelectric conversion improve with longer phonon mean free paths.

VI. Photon detection in nanostructures superlattice

Photon detection can be further divided into photoconductive (PC) and photovoltaic (PV) detectors according to satisfaction or violation of symmetry in the configuration. photovoltaic detectors can

operate at zero bias, while photoconductive detectors require an external bias to initiate the operation. In addition to the simplest semiconductor slab, a comparably more complex PC photodetector structure is a QWIP [58], the basic elements of a QWIP are quantum wells (QWs) separated by wide barriers. The incident light is absorbed via Intersubband transitions of electrons within the QWs. Once the electrons are excited into the continuous upper states, they will be measured as a signal current. However, to collect these electrons, an external bias needs to be applied and the signal current responds in an almost linear fashion to the applied bias. Among various types of QWIPs, technology based on GaSb/AlGaAsSb/InGaAsSb multiple QWs is most mature [58].

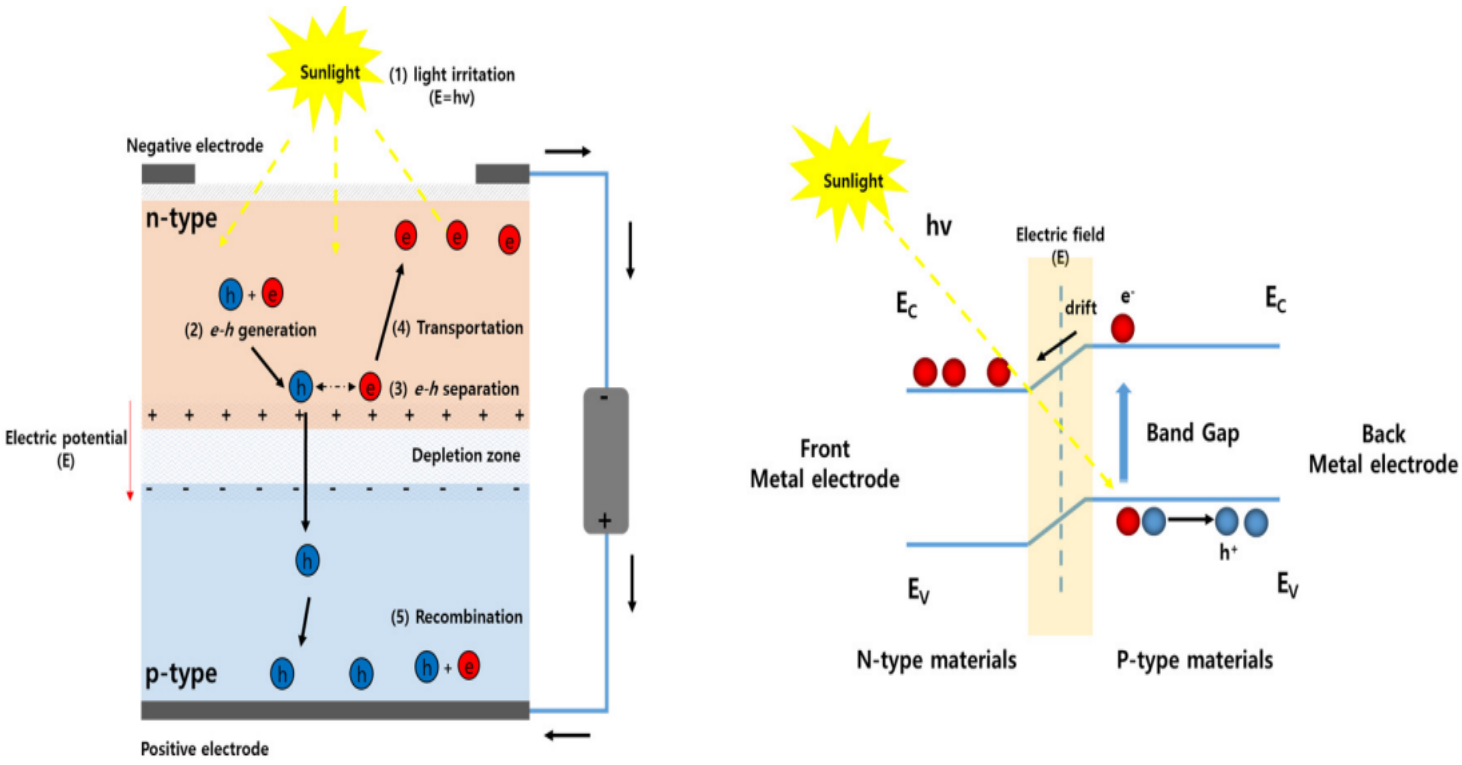

Figure II.6 Working principle of solar cell with p-n junction structure and (b) loss mechanism in standard p-n junction [59].

Major photovoltaic detectors are an extraordinary p-n junction, as seen in FigureII.6. The optically stimulated electrons and holes are segregated by the intrinsic electric field in the depletion area, thus contributing to the signal current. One method to enhance light absorption in a p-n junction is

to interpose a substantial intrinsic layer between the p- and n-doped layers, so creating the p-i-n structure. Certain p-i-n detectors can employ avalanche multiplication, provided they are reverse-biased [60].

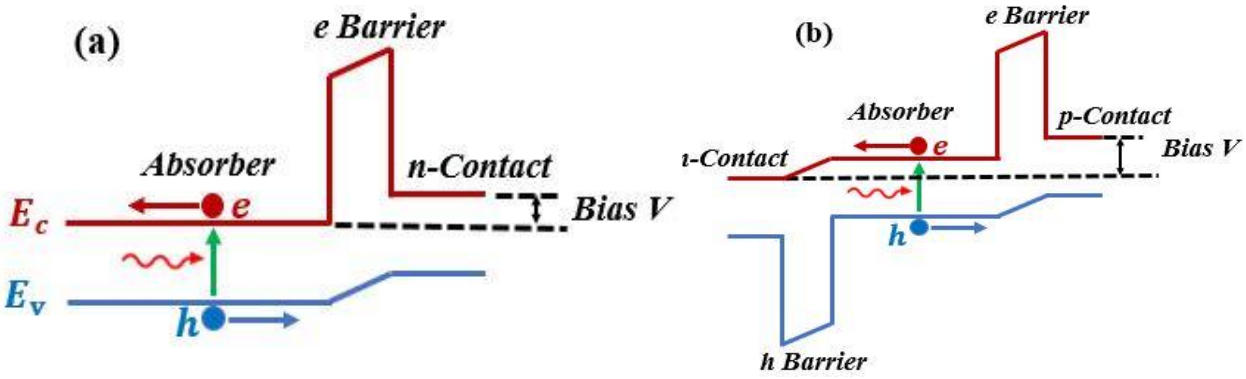

Figure II.7 Strategies to enhance thermoelectric performance by engineering the band structure of alloyed multitude materials to reduce the energy disparity between light and heavy carrier bands, hence improving Seebeck coefficients and power factors.can be executed on either the valence band and/or conduction band, respectively, for p-type and n-type carriers.

We decided to incorporate nano-engineering structure in order to obtain a multi-scale material. III-V antimonide based materials were chosen for this purpose, as they have already demonstrated promising results when combined with other thermoelectric materials as shown in table II.1

VII. Quantum nanostructured cascade photodetector

The quantum nanostructured cascade photodetector devices may exhibit significantly extended durations because it functions through intersubband transitions occurring inside a single band, such as the conduction band for electrons transition or valence band for holes transition. Elevated photon energy will increase thermalization loss. To assess the correlation between device performance and incident photon energy, an energy-dependent absorption coefficient is employed, which aligns well with that of quaternary, with a narrow bandgap.

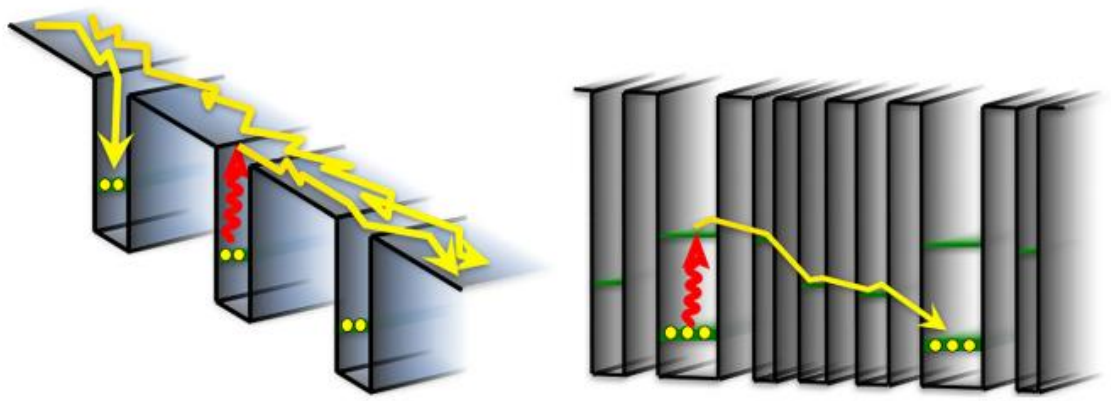

Figure II.8 Illustration of the photon absorption and cascading effect in an interband cascade photodetector figure from [63].

The origins and quantification of photoconduction and noise gains in quantum well infrared photodetectors (QWIPs) have been subjects of intense discussion for the last two decades. The photoconduction gain, which is inattentive in Quantum Cascade Detectors QCDs is the reason why QWIPs and QCDs have different Internal Quantum efficiency IQEs and consequently the efficiency EQEs are very similar [63], despite their comparable absorption efficiencies. It depends on the vague capture probability, which represents a high probability of an electron traversing the continuum of states above the barriers and incident upon a certain period being caught by the quantum well of that period, as opposed to passing over it (figure II.9). This differs from conventional devices that rely on interband transitions between the conduction and valence bands. This intrinsic disparity in carrier transport leads to varying carrier lifetimes and device performances, particularly at high temperatures.

lifespan τ of quantum cascade devices is in the picosecond range due to rapid phonon scattering, but interband cascade devices have a nanosecond lifetime scale owing to Auger and Shockley-Read-Hall (SRH) recombination.

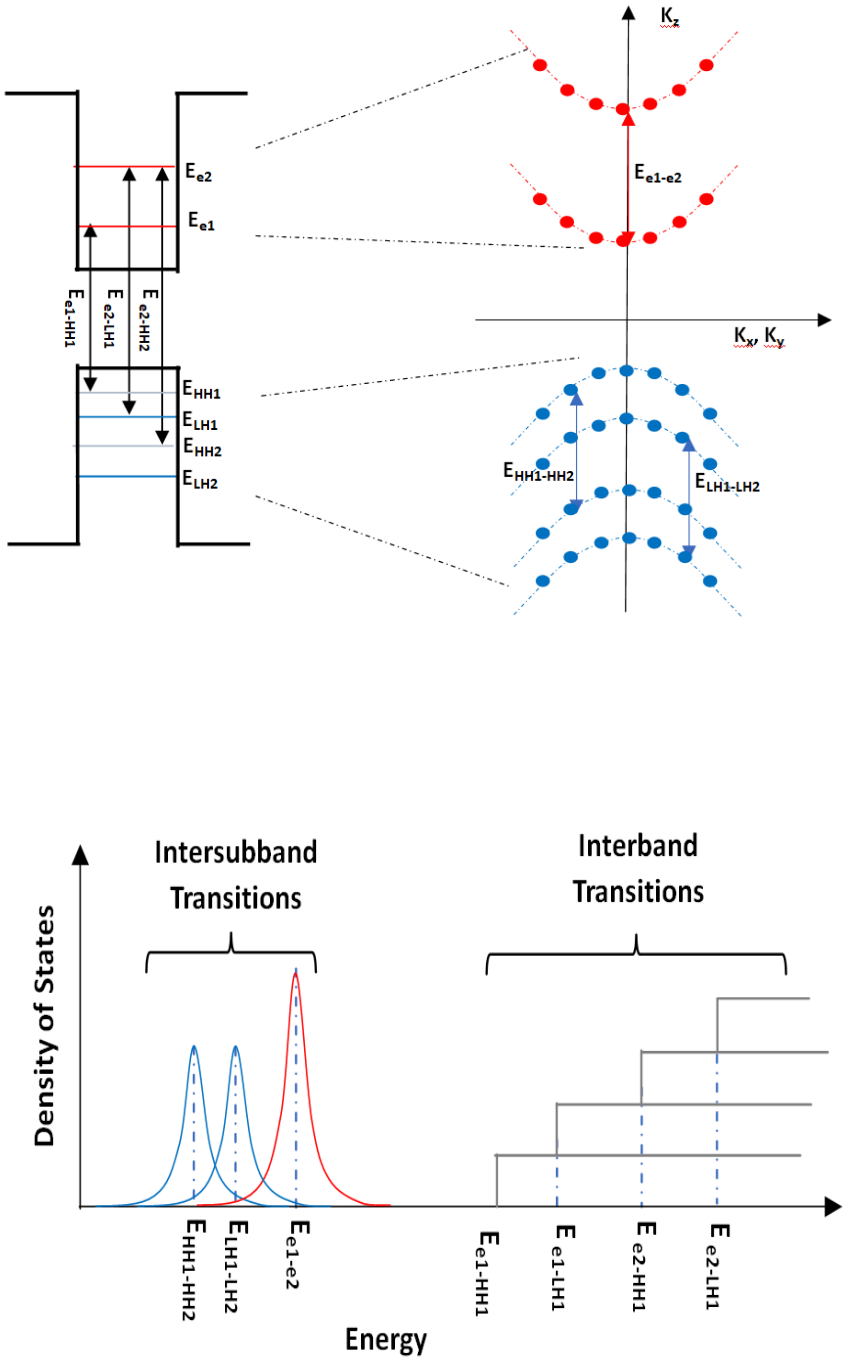

Figure II.9 The schematic diagram for finite quantum well type-I a) illustrations of permitted Intersubband and Interband transitions b) the density of states for Intersubband and Interband transitions.

Similar to Interband Cascade devices, the Quantum Cascade family despite the theoretical proposals and simulations of Quantum nanostructure for TPV cells [61], none have been documented empirically. In Presence of Auger and SRH mechanisms gives a thermal generation rate that is expressed as [62]:

$$g_{th} = \frac{n_i^2}{N_a \tau_A} + \frac{n_i^2}{(N_a + n_i)\tau_{SRH}} = \frac{n_i^2}{N_a \tau} \qquad \text{II.7}$$

$$\frac{1}{\tau} = \frac{1}{\tau_A} + \frac{N_a}{(N_a + n_i)} \frac{1}{\tau_{SRH}} \approx \frac{1}{\tau_A} + \frac{1}{\tau_{SRH}} \qquad \text{II.8}$$

where τ represents the carrier lifetime due to the Auger mechanism and τ_{SRH} is the SRH carrier lifetime. Equation II.7 is valid if the doping concentration Na is much higher than the intrinsic carrier concentration ni. Therefore, one can first extract g_{th} from Equation II.7 and then calculate the carrier lifetime from Equation II.8. The contribution of SRH process can be indirectly assessed by the activation energy E_a.

Figure II.10 shows the temperature dependence of Auger and SRH recombination. This suggests that carrier movement was influenced by both the diffusion process and the SRH processes [61]. For SRH recombination is related to the presence of multi-Energy level defects within the material. Which is influenced by the density of states and the ability of carriers to recombine via these defect states. The observed peak suggests that for intermediate quantum well widths, the carrier dynamics and the defect states are most favorable for SRH recombination. As temperature increases, the carriers gain more thermal energy, which can affect the interaction with deep-level states, thereby shifting the peak of SRH recombination to wider wells. For Auger recombination involves three carriers and is typically more significant in narrow quantum wells due to the higher carrier concentration. As the well width increases, the carrier density decreases, which leads to a reduction in Auger recombination. the decrease with increasing temperature is anticipated because thermal effects at higher temperatures reduce carrier localization and reduce the recombination efficiency.

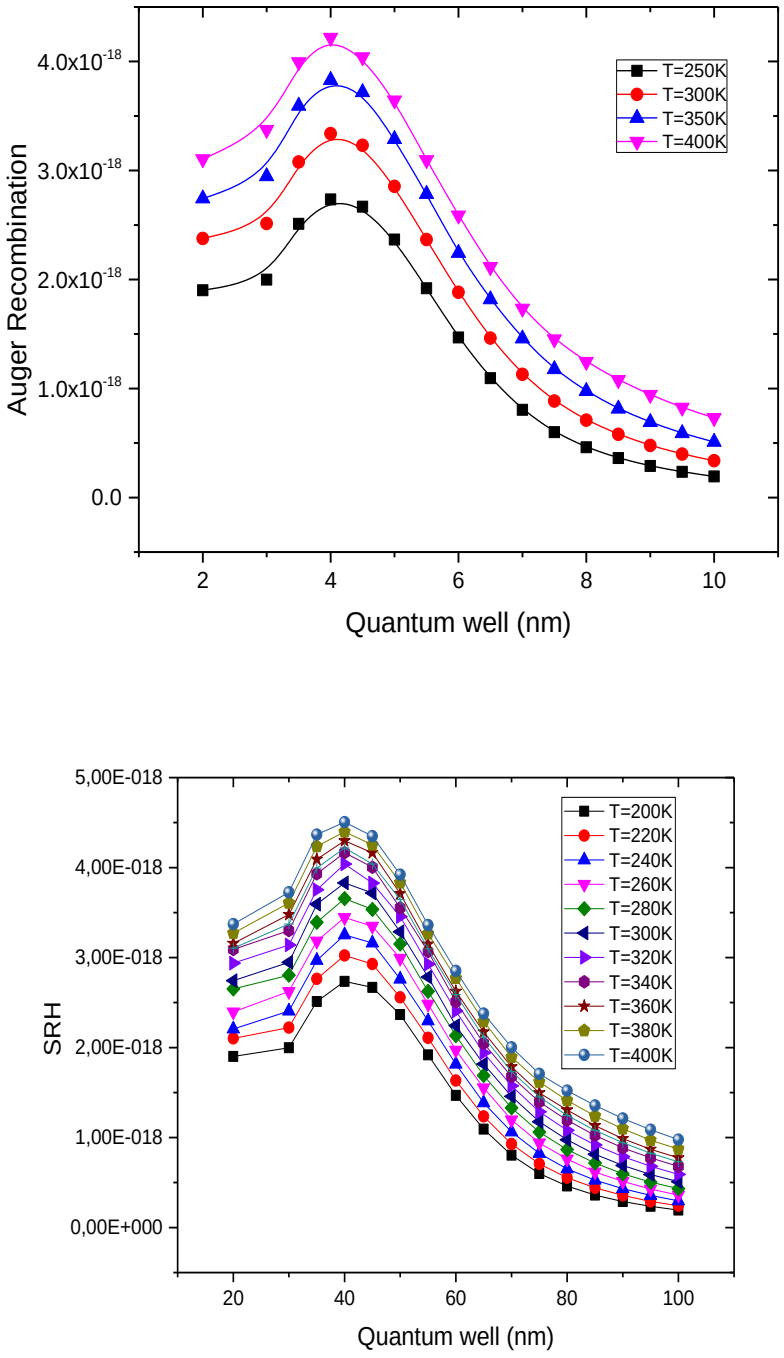

Figure II.10 The variation of Auger recombination and SRH (Shockley-Read-Hall) recombination as a function of the quantum well width at different temperatures.

Auger recombination shown in figure II.10.a refers to a recombination process in which the energy released by recombination is transferred to another charge carrier, which then relaxes back to its original energy level through lattice collisions. Auger recombination is particularly effective in highly confined semiconductors.

Shockley–Read–Hall recombination shown in figure II.10.b refer to impurities and defects in a semiconductor can create energy levels within the bandgap. These energy levels facilitate a two-step recombination process. For example, an electron from the conduction band can first occupy a defect level and then relax from there to the valence band, releasing its energy in the form of phonons. This defect-related recombination, also known as Shockley–Read–Hall recombination (SRH recombination), depends on the crystal quality of the semiconductor material.

The design process for QCDs is examined in relation to the detection wavelength, detectivity, and responsivity wich is related to the splitting between the discret energy level. A more extensive theory about Intersubband ISB transitions figure II.9. Conduction band ISB devices, including QCDs, rely on photon–electron interactions among quantised electron subbands inside the conduction band of semiconductor heterostructures. The same happened in the valence band but with existence of more other energies for different types of hole's effective mass figure II.9.

Their spectral response is optimal at the energy difference between two quantised electron levels in a quantum well. In contrast to semiconductor devices reliant on interband transitions, where the operating wavelength is approximately determined by the bandgap of the semiconductor material, the operating wavelength of intersubband (ISB) structures is typically dependent on the thickness of the quantum well (QW) Figure II.10. The transition energy between the two lowest electron levels in a quantum well as a function of the quantum well thickness, derived from numerically solving the Schrödinger equation for the quantum well, which is done in the next chapter (chapter III).

VIII. Conclusion

We have defined the application of nanostructured materials to enhance the thermoelectric performance. The combined method of lowering electron scattering and maximizing heat-conducting phonon scattering overall length scales by nanostructuring methods generated several enhanced figures of merit. The nanostructuring techniques include many creative ideas of multiscale phonon scattering. The most sensible approach to raise ZT higher is to favorize the intersubband transition. Where the intersubband characteristics of infrared transitions in nanostructured detectors necessitate precise control over both the pounded state and the excited state to design for a certain peak wavelength. The transitions may occur from bound-to-bound states, exhibiting a narrow spectral response, or from bound states to the continuum, displaying a broad spectral response, contingent upon the relative location of the excited energy of interest.

research is required to commercialize nanostructured materials, 2D structures are captivating methods to improve the figure of merit. However, these methodologies rely on the basic features of the material, including carrier concentration, mobility, and the behavior of phonons, such as the mean free path of the phonons. Further study to achieve a better quantitative comprehension of thermoelectric materials for a broad spectrum of power applications will be explored in the next chapter.

Chapter III

Thermophotovoltaique cells based on III-V materials design and Engineering

I. Introduction

The design, manufacture, and characterization of a quantum well thermophotovoltaic able to simultaneously detect Infrared and visible radiation are described in this chapter. Whereas IR depended on intersubband transition, visible light detection was achieved by interband transition. Self-consistently solving the Schrödinger and Poisson equations with the shot approach allowed to model the quantum well structure, first we start by optimizing the architectures by calculate all the structural proprieties while preserving the notion studied in the previous chapter such as confinement, use of materials with high figure of merit, the aim is to select materials with a high figure of merit displaying similar compatibility behaviors. The traditional III-V semiconductor material used in quantum well infrared photodetectors (QWIPs) are based on GaAs families. Detectors that use this material system can have their spectral response adjusted between 6 and 20 μm. Most of the energy gap discontinuities in that combination are in the conduction band. Consequently, quantum well infrared photodetectors based on GaSb families may be able to achieve intersubband absorption at much lower wavelengths. The n-doped QWIPs show no sensitivity to radiation. On the other hand, due to band mixing, QWIPs that use inter-valence band transitions are sensitive to normal incidence radiation. Quantum well infrared photodetectors (QWIPs) doped with n and p have been built and combined.

II. Properties III-V materials based antimonides

III-V based antimonides materials families are currently of great interest because they are very promising in many new optoelectronic devices and especially, in solar applications as thermo-photovoltaic cells. As we have seen that several new materials have been discovered very recently with a figure of merit of 2 to 3. However, their application in industry still requires many efforts. These efforts would include improvements in their chemical and thermal stability, as well as their synthesis methods and production costs.

II.1. Structural properties

For a reliable simulation, the most accurate knowledge possible of the materials contained in the thermophotovoltaic cells is necessary.

The material parameters of GaSb and III-V semiconductor materials fit in to the families of antimonides shows zinc blende crystal structures figure III.1. GaSb,InSb,AlSb and InAS,GaAs materials have mainly low lattice constant discrepancies and similar growing conditions as their benefits [63,64]. These binary materials could be combined to obtain ternary alloys InGaSb, AlGaSb, or quaternary such as InGaAsSb and AlGaAsSb, required for modeling are discussed below. the bandgaps of these materials and their associated alloys varies from 0.17 eV (for InSb) to 1.70 eV (for AlSb). In the design of TPV nanostructured Photodetector's devices, this bandgap range is quite important.

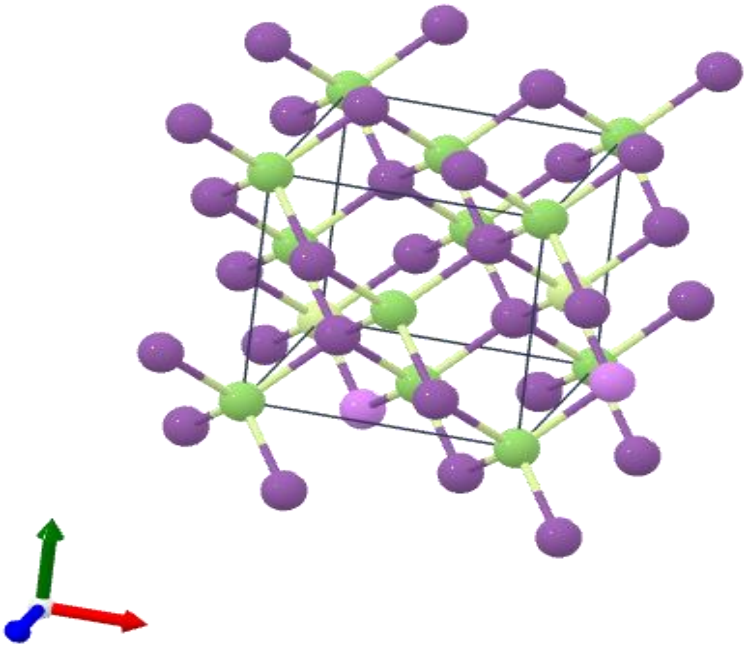

Figure III.1: zinc blende crystal structure of GaSb.

Despite these spectacular results, current commercial thermoelectric modules are still based on conventional materials, such as compounds based on Bi-Te, Pb-Te for near ambient temperature,

or Si-Ge, Heusler and stekrudit materials for high temperature appliocations. Indeed, in addition to the search for figure of merit optimization, economics and the environment are important factors to consider for industrialization. These materials must address the issues of cost and toxicity. From this perspective, the basic compounds, Bi-Te, Pb-Te, are unfavorable because Pb is a toxic element and banned in several countries.

II.2. Electronic properties

Most of III-V materials is chemically stable, GaSb and his derived materials are motivated by several applications [63] such as gas sensors, transparent conductors (TCO - Transparent Conducting Oxide), … In the following part, we will present the physical properties of III-V materials based on antimonides, which is generally growth in cubic phase figure III.1.

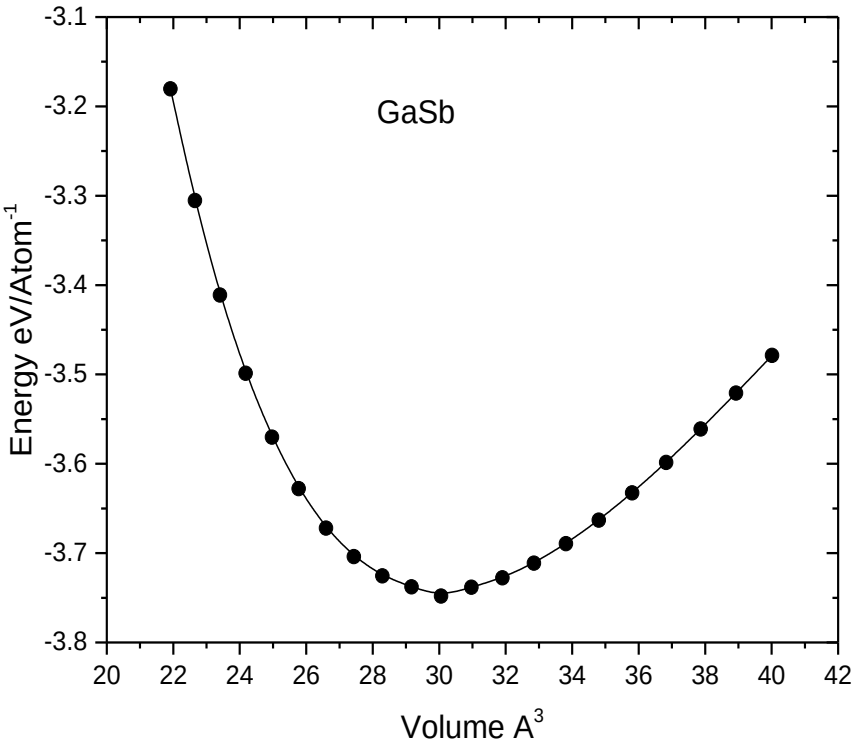

Figure III.2: Variation of total energy versus volume of unit cell volume for GaSb.

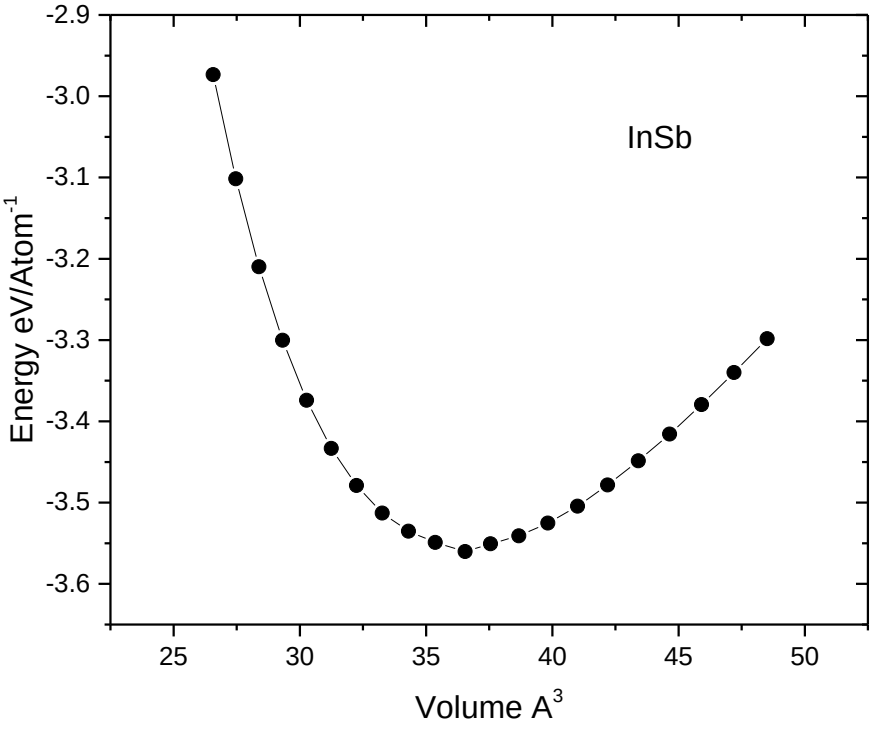

Figure III.3: Variation of total energy versus volume of unit cell volume for InSb.

The most stable (equilibrium) configuration is represented by the minimum point on the energy vs. volume curve figureIII.2 and figure III.3. for both GaSb and InSb a stable crystal structure is indicated by the curve's parabolic shape close to the minimum. Their total energy vs. volume profiles will resemble each other almost exactly because of their similar bonding and structural parameters. The band structure of both materials is similar figure III.4, while Both are narrow bandgap semiconductors InSb (~0.17 eV) and GaSb (~0.72 eV).

The band structure of GaAs and InAS are also similar figure III.4, for the same reasons

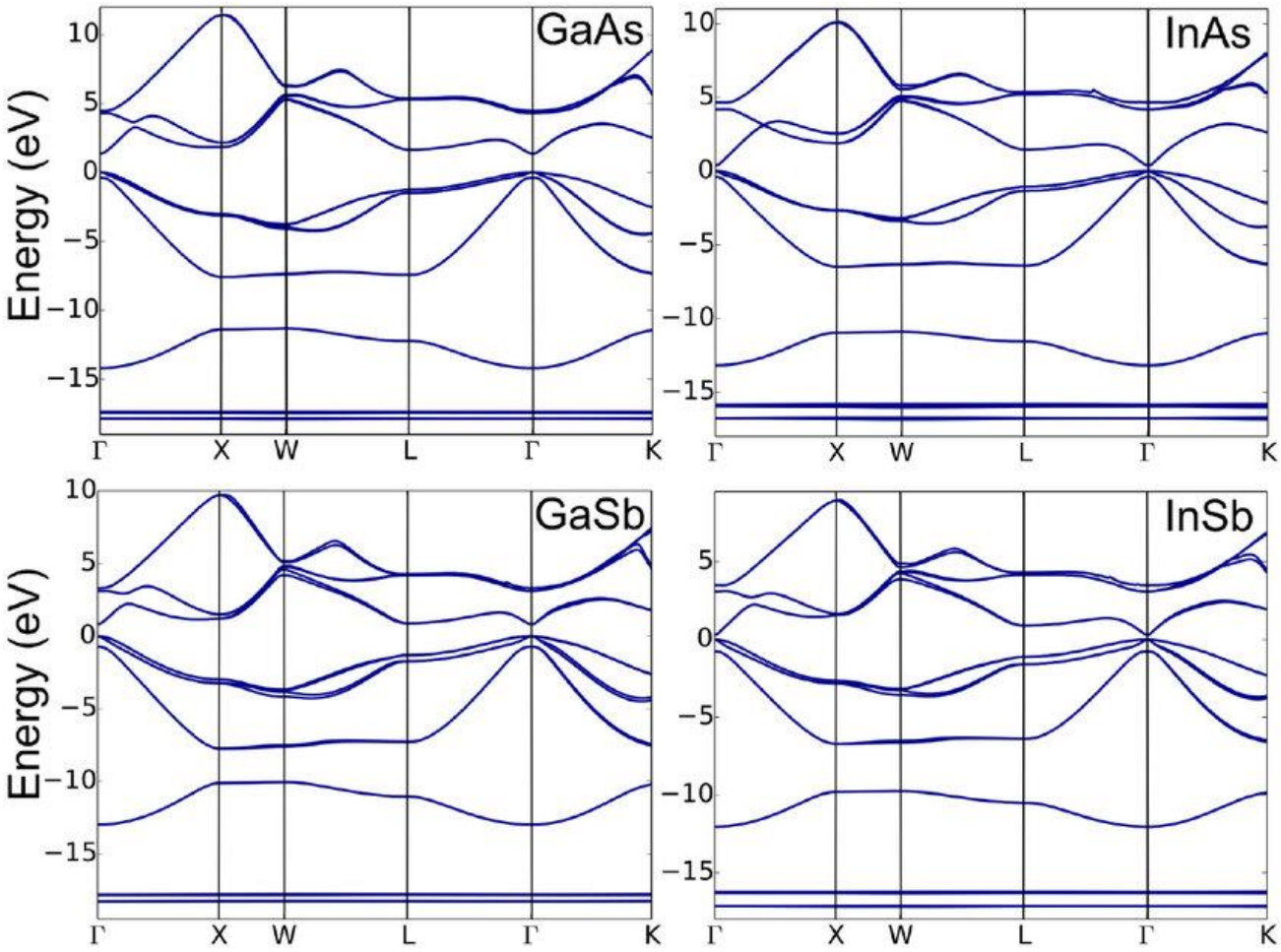

Figure III.4: Band diagram and density of state for GaAs, InAs, GaSb and InSb [65].

The valence band maximum and the conduction band minimum are located at the same point in the Brillouin zone. Detection efficiency and light emission are then high since radiative transitions are very probable. This property makes these materials useful for optoelectronic devices such as light-emitting or light detecting diodes [66]. From the Γ point (point of haut symmetry), there is another minimum (E_L) in the <111> direction, which lies only slightly above the minimum at the Γ point. $\Delta E_{\Gamma\text{-}L}$ denotes the difference between these two minima.

II.3. Energy variation as function of temperature

A better understanding of the band structure of III-V materials is therefore essential. The values of $\Delta E_{\Gamma\text{-}L}$ reported in the literature are in the range 0.85 meV [66]. The temperature dependence of the band gap E_g is given by:

$$E_g = E_g(0) - \frac{\alpha T^2}{T + \beta}$$

where $E_g(0)$ is the energy gap at 0°K, β is approximately the 0°K Debye temperature, and α is an empirical constant.

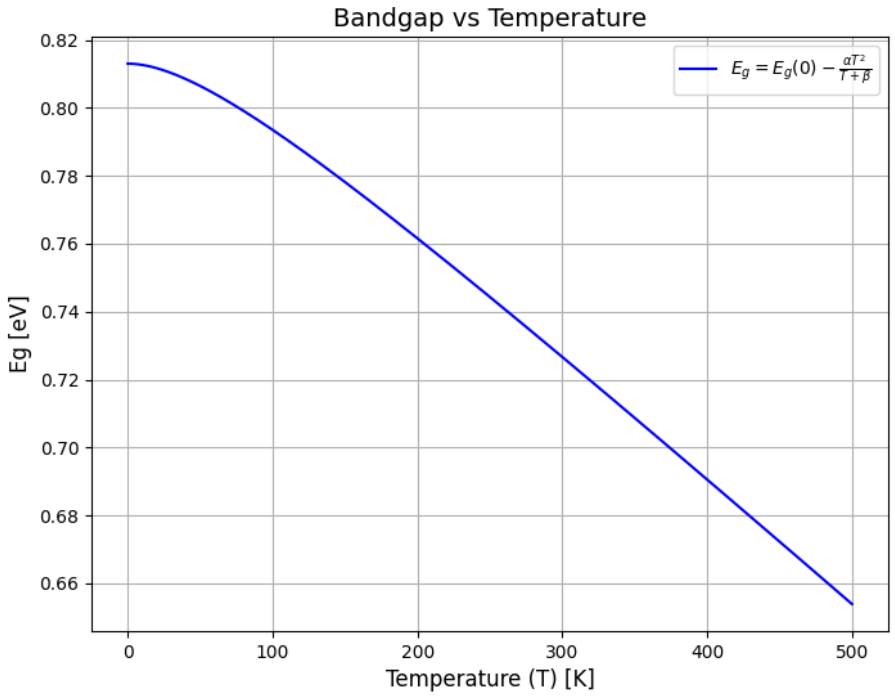

Figure III.5: Variation of the energy gap as function of temperature variation.

A full understanding of the intrinsic charge carrier concentration n_i is essential for accurately characterizing a semiconductor device. The intrinsic charge carrier concentration is dependent upon the effective densities of states of the conduction and valence bands, N_C and N_V, the band gap, Eg, and the temperature T.

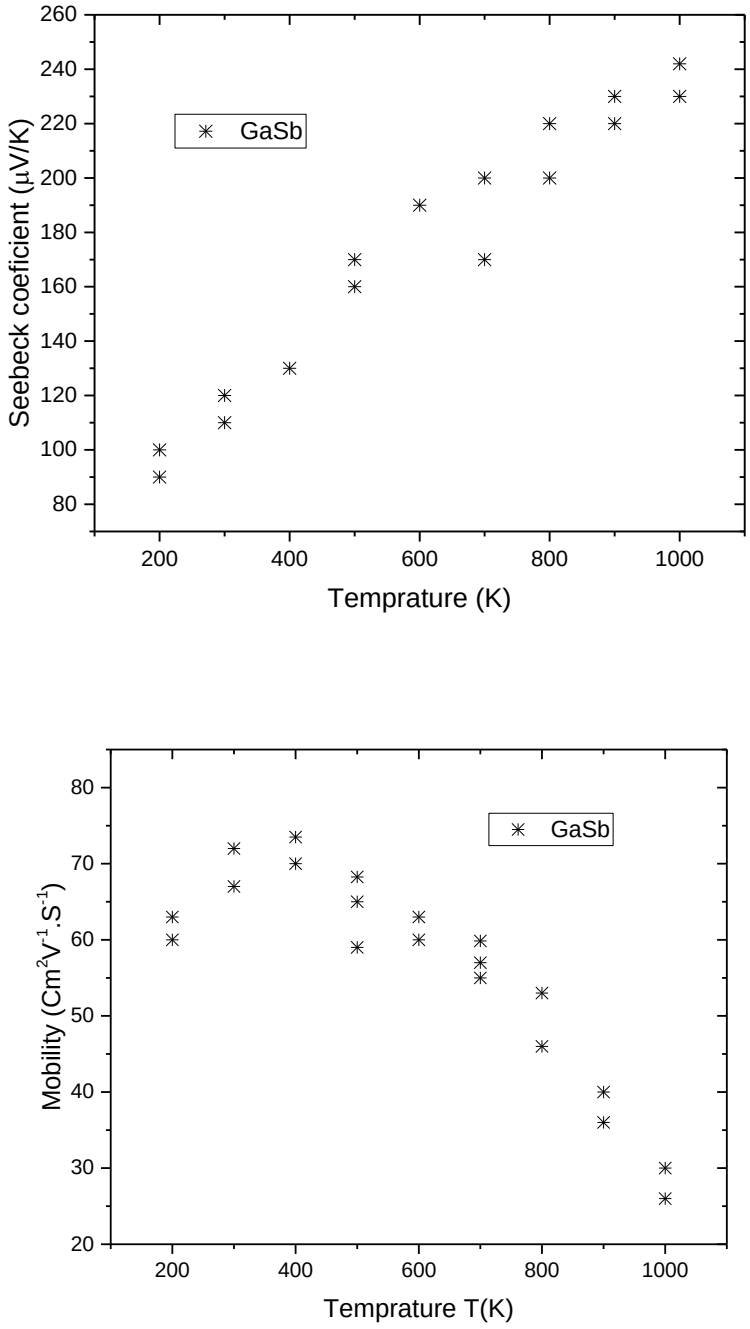

Figure III.6: a) Temperature dependence of Seebeck coeficient in GaSb.

b) Temperature dependence of mobility in GaSb.

By way of temperature increase, Seebeck coefficient increases, which is beneficial for thermoelectric performance but from the second graph we observe the mobility decreases, which can reduce electrical conductivity. This trade-off is crucial when optimizing materials for thermoelectric applications, where both high Seebeck coefficient and sufficient mobility (or power factor) are desired, by returning to the equation I.13 & I.15 mentioned in chapter I, a better zT for GaSb will be obtained in the range of temperature 300-500 K.

In the table III.1 the operating temperature range of different materials based on III-V alloys is defined, based on experimental value which Matches well with theoretical predictions.

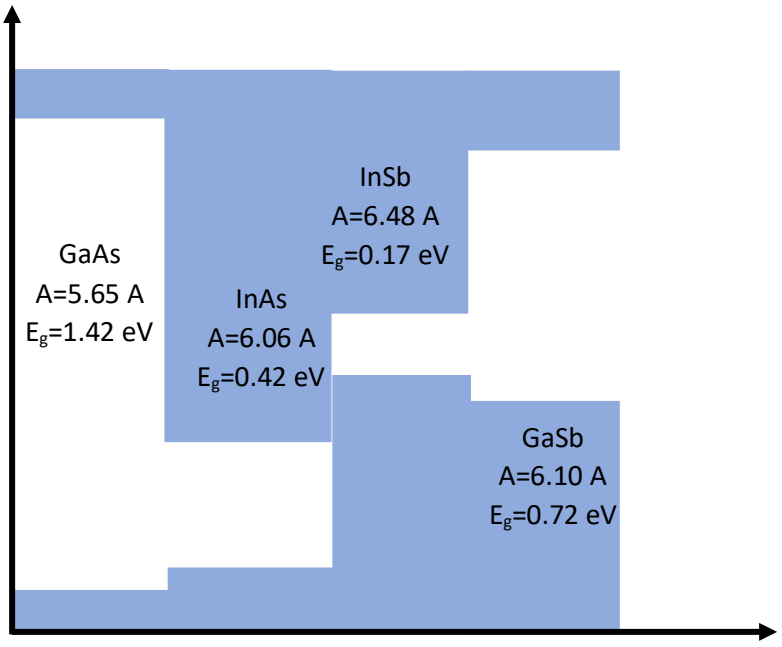

Figure III.7: Band position of GaAs, InAs, InSb, and GaSb binary systems. The values are obtained from Ref. cited in the table below.

Table III.1: Survey of thermophotovoltaic technologies grouped according to absorber material.

Material	InAsSb	InSb	InAs	InAs	InAsSbP	InGaSb	GaInAsSb	GaInAsSb	InGaAs	InGaAs	GaSb	GaSb	Ge	Si
E_g (eV)	0.286	0.23	0.36	0.32	0.35	0.56	0.549	0.53	0.74	0.6	0.73	0.73	0.66	1.1
Cell T	27 °C	77 K	300 K	20 °C	21 °C	27 °C	27 °C	27 °C	30 °C	25 °C	25 °C	25 °C	300 K	300 K
Illumination	1500 K	1248 K IR	800 °C	950 °C	N/A	1373 K	arc lamp	950 °C SiC	3250 K	1039 °C tungsten	1350 K blackbo	1200 °C	1100 °C tungsten	2300 °C radiator
Spectral	without	without	without	without	without	without	without	front surfac	front surfac	front surface	perfect band	front surfac	front & back	N/A
J_{sc} (A/cm	39.88	7.2E-3	0.23	0.89	0.25	3.0	3.5	2.9	0.288	0.1	3.0	2.83	1.67	9.52
FF (%)	N/A	64%	25%	37%	34%	61%	66%	67%	65%	66.2%	75%	73%	67%	N/A
V_{oc}	162.8	83 mV	17.4 mV	60 mV	120 mV	270 mV	313 mV	306 mV	405 mV	12.5 V	500 mV	477 mV	356 mV	N/A
P_{out} (W/c	N/A	3.8E-4	1E-3	0.02	0.024	0.49	0.723	0.58	0.08	0.79	1.26	0.98	0.4	10
Efficiency	projected	N/A	0.35 %	3%	0.18 %	N/A	N/A	19.7%	12.4 %	24%	projected 30%	21%	16%	26%
Reference	[67]	[68]	[69]	[73]	[72]	[71]	[74]	[39]	[70]	[68]	[69]	[63]	[67]	[34]

III. Material optimization

The III–V family based on antimonide alloys were employed since, these materials offered optimal narrow bandgap energy while keeping the lattice-matched condition and therefore enabling designs shown in Figure III.7. An approach based on the band diagram and strain engineering to obtain type I quantum wells based InGaAsSb/AlGaAsSb [80] for infrared detector on GaSb substrate, took into consideration a quantum well type I, lattice-mismatch within 2% (circles in Figure III.8, and good band offset to gain good confinement for both electrons and holes (Table III.2). A study on the optimization of the materials was done using a quaternary alloy formed by the two families of III-V semiconductors, arsenide and antimonide.

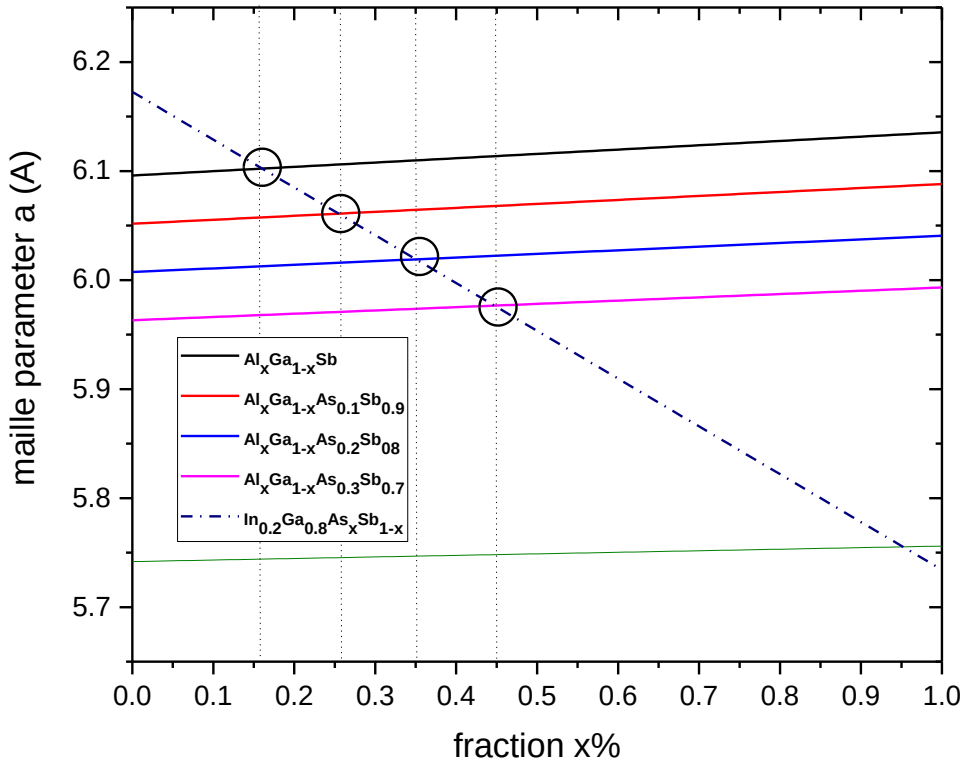

Figure III.8: Calculation of the $Al_xGa_{1-x}As_ySb_{1-y}$ /$In_{0.2}Ga_{0.8}As_xSb_{1-x}$ maille parameter as function of composition.

The structure was made on a GaSb substrate followed by an N-type GaSb layer and then a buffer layer of AlGaAsSb to ensure mesh agreement with the active zone which will constitute multi-quantum wells AlGaAsSb/InGaAsSb, then a second buffer layer was made by AlGaAsSb with a concentration different from that on the first terminal, to ensures the mesh agreement between the active zone and the second pole of the junction which is a typical GaAs layer P-type. The first part of our work seeks to find the best adjustment of the energy gap according to the lattice mismatch, the composition dependence of the lattice parameter.

The dashed line in Figure III.8 shows the variation of the lattice parameter of InGaAsSb as a function of As concentration by taking a low fraction of indium 20% in the wells to obtain a narrow band gap. And demonstrates how the lattice parameter of AlGaAsSb can vary depending on the lattice parameter for the Al composition in the barrier and the As composition in the well with a significant amount of GaSb up to 50% to gain the good thermal proprieties of antimony alloys [2] and cut the compressive strain [82].Figure III.8 shows a good mesh agreement for different values, indicating that several options are available as designated by circles. Maintaining good mesh agreement is an iterative process; require multiple iterations of mesh enhancement and analysis to achieve accurate results, as overly sophisticated find a good mesh with desired proprieties can lead to longer simulation times.

The bandgap energies of the InGaAsSb quaternary system range from 0.17 eV for InSb to 1.42 eV for GaAs, whereas the energy gap of AlGaAsSb fluctuates between 0.72 eV for GaSb to 2.30 eV for AlSb [83]. The fluctuation depicted in Figures III.9 and III.10 of E_G exhibited a non-linear tendency; for $In_xGa_{1-x}As_ySb_{1-y}$, the energy gap significantly diminishes with increasing indium percentage, maintaining the lattice misfit within an acceptable limit of $\Delta a/a < 2\%$, whci led to a tight bandgap range of $0.5\ eV < EG < 0.7\ eV$.

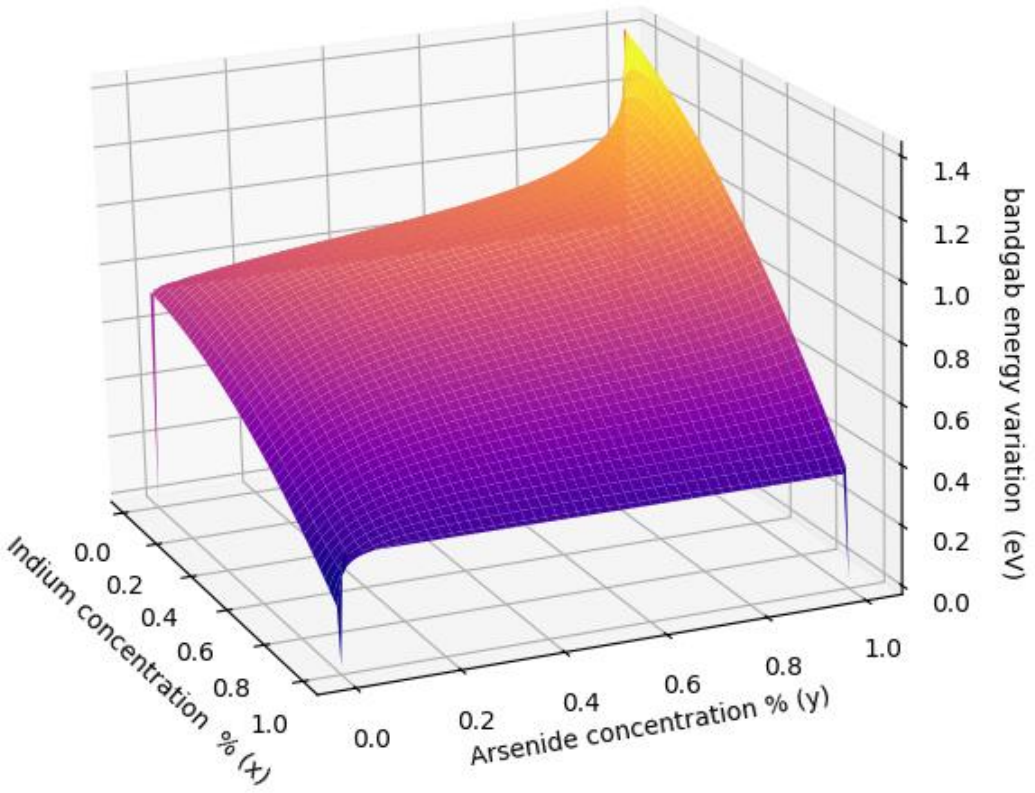

Figure III.9: Variations of the gap energy as a function of x (% In) and for different y (% As).

It is intended to have a significant antimony content above 0.5, which means that x and y must be limited to less than 25% indium and 30% in arsenic, respectively [84]. As shown in Figure III.8, the lattice parameter is strongly impacted by the x value in aluminium and especially by the y value in arsenic, while the barrier AlGaAsSb energy gap is primarily determined by the percentage of aluminium. We need to enforce values of y < 30% in order to implement quantum wells using InGaAsSb on an AlGaAsSb barrier system.

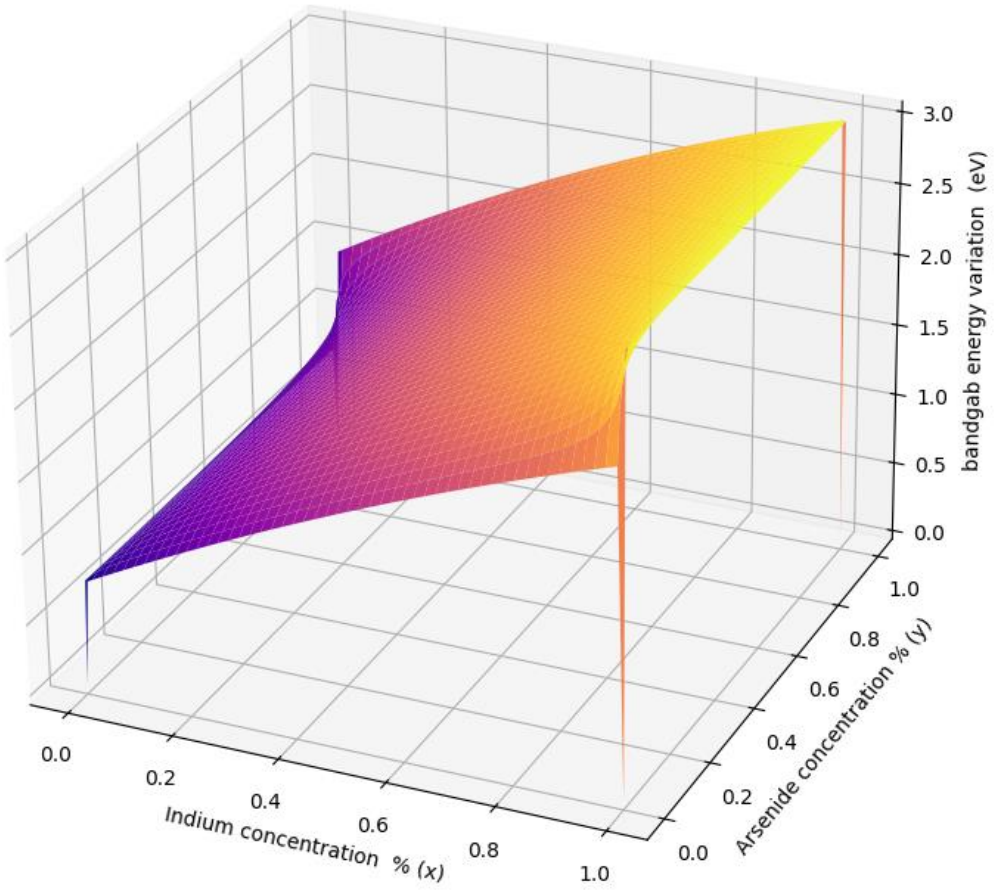

Figure III.10: Variations of the gap energy as a function of x (% Al) and for different y (% As).

Additionally, as shown in Table 1, the high indium fraction of 20% and the elevated arsenic fraction of up to 10% in the quantum wells cause the conduction band and valence band of the barrier to be displaced, resulting in improved confinement. As the compressive strain caused by this condition, careful strain balancing is required. In order to develop high-performance photodetectors based on InGaAsSb/AlGaAsSb type-I superlattices, we propose a number of superlattice designs for quantum wells and barriers. We used a theoretical model to calculate the

band offset. When the bandgap is increased to 0.4 eV, it is possible to achieve a conversion efficiency of 30% with a multijunction architecture even for a small width. This elucidates that multijunction architecture is an effective strategy to universally improve the device performance in a wide infrared spectral range.

III.1. Band-edge alignments

Type I quantum wells can be created in a variety of ways using the material systems listed in Table 1, which enable the construction of multiple quantum wells integrated within a PIN junction [83]. This material system, which can be grown lattice-matched on GaSb and/or GaAs substrates, may improve conversion efficiency, a highly desired property [85].

Figure III.2: The scheme of the layer's composition in the investigated samples.

sample	A	B	C	D
QW	$In_{0.2}Ga_{0.8}As_{0.15}Sb_{0.85}$	$In_{0.2}Ga_{0.8}As_{0.25}Sb_{0.75}$	$In_{0.2}Ga_{0.8}As_{0.35}Sb_{0.65}$	$In_{0.2}Ga_{0.8}As_{0.45}Sb_{0.55}$
Barrier	$Al_{0.15}Ga_{0.85}Sb$	$Al_{0.26}Ga_{0.74}As_{0.1}Sb_{0.9}$	$Al_{0.35}Ga_{0.65}As_{0.2}Sb_{0.8}$	$Al_{0.45}Ga_{0.55}As_{0.3}Sb_{0.7}$
ΔE_C (eV)	0.21	0.34	0.42	0.62
ΔE_V (eV)	0.06	0.17	0.30	0.24

IV. Device design and fabrication

To reach high performance PIN photodetectors, it should overcome two principal challenges. The first one resides in choosing an InGaAsSb/AlGaAsSb system with a NIR cut-off wavelength and theoretically giving a high absorption coefficient. At the same time, the superlattice design must give a good strain balance to ensure a high-quality material for a long minority carrier diffusion length in order to achieve high quantum efficiency (QE) [86].

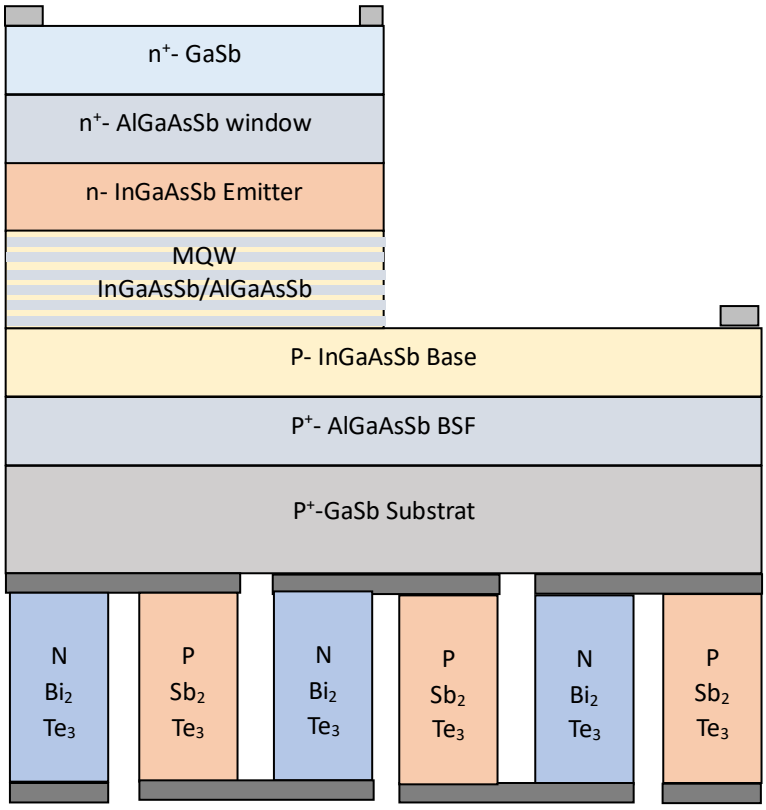

Figure III.11: Structure of a PIN thermophotovoltaic solar cell with multi quantum wells using cascade nastructure for photovoltaic cell and micro cascade structure to improve thermoelectric conversion.

In order to obtain high quantum efficiency, superlattice design must provide appropriate strain control to guarantee a high-quality material with a long minority carrier diffusion length. The second challenge is in designing a highly controllable barrier which effectively blocks the majority electrons in the conduction band while ensuring the free movement of minority holes in the valence band.

V. Schrodinger equation resolution for quantum well

The calculation procedures mentioned in the last section of chapter II described here by follows the envelope function approach based on the effective-mass approximation [82]. to obtain in-plane sub band dispersions in the conduction and valence band. The Schrodinger equation for a particle of mass m confined in 1D potential well in an electric field E perpendicular to the quantum well layer is given by the relation (III.3) [83]:

$$i\hbar \frac{\partial \psi}{\partial t}(x,t) = \left(-\frac{\hbar^2}{2m}\frac{\partial^2}{\partial x^2} + V(x) \right) \psi(x,t) \tag{III.3}$$

ψ describes the time-dependent Schrödinger equation (how the wave function changes over time), while φ describes the time-independent Schrödinger equation (stationary states).

The set of energies E_n and stationary states φ_n , form the eigenvalues and eigenstates of the Hamiltonian operator

$$\hat{H}\varphi_n = \left(-\frac{\hbar^2}{2m}\frac{\partial^2}{\partial x^2} + V(x) \right) \varphi_n = E_n \varphi_n \tag{III.4}$$

We use the effective mass approximation to calculate the energy states for a quantum well [6].

$$\left(-\frac{\hbar^2}{2m^*}\frac{\partial^2}{\partial x^2} + V(x) \right) \varphi_n = E_n \varphi_n \tag{III.5}$$

$$\varphi^{"}(x) = \frac{2m^*(V_0 - E)}{\hbar^2}\varphi \tag{III.6}$$

$$\varphi^{"}(x) = -k^2\varphi \tag{III.7}$$

$$\begin{cases} k = \sqrt{\frac{2m^*_{e,h}E}{\hbar^2}} - \frac{L}{2} \le x \le \frac{L}{2} \\ k = \sqrt{\frac{2m^*_{e,h}\,(E-V_0)}{\hbar^2}} \; x > \frac{L}{2} or x < -\frac{L}{2} \end{cases} \tag{III.8}$$

$$\sqrt{2m^*_{e,h}E_n}\left(\frac{L}{\hbar}\right) = n\pi \tag{III.9}$$

$$E_n \le \Delta E_{C,V} \tag{III.10}$$

We obtain

$$E_n = \frac{n^2\pi^2}{2m^*_{e,h}}\frac{\hbar^2}{L^2} \quad \text{(III.11)}$$

$n = 1, 2$ .... Energy level, $m^*_{e,h}$ effective mass of electrons, holes respectively.

L: the width of the well, $\hbar = h / 2\pi$.

$$\varphi_n = A \sin\left(\frac{n\pi z}{L_z}\right) \quad \text{(III.12)}$$

So, the number of energy states n is given by the relation:

$$\sqrt{2m^*_{e,h}\Delta E_{C,V}}\left(\frac{L}{\hbar}\right) > n \quad \text{(III.13)}$$

The number of the discrete energy levels n is strongly depends on the value of the offset band $\Delta E_{C,V}$, the effective mass of the carriers $m^*_{e,h}$ and the width of the well L. All the possible direct transitions are calculated as a function of QW width to recognise how to design devices for different wavelength section.

self-consistent Schrödinger-Poisson computations were conducted utilising the material parameters defined in table III.2. Nonparabolicity was considered via an energy-dependent effective mass. Based on this calculation figure III.11. and table III.2. lists the layer sequences for a single active area period. Using 7-15 repetitions of QW the active region period based on theckness of QWs, two thick top and down contact layers, all layers were fabricated using molecular beam epitaxy on GaSb substrate. For the resonant quantum well in the active zone. The high energy transition is limited in QW without shifting, so localising wave functions in QWs lead to permanently lowering the energy wave function in QW, does not Stark shift, and has a significant wave function for strongly positive fields while the high energy wave function is localised in QW.

VI. Linear optical properties of quantum wells

For a QW, the absorption efficiency noted η_{ab} equation III.14 between two level E_1 and E_2 is related to 2D absorption coefficient noted α_{2D} relation III.15

$$\eta_{ab} = 1 - e^{-N_{QW}\alpha_{2D}} \approx e^{N_{QW}\alpha_{2D}} \quad \text{(III.14)}$$

$$e^{N_{QW}\alpha_{2D}} \ll 1$$

Where α_{2D} is given by the relation

$$\alpha_{2D} = \frac{n_s q^2 \hbar}{2\varepsilon_0 c n m^*} f_{12} \frac{\Gamma}{(E_2 - E_1 - \hbar\omega)^2 + \Gamma^2} \quad \text{(III.15)}$$

$$f_{12} = \frac{2m^* \omega_{12}}{\hbar} |\langle \varphi_1 | \mathcal{Z} | \varphi_2 \rangle|^2 \quad \text{(III.16)}$$

n_s is the active QW's 2-D doping density, n is the refractive index of the QCD, and m* is the effective.

mass in the QW, f_{12} is the oscillator strength between the two lowest wave functions in the active QW, φ_1 and φ_2 is the function of the position along the growth direction $\mathcal{Z}$, and Γ is the half-width of the intersubband transition's Lorentzian absorption shape.

Relation III.15 show that the absorption efficiency and the responsivity thus increase linearly with the number of periods and the doping density. However, since the detector gain is inversely proportional to the number of periods, the current responsivity can be approximately independent from the number of periods.

The in-plane transport is supposed to occur on timescales much shorter than the 1D motion: the subbands are theoretically in thermal quasi-equilibrium state, and the carrier transport becomes moderately spontaneous: all quantum confined states in the z-direction are effectively thermalized creating such a reservoir that exchange electrons with scattering rates calculated through Fermi's rule equation III.16. The time scales and phenomena involved are the quantum decoherence influencing the QCD absorption [87], and Intrasubband thermalisation results from electron-electron scattering, ISB scattering become apparent approximately in very short time some Picoseconds, mostly attributed to electron-LO-phonon scattering when quantum states exhibit significant energy separation. The rapid timeframe governing ISB transmission accounts for both the low working temperature of ISB devices and their inherent high speed.

VII. Conclusion

In this section, we studied the performance quantum cascade photodetectors QCPDs for thermophotovoltaic application, it is a kind of modules that utilize the properties of quantum structures exhibit highly advantageous thermal and optical properties compared to bulk materials. The primary motivation for developing QC photodetectors based on III-V materials was to identify a more cost-effective, high-quality material alternative. One method to reduce the wavelengths of QCDs involved using mixture of high bandgap and wide bandgap III–V materials, which offer significantly elevated conduction band offsets. We demonstrated the benefits of using quantum nanostructures and the influence of their properties on device operation. This implies that quantum nanostructure technology is the best solution for achieving record efficiency values that can exceed 50%, especially with the new concept of photon recycling, which creates discrete energy levels, which promotes inter-subband transitions and reduces non-radiative recombination and thermalization losses. The crucial design aspect of Intersubband devices such as QCDs is the quantum engineering bandstructure. It can be calculated using theoretical calculation of the Schrödinger equation will be explored in the next chapter.

Chapter IV

Performances of Quantum Cascade Photodetectors

I. Introduction

Quantum cascade detectors (QCDs) are photodetectors that require quantum engineering of the electronic band structure to detect photons with energy below the semiconductor bandgap. The integration of long wavelength capabilities with higher material quality makes them a compelling technology for large domain of operation allow detection of photons not only in Visible range but also infrared radiation detection, which makes them very suitable for innovative applications. Quantum cascade detectors (QCDs) emerged since the two last decades as a derivative of two principal technologies in mid-infrared photonics: quantum well infrared photodetectors (QWIPs) and quantum cascade lasers (QCLs). Quantum cascade detectors (QCDs), quantum cascade lasers (QCLs), and quantum well infrared photodetectors (QWIPs) can be classified as intersubband (ISB) optoelectronic transducers, since they depend on intraband transitions between quantum confined states inside the conduction band of semiconductor heterostructures. The in-plane motion affects free electrons, while the z-confined states correspond to two-dimensional (2D) k_x, k_y parabolic subbands. Quantum cascade device bandstructures are created by layering thin films of semiconductors with varying conduction band offsets (Ec) using conventional epitaxial methods, including molecular beam epitaxy (MBE) or metal-organic vapour phase epitaxy (MOVPE) as mentioned in the previous chapter. The most prevalent material system consists is described in the previous chapter, where photodetection transpires as the n-doped optically active quantum wells, responsible for light absorption, are linked to a cascade extractor of restricted states, where effective longitudinal optical phonon scattering produces a directed current. In this section we calculate the optoelectronic and thermoelectric proprieties, such as Interband direct transition and Intersubband transition, lattice thermal conductivity and the electronic transport characteristics.

II. Energy states in a well InGaAsSb/AlGaAsSb

We calculated the restraint level and the variation of the splitting between different energy level of the conduction band BC based on the width of a single well $In_{0.2}Ga_{0.8}As_{0.45}Sb_{0.55}$ on the barrier $Al_{0.45}Ga_{0.55}As_{0.3}Sb_{0.7}$, of the 3rd proposition in table III.2 of chapter 2, where the confinement ΔE_c and ΔE_V is more suitable for better confinement 0,62eV and 0.24eV respectively, We note that for a width of well less than 4nm, the level of confinement E_1 is outside the well, for E_2 from 9nm and

for E_3 around 11nm figure IV.1, we can create a level of confinements, the ratio $\Delta E_0 = E_1 - E_{cp}$ decreases when the width of the well increases, on the other hand the output work $\emptyset_p = E_1 - E_{cb}$, increases to ensure both a good relationship between the confinement level and the work of output from the well, we use well widths between 5nm-20nm.

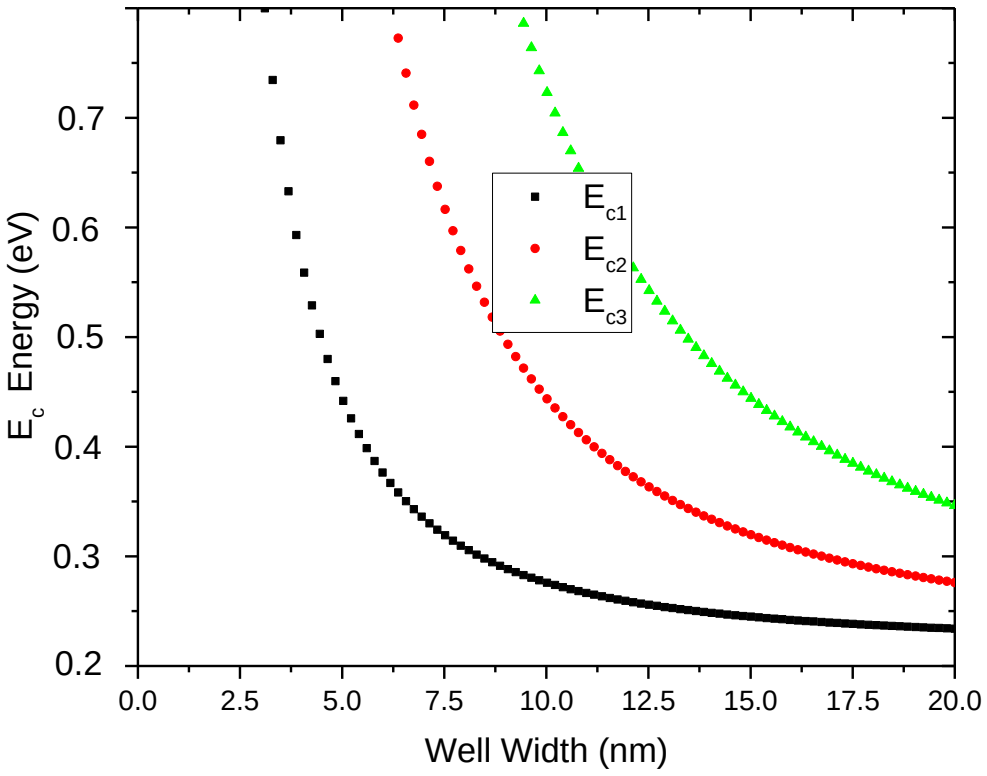

Figure IV.1: The level of confinement in the conduction band as a function of the width of the well for the quaternary InGaAsSb / AlGaAsSb.

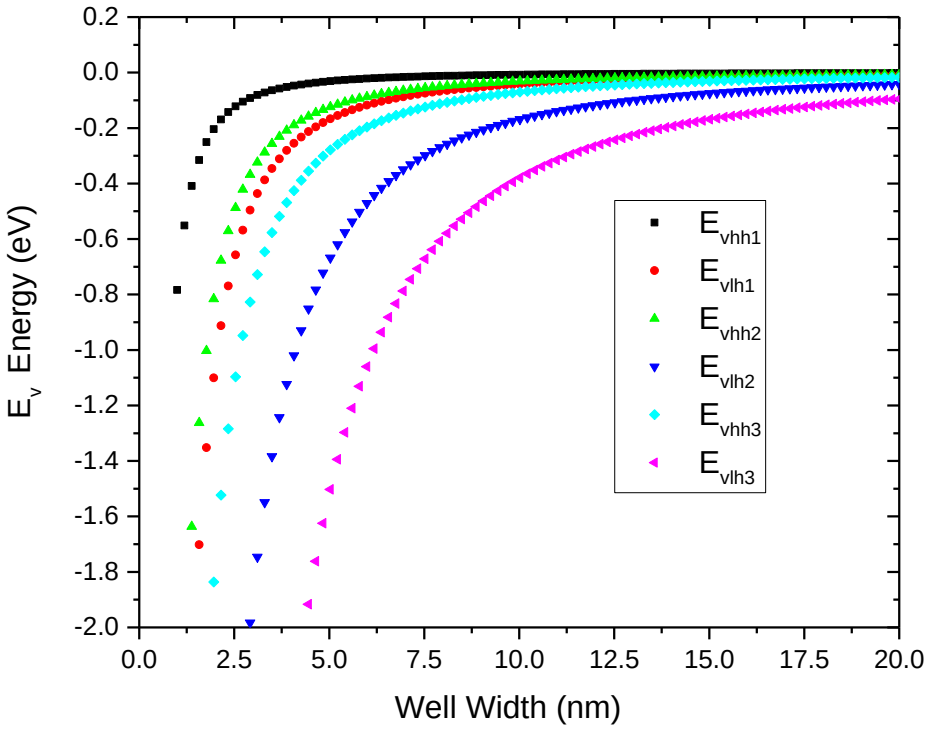

Figure IV.2: The level of confinement in the valence band as a function of the width of the well for the quaternary InGaAsSb / AlGaAsSb.

For the valence band and due to non-parabolicity of the hole masses each level can be divided on two distinct level $E_{v\text{-}hh}$ and $E_{v\text{-}lh}$ as shown in figure IV.2. The binding energies of the heavy- and light-hole excitons as function of well width change rather similarly, no noticeable change in the form of the curve obtained for the dependence of the heavy- and light-hole exciton binding energies on the well width is observed. Whereas the maximum heavy-hole (light-hole) exciton binding energy computed theoretically [94].

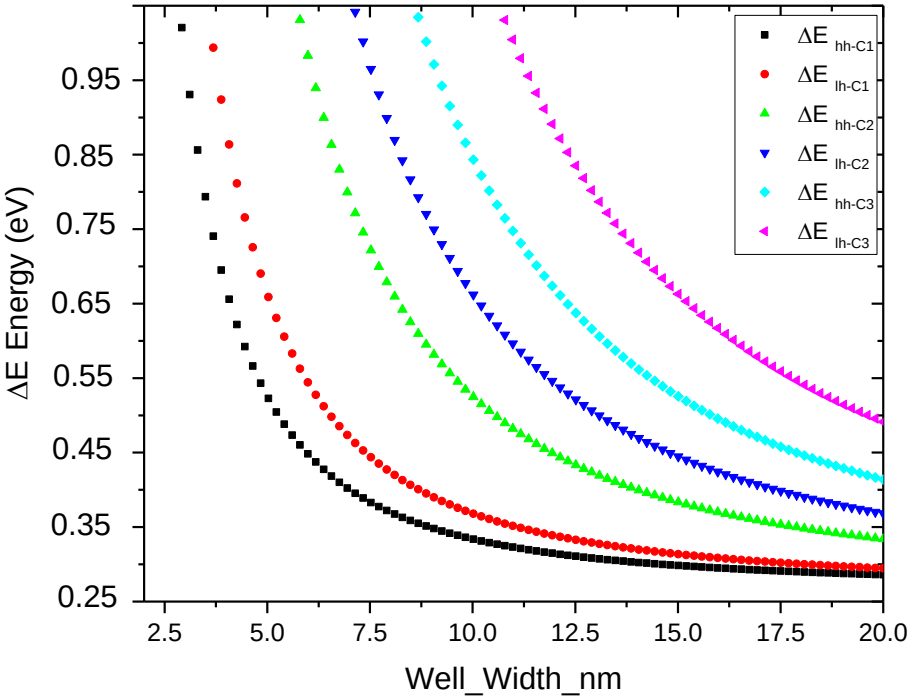

Figure IV.3 : The level of confinement in the conduction band and in the valence band, as a function of the well width and of the level of confinement ΔEC and ΔEV for the quinary InGaAsNSb / AlGaAsSb, for two different concentrations.

The energy positions of the electron and heavy/light hole levels are also represented in figure IV.3. The electronic band structures of $In_{0.2}Ga_{0.8}As_{0.45}Sb_{0.55}/Al_{0.45}Ga_{0.55}As_{0.3}Sb_{0.7}$, and $Al_{0.45}Ga_{0.55}As_{0.3}Sb_{0.7}/GaSb$ demonstrate a type I band alignment with (ΔEc=0,62 meV and ΔEv=0.24 meV), (ΔEc=1.2 eV and ΔEv=0.91eV), respectively at 300 K, demonstrates that the band gap energy diminishes with increasing temperature as discussed in chapter III figure III.5, We can see, that for the three possible energy state, the maximum gain corresponding to the first energy level transition (e_1–hh_1), while the minimum gain corresponding to Bandgap energy of the Barrier, increases non-linearly as a function of the QW width which is in relation with carrier density.

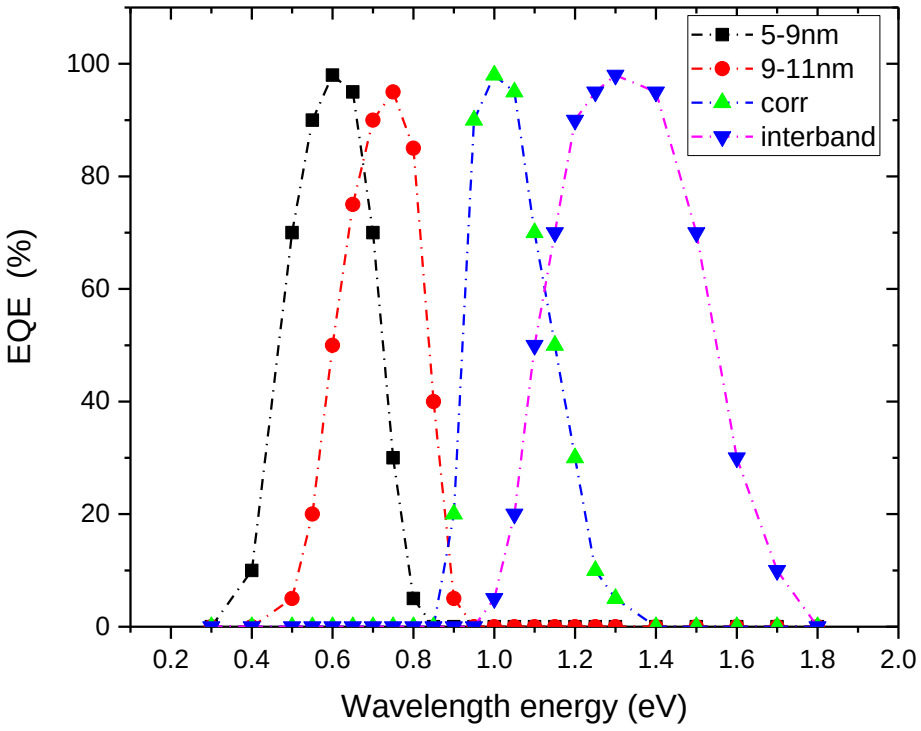

Figure IV.4 : External quantum efficiency (EQE) of maximum power conversion efficiency that a QCD can achieve for optimal transitions as a function of the QW width for the case of $In_{0.2}Ga_{0.8}As_{0.45}Sb_{0.55}/Al_{0.45}Ga_{0.55}As_{0.3}Sb_{0.7}$

The physical requirements for the QCDs are mostly related to current compatibility and alignment with the sun spectrum. In terms of QW engineering, which is essential for examining the most economical techniques for creating novel QCPDs and the possibility of commercial TPV cells, this is extremely demanding. TPV based on III-V QCDs are inherently cost-effective and compatible with low-temperature processing especially those materials based on GaAs and GaSb, two essential factors for high-throughput manufacturing operations. The main feature is the existence of strongly bound exciton states, which have a major impact on several processes in the devices, such as strong absorption (see figure IV.4) and, as a result, the production of photocurrent will be more significant [93].

III. Nanophotonics with 2D transitions

Developments in nanophotonics have since 2012 changed the prospects and high-responsivity Intersubband detectors have been demonstrated. Innovative advancing research and engineering applications depend much on nanophotonic devices. In many different disciplines, including sensing and catching, filters, lasing, nonlinear optics, photodetection, coherent thermal emission…etc., their capacity to offer high spectral resolution and enhanced light-matter interactions makes them interesting [92].

III.1. intersubband transition in conduction band

The selection rule, rather than momentum conservation, requires that only transitions between states with identical quantum numbers in the valence and conduction bands are permitted, as seen in figures IV.5 and IV.6 [88]. Intersubband The spacing between the energy levels for electrons (Figure IV.5) and holes (Figure IV.6) differs due to their distinct effective masses [91].

The primary intersubband optical transitions in CB are depicted in Figure IV.5 as a function of the quantum well width. The transitions were plotted with the barrier width fixed at 0.62eV to maintain strain symmetrisation throughout all the structures demonstrated, as can be observed. The modelling was initiated at 2 nm QW width increments between 2 and 20 nm. The splitting between E_1 and E_2 increases inversely proportional [89] for QW widths between 5nm and 20 nm, as illustrated in figure IV.5. However, the splitting diminishes when the QW width is less than 5nm. This decrease is a result of the correlation between the second energy state and the first and third energy states. furthermore, other transitions are feasible, as indicated in Equation III.10 (chapter III). For example, the number of energy states that can be observed is contingent upon the value of ΔE_C . For a three-level energy system, there are two additional transitions between e_1-e_3 and e_2-e_3. The separation between these levels decreases as the QW width increases, and they will eventually coalesce when the material is in a bulk state.

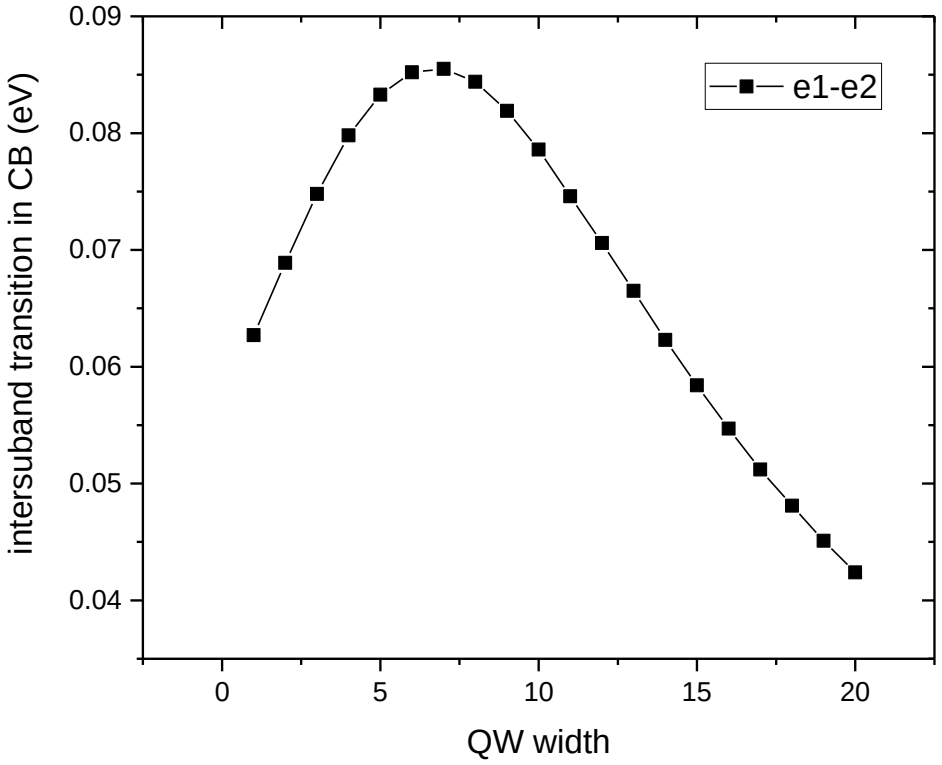

Figure IV.5: Intersubband transitions in conduction-confined energies for electrons as function of barrier thicknesses at 300K.

III.2. Light and heavy holes intersubband transition

Generally, there are two categories of holes with different effective masses in semiconductors. They are referred to as light holes and heavy holes. The differing masses of these two types of holes result in two sets of hole subbands with distinct energy spacings. The light holes possess a significantly smaller effective mass, often akin to that of the electron, and exhibit subband spacing that is greater in comparison to the heavy holes. The heavy-hole to conduction state possesses somewhat lower energy and exhibits closer spacing compared to the light-hole to conduction state. Refer to Figure IV.6. The heavy hole state often prevails in optical absorption for light travelling perpendicular to the quantum well layers [88][90].

Intersubband transitions from heavy hole HH1 to HH2 and light hole LH1 to LH2 yield exclusively z-polarized absorption within the parabolic band approximation [90]. Conversely, HH to LH

transitions occur in three directions—xy and z-polarization; however, the non-parabolicity of the effective masses of holes significantly diminishes xy-polarization due to confinement in the xy directions and sub-band mixing [90].

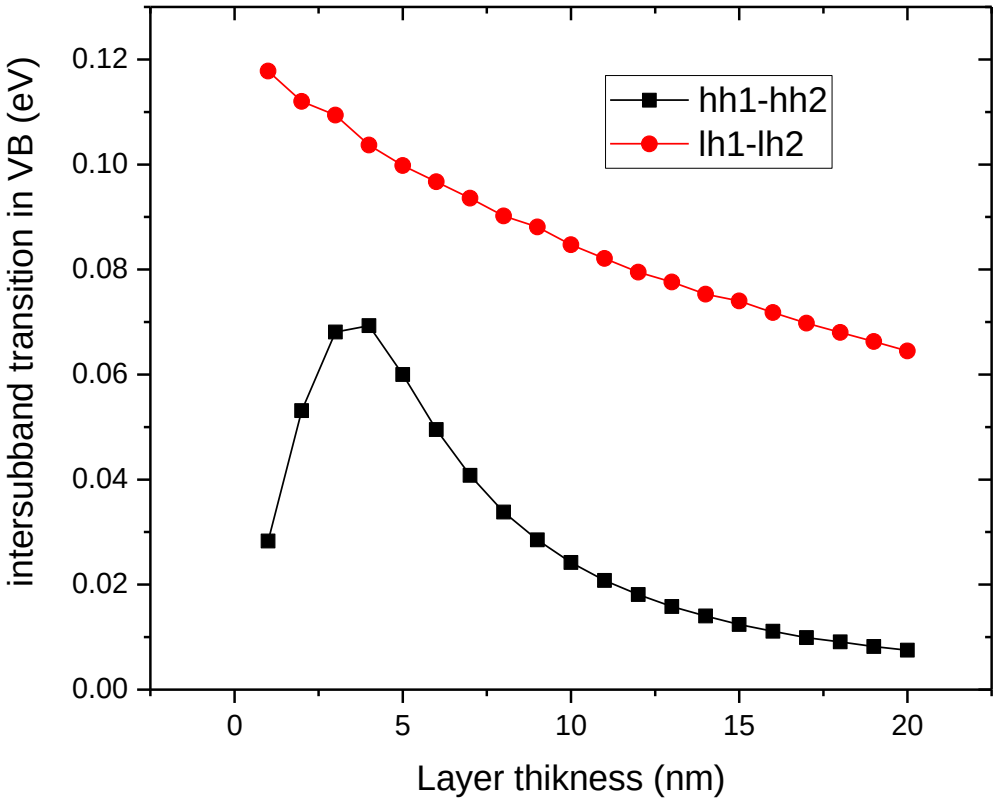

Figure IV.6: Intersubband transitions in valence-confined energies for heavy and light holes as function of barrier thicknesses at 300K.

For Intersubband transitions, heavy hole HH1 to HH2 and light hole LH1 to LH2 produce only z-polarised absorption in the parabolic band approximation [90], HH to LH transitions produced in 3 directions xy and z-polarisation but due to the non-parabolicity of the effective masses of holes the xy-polarization will be reduced significantly because of the confinement in the directions xy and the mixing of sub-band [90].

III.3. Interband transitions in quantum well

During interband transitions electrons migrate from energy levels in the valence band to another energy level in the conduction band. Interband transitions entail electrons moving from an energy level in the VB to another in the CB figure II.9 (chapter II). The energy difference between the initial and final states represents the energy received or released by the photon throughout the transition [91]. As function of width and material qualities of quantum wells dictate their energy levels, adjusting these factors can result a controllable interband transitions. This tunability is very useful in creating optoelectronic devices with specified absorption wavelengths, such as quantum well photodetectors with high rate of photo-absorption [91].

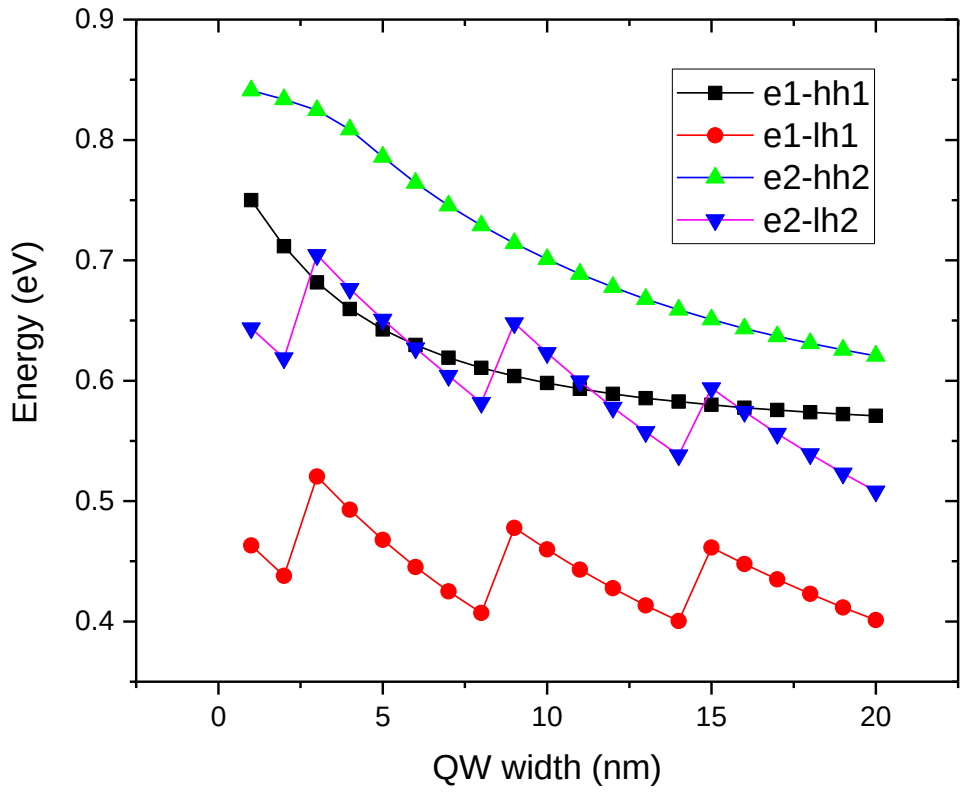

Figure IV.7: Interband transitions between different confined subband states of CB and VB as a function of QW width at 300K.

As described previously many discrete energies states for both electrons and holes are possible. We may presume that by applying the energies of the valence confined state for holes and the conduction confined state for electrons, we can obtain the different transition energies of the QW structure are calculated as shown in figure IV.7.

For widths around 20 nm, the conduction confined states for electrons is therefore nominal around 0,045eV. However, on the valence-confined energies states for light holes is about 0,07eV, but for heavy holes is negligible figure IV.5 and IV.6. The difference between the two cases is 0.025eV, on the other hand by decreasing QW width the difference decreases for QW width up to 5nm, for width less than 5nm electrons undergoes stress caused by the deformation of the mesh of the structure which causes a correlation of sub-band, this stress effect heavy holes too which expresses the variation in the form saw-tooth graph in figure IV.7. for the transition e_1-LH_1 and e_2-LH_2.

IV. Band-edge alignments of cascade superlattice photon-absorber

The band structure of devices presented here comprising 3 and 9 quantum wells with their electron confined states intended to create a cascade of states, as mentioned before it's possible to incorporate many QWs according to their Width, we can also make theme in different stages. Where each Qw or group of Qws formed stage are separated by an optical phonon energy, the "quantum ratchet" section of the device has a new Band structure very different than the material at bulk state. Red lines in figure IV.8 and IV.9 , represent Γ-point band edge, Complete Γ-point structure of the device with a normal p-I-n photodetector formed in the Intrinsic region represent the resonance cavity of photodetectivity formed by type I quantum wells.

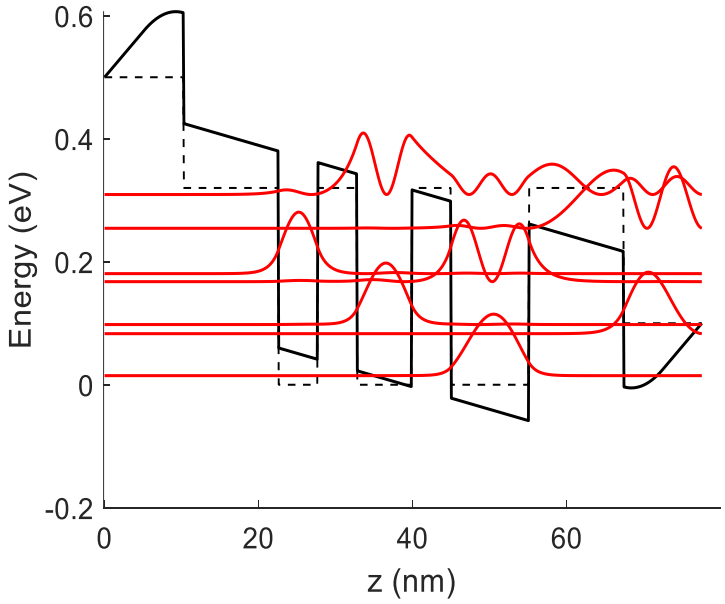

Figure IV.8: Self-consistently calculated conduction band structure of three QC 2D nanostructure with different z and the magnitude squared wave function for each sub bands in active region is illustrated.

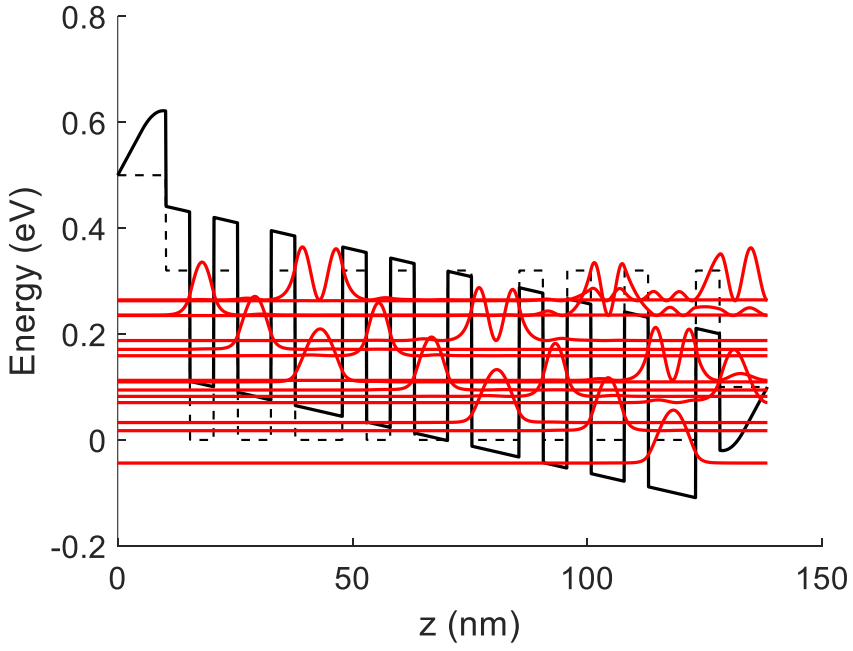

Figure IV.9: Self-consistently calculated conduction band structure of multiple QW of a QC structure for one full period surrounded by adjacent parts of barriere. The observed transitions take place in the active zone; the extraction cascade consists of all possible states.

Figure IV.8 and IV.9. shows the conduction band profile computed with a self-consistent Schrödinger-Poisson solver. The active QW lies at 20 nm and 10nm in the figure IV.8 and IV.9 respectively. Starting from the left barrier, the photocurrent spectrum of the. The photocurrent peaks at 30 meV) and 20 meV, which is in good agreement with the calculated ISB transition energies between level 0 and level 5 respectively 11 of 20 meV and 15 meV. The additional peaks are due to ISB transition into states higher than 6 and 11 respectively. Compared with the results of heterojunction photodetector based on internal photodetection [64 39], those results are about two orders of magnitude lower. However, the QCD is believed to have area for improvement [65 38], especially by increasing the doping density and optimizing the bandstructure for high absorption and escape probability.

V. Relationship between absorption and cell thickness

The intensity of the radiation absorbed by the cell is strongly dependent on the thickness of the cell, and therefore on the thickness of the active area, this is the reason why the number of wells inserted in the active area is limited depending on the thickness of the latter [2].

The optical absorption efficiency as a function of the thickness of the device is given by the relation [pub onera]:

$$\eta_{op} = 1 - exp^{-\alpha W_c} \frac{1}{1+\alpha L_D} \qquad \text{IV.1}$$

α : the absorption coefficient

W_c : the cell thickness

The equation shows the relationship between the absorption coefficient, the thickness of the cell and the diffusion length, hence the term $(1/1 + \alpha L_D)$ represents the absorption recover from the diffusion of carriers.

$$I_s = I_{ph} - I_0\left(e^{qV_m/k_bT} - 1\right) \qquad \text{IV.2}$$

Were

$$I_{ph} = \frac{2\pi q A_{opt}}{h^3 c^2} \int_{E_g}^{\infty} QE_m \left(\frac{E^2}{e^{E/k_bT_{fs}}} - \frac{E^2}{e^{E/k_bT_{bs}}}\right) dE \qquad \text{IV.3}$$

$$QE_m = (1-R)T_{win}e^{-(m-1)\alpha d}QE_d \qquad \text{IV.4}$$

A_{opt} is the optical area of the device, Eg is the bandgap of the absorber, QE_m is the effective quantum efficiency in the N_{th} stage, T_{fs} is the front-side temperature, T_{bs} is the back-side.
Equation IV.2 indicates that the signal current will equal the average of the photocurrents, the overall impact of electrical amplification is to elevate the signal current from the minimum photocurrent in the final stage to the mean photocurrent across all stages.

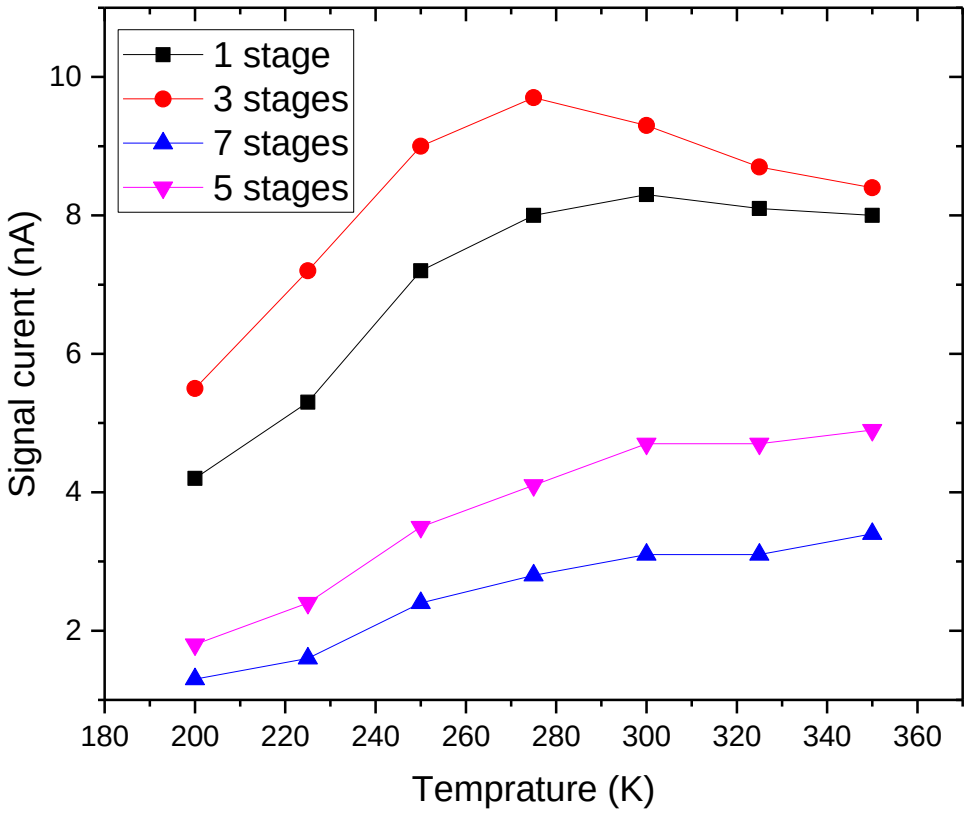

Figure IV.10: Theoretically calculated signal current and photocurrent based on Equation IV.2 as function of width wich is represented by number of stages.

Figure IV.10 illustrates the computed and observed signal currents for the four proposed devices within a temperature range of 200-350 K. considering some flaws and uncertainties in the absorption coefficients equation IV.1, we know that reducing thickness results in an extremely reduced optical path in the active layer, thereby decreasing the amount of light absorbed [95]. To enhance the efficiency of thin TPV, it is essential to optimise absorption in the active zone.

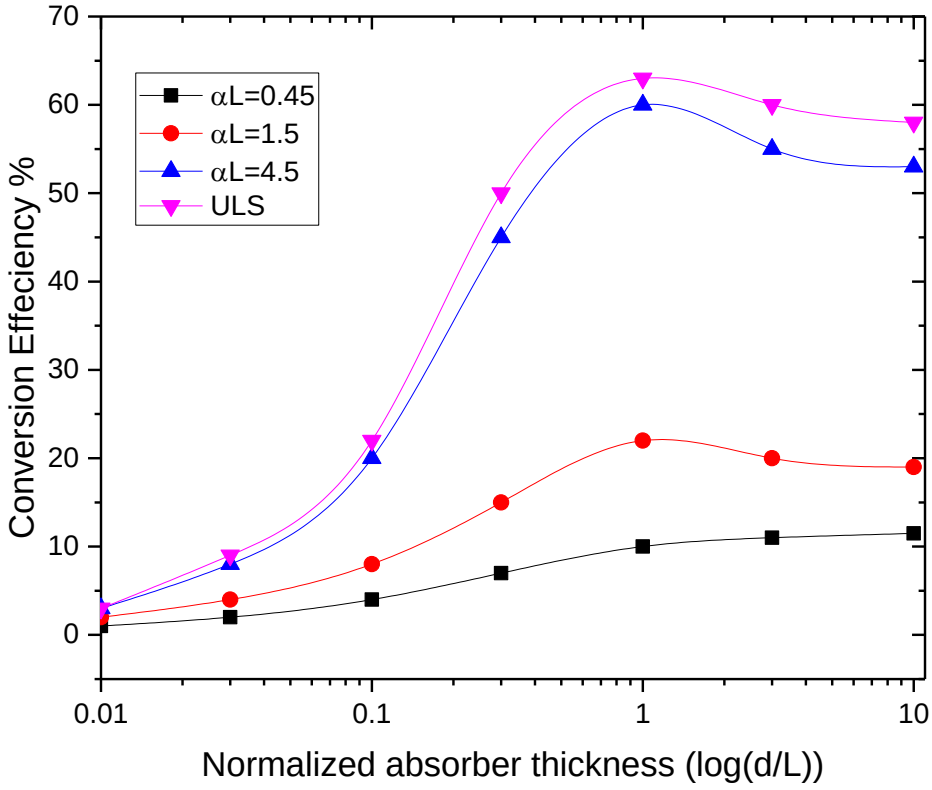

Figure IV.11: Calculated conversion efficiency vs normalized absorber thickness for different values of αL with an incident power density equal 50 W/cm^2.

Figure IV-11 illustrates the conversion efficiency of TPV devices under different conditions. The radiative and ultimate limits state (USL) is nearly identical at small absorber thicknesses, with peak efficiencies of 60% and 65%, respectively. In contrast, practical performance at αL = 0.45 is much lower (<7%) due to short carrier lifetimes (~20 ns), which lead to high J_o, low V_{oc}, and low FF. Improving the carrier lifetime by an order of magnitude could raise efficiency to about 25%. The results highlight that carrier lifetime is the critical limiting factor in narrow bandgap TPV devices, alongside the low quantum efficiency (QE < 32%) caused by small αL. The efficiency trend versus normalized absorber thickness (d/L) mirrors that of QE: it rises to a maximum, then decreases and plateaus. The optimal d/L for maximum efficiency is ~1.7, 1, and 0.7 for αL = 0.45,

1.5, and 4.5, respectively slightly smaller than the optimal d/L for maximum QE because of Voc and FF degradation at larger thicknesses.

VI. The quantum multi-stage PIN cell calculation model

The current density of a PIN junction QC, according to the model given by the relation :

$$J = J_0\left[\exp\left(\frac{qV}{KT}\right) - 1\right] - J_G + J_R \qquad \text{IV.5}$$

J_G and J_R are the generation current and the recombination current corresponds to the absorption coefficient G and to the recombination R calculated in chapter II, they are given by the following relation:

Generation current:

$$J_G = qw\left[G_{op} + G_{th} + A_{cnr}n_i\right]\exp\left(-\frac{qV_d}{KT}\right) \qquad \text{IV.6}$$

Recombination current

$$J_R = qw[G_{th}]\exp\left(-\frac{qV_d}{KT}\right) \qquad \text{IV.7}$$

W : intrinsic zone width, G_{op}: optical generation current, G_{th}: thermal generation current, A_{cnr}: non radiative coefficient generation.

the current density must be higher than that of a classic junction

The current density equation becomes:

$$J = J_0(1+\beta)\left[\exp\left(\frac{qV_d}{KT}\right) - 1\right] + J' - J_{ph} \qquad \text{IV.8}$$

The diffusion voltage V_d is given as a function of the state density of electrons of the conduction band N_C' and of the state density of holes of the valence band N_V' by the following relation:

$$qV_d = E_{g,QW} + KT\ln\left[\exp\left(\frac{n}{N_c}\right) - 1\right]\left[\exp\left(\frac{n}{N'_V}\right) - 1\right] = E_{g,QW} + KT\ln\left[\exp\left(\frac{p}{N'_c}\right) - 1\right]\left[\exp\left(\frac{p}{N_V}\right) - 1\right] \qquad \text{IV.9}$$

In each well the absorption is given by the following relationships:

The photoconductive gain per quantum well is given by:

$$G_{pq} = \frac{\tau_c}{\tau_{tr}} \qquad \text{IV.10}$$

τ_c is the lifetime of the carriers proportional to G_{pq} and τ_{tr} is the transition time. The optical yield per well is given by:

$$\eta_{pq} = p_e \alpha_{pq} \qquad \text{IV.11}$$

p_e is the amount of movement necessary for the carriers to cross the active zone.

$$R = \frac{J_s}{J_{ph}} = \frac{\eta_{pq} G_{pq}}{h\upsilon/q} \qquad \text{IV.12}$$

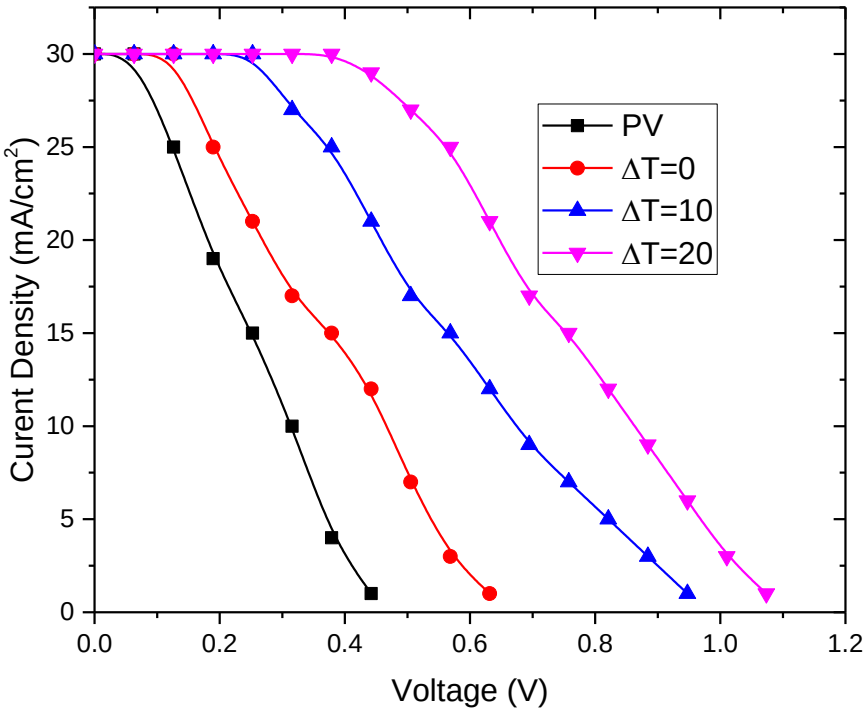

Figure IV.12 : comparison of the J–V characteristics of a conventional PV and TPV under various temperature differences (ΔT).

Figure IV.12 represent a theoretical calculation of the characteristic J-V of conventional PV and hybrid TPV devices in for many three value of ΔT from 0°C, 10°C and 20°C. In addition to J_{sc} of 30 mA/cm2, PV cell produced V_{oc} equal 1.1V, which represent nearly the sum of V_{oc} from PV and

from the high capability of Iph in addition to TE conversion. Voc increases with the TE device in proportionate to ΔT, because of the extra VTE caused by ΔT.

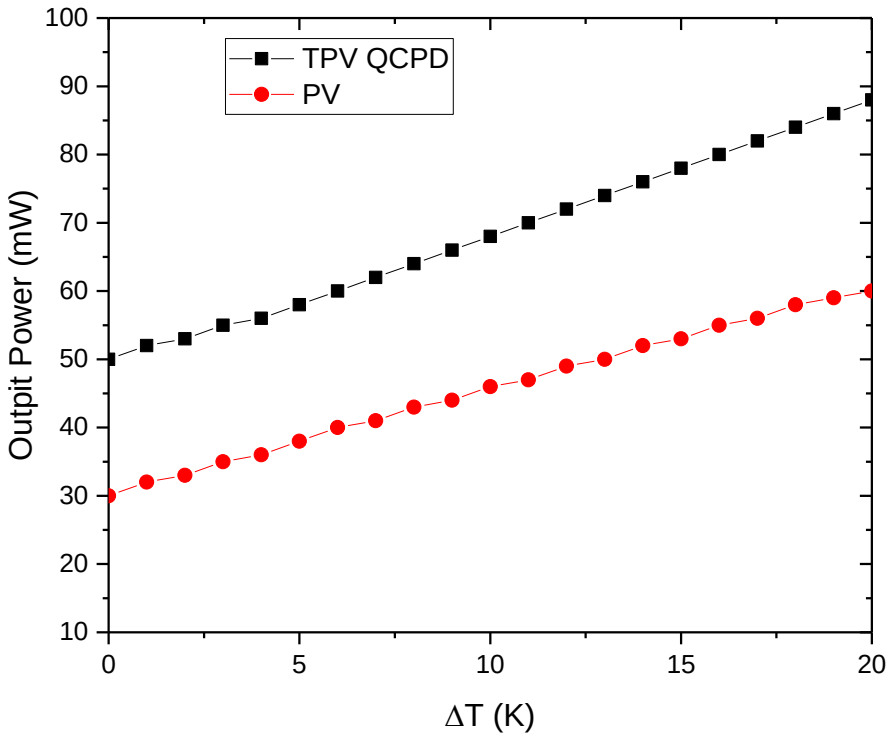

Figure IV.13: The comparison of the calculated output power for a simple summation of the PV and and QCPD's TPV as a function of (ΔT).

Figure IV.13 shows the difference between PV power and QCPD's TPV device determines maximum output power (P_{max}) rather significantly. Remarkably, we investigated the lossless operation condition by separately operated at maximum output conditions by comparing the power of the TPV device with the simple sum of the output values from the individual PV and TE devices. The output power equals the total of maximum power outputs generated separately from the PV and TE devices when ΔT reaches a threshold value, this lossless coupling between PV and TE circuits clearly showed that I_{ph} calculated the total current under the optimal hybrid PV-TE operation.

VII. Conclusion

The model proposed in this study indicates that transport in the detector results from the trading of electrons among bands of thermalised states within the device. For this reason, an approach based on strain compensation in InGaAsSb/ AlGaAsSb type I QW, to obtain long emission wavelength in the mid-infrared. This system emphasizes the intrinsic design compromise between signal and thermal noise. In the state of bulk-like absorbers, the photocurrent and thermal currents derived from their particular-production, which distresses to the design and material characteristics of the absorber. Our model is applicable to QCPDs thermophotovoltaic devices. This QCDs utilized to determine the circumstances technique may surpass single-absorber detectors. specifically, when we utilize multi stages where the electric fields in each stage are restricted to the barrier areas, the multiple stage technique enhance performance by boosting carrier collecting efficiency through assuming the absorbers are appropriately engineered to provide unbroken absorption for the major part of sunlight and collection of carriers at each stage. Finally, we determined an optimal number of stages for detectors within this limit, this consequence indicates that employing many stages facilitates the attainment of highspeed detectors while minimizing the loss of sensitivity compared to a single absorber device.

GENERAL CONCLUSION

GENERAL CONCLUSION

In this PhD thesis, we conducted a comprehensive theoretical investigation into the optimization, modeling, and simulation of a new generation of thermophotovoltaic (TPV) solar cells based on quantum nanostructures. The overarching objective was to enhance the exploitation of solar energy and to facilitate the recovery of waste heat—two energy sources that are abundant, readily accessible, and not subject to the intermittency challenges associated with wind or hydropower. Given the increasing global demand for sustainable energy solutions, maximizing the efficiency of photovoltaic (PV) and thermoelectric (TE) devices has become a strategic priority.

To this end, we explored the synergistic integration of PV and TE technologies as a means of surpassing the conversion efficiency limits of standalone devices. Traditional solar cells suffer from two major energy loss mechanisms: thermalization losses, where excess energy from high-energy photons is dissipated as heat, and transmission losses, where low-energy photons pass through the material without being absorbed. Collectively, these effects lead to a substantial portion of the solar spectrum being converted into heat rather than usable electrical power.

To address these limitations, we proposed the use of quantum cascade photodetectors (QCDs) within TPV architectures—not only to recover the waste heat generated during the photovoltaic process but also to actively extract and convert the infrared (IR) portion of the spectrum that is typically neglected by conventional PV devices. This dual role provides two simultaneous benefits: efficiency enhancement through supplementary energy harvesting, and thermal management by reducing the undesired heat load that degrades PV performance.

A significant part of this work was devoted to identifying and optimizing material platforms and structural designs capable of sustaining room-temperature operation. We demonstrated that III-V semiconductor compounds, already experimentally validated for terrestrial applications, offer a robust foundation for forming quantum wells (QWs), quantum dots (QDs), and superlattice structures with tailored absorption properties. While multiple QWs allow engineering of intermediate bandgaps suitable for IR collection, their fabrication demands precise control over layer thicknesses and interfaces—an aspect we accounted for in our modeling strategy.

We evaluated several quantum nanostructure geometries, showing that the spectral position of absorption bands can be modulated through quantum confinement effects and barrier engineering, allowing near-perfect alignment with the dominant portion of ground-level solar IR radiation. The use of earth-abundant and non-toxic materials was emphasized to ensure technological scalability and environmental compatibility.

In addition to optical simulations, we provided a global overview of mechanical, thermal, and electrical performance constraints associated with these devices, highlighting practical considerations for future fabrication. Our results validate the proposed architecture as a promising path toward high-efficiency, multi-functional TPV systems capable of harvesting both photonic and thermal energy.

In conclusion, this thesis confirms that quantum nanostructure–based TPV devices represent a viable and forward-looking solution to the dual challenge of energy efficiency and sustainability. By recovering energy that is traditionally lost and re-injecting it into the conversion process, such hybrid systems pave the way toward greener, smarter, and more resilient power generation technologies. In the broader context of global energy scarcity, any advancement that contributes to more efficient harvesting of naturally available energy sources is not only scientifically relevant but also of profound societal importance.

Perspective

The development of hybrid quantum nanostructured thermo-photovoltaic (TPV) systems offers a compelling pathway toward sustainable energy conversion. Traditional energy sources still rely heavily on fossil fuels, leading to massive heat losses into the environment—more than 60% of industrial energy is dissipated as unused thermal waste. By engineering TPV devices capable of harvesting and converting this wasted heat into clean electricity, the present work contributes to a technology that directly addresses one of the most urgent challenges of our time: reducing greenhouse gas emissions and global warming.

By integrating low band-gap antimonide absorbers with the tailored electronic properties of III–V semiconductor nanostructures, this approach enables broadband photon harvesting and efficient thermal-to-electrical conversion within a single platform. Beyond the demonstrated enhancement in optoelectronic response, the proposed architecture overlays the way for new

multifunctional TPV systems capable of operating under high thermal loads while maintaining spectral selectivity and conversion efficiency. Looking forward, several research directions emerge. Optimizing the geometry and arrangement of quantum dots, wires, and wells may further improve carrier mobility and reduce thermal losses. Coupling these nanostructured absorbers with selective thermal emitters or photonic cavities could lead to unprecedented control over photon recycling and spectral filtering. Additionally, integrating thermoelectric modules or heat-management layers may provide a new class of hybrid TPV/TE devices capable of simultaneously harvesting radiative and conductive heat. Ultimately, the advances presented in this work establish a strong foundation for next-generation energy systems that are compact, highly efficient, and suitable for a wide range of applications—from industrial waste-heat harvesting to portable energy sources and space technologies. As materials engineering and nanofabrication techniques continue to evolve, hybrid quantum TPVs have the potential to become an unruly technology in the transition toward cleaner, smarter, and sustainable energy infrastructures.

BIBLIOGRAPHY

Bibliography

[01] G. J. Snyder and T. S. Ursell, 'Thermoelectric Efficiency and Compatibility', Phys. Rev. Lett., vol. 91, no. 14, Oct. 2003. https://doi.org/10.1103/PhysRevLett.91.148301

[02] Asokendu Mozumder, Milton Burton et all, Radiation, encyclopaedia Britannica feb 5, 2025 website https://www.britannica.com/science/radiation

[03] E.Okuno J. R. Cunningham and D. R. Dance, Interactions of Radiation with Matter Diagnostic Radiology Physics: A Handbook for Teachers and Students IAEA publication (ISBN 978-92-0-131010-1) 2024.

[04] Ran Liu, Yufei Ge, Dong Wang and Zhigang Shuai, Understanding the Temperature Dependence of the Seebeck Coefficient from First-Principles Band Structure Calculations for Organic Thermoelectric Materials, Journal of Chinese Chemical Society. 2021, 3, 1477–1483 https://doi.org/10.31635/ccschem.021.202100813.

[5] Pablo Arturo Fernandez Garrillo, Development of highly resolved and photo-modulated Kelvin probe microscopy techniques for the study of photovoltaic systems, phd dessertetion 31 Jan 2019.

[06] R.A. EDWARDS, CHAPTER 17 - Thermal Radiation, Physics for O.N.C. Courses, Pages 277-302, 1970. ISBN 9780080134314, https://doi.org/10.1016/B978-0-08-013431-4.50021-0.

[07] K. Dhar, R. Dat, A. K. Sood, "Advances in Infrared Detector Array Technology," IntechOpen, 2012.

[08] B. Lenoir, J.-P. Michenaud, and A. Dauscher. Thermoélectricité : des principes aux applications. Techniques de l'ingénieur, 33(0) :K 730, 2010.

[09] S. LeBlanc, S. K. Yee, M. L. Scullin, C. Dames, and K. E. Goodson. Material and manufacturing cost considerations for thermoelectrics. Renewable and Sustainable Energy Reviews, 32 :313–327, 2014.

[10] Bo Brummerstedt, Iversen, Jacob Becker, Kasper Andersen Borup, Termoelektriske, Aktuel Naturvidenskab, (2014), https://aktuelnaturvidenskab.dk/fileadmin/Aktuel_Naturvidenskab/nr-1/AN1-2014termoel.pdf

[11] H Julian Goldsmid. The Seebeck and Peltier effects. The Physics of Thermo-electric Energy Conversion, pages 2053{2571, 2017.

[12] TJ Seebeck. The magnetic polarization of metals and ores produced by temperature difference. Proceedings. of Prussian Academy of Sciences, pages 265{373, 1822.

[13] Jia, N., Cao, J., Tan, X. Y., Dong, J., Liu, H., Tan, C. K. I., … Suwardi, A. (2021). Thermoelectric materials and transport physics. Materials Today Physics, 21, 100519. doi:10.1016/j.mtphys.2021.100519

[14] Zhe Ma, Jiangtao Wei, Peishuai Song, Mingliang Zhang, Liangliang Yang, Jing Ma, Wen Liu, Fuhua Yang, Xiaodong Wang, Review of experimental approaches for improving zT of thermoelectric materials, Materials Science in Semiconductor Processing, Volume 121, 2021, 105303, ISSN 1369-8001, https://doi.org/10.1016/j.mssp.2020.105303.

[15] B. Lenoir, J.-P. Michenaud, and A. Dauscher. Thermoélectricité : des principes aux applications. Techniques de l'ingénieur, 33(0) :K 730, 2010

[16] L. M. Fraas, J. E. Avery, H. X. Huang, R. U. Martinelli, "Thermophotovoltaic system configurations and spectral control," Semiconductor Science and Technology, 18, pp. 165–173, 2003

[17] JCA Peltier. New experiments on the heat effects of electric currents. Ann. Chim. Phys, 56:371{386, 1834.

[18] G. D. Mahan and J. O. Sofo, 'The best thermoelectric', Proc. Natl. Acad. Sci., vol. 93, no. 15, pp. 7436–7439, 1996.

[19] A. Sharma, J. Hyeong Lee, K. Heum Kim and Jae Pil Jung, Recent Advances in Thermoelectric Power Generation Technology, journal of Microelectron, 24(1), 9-16 (2017) https://doi.org/10.6117/kmeps.2017.24.1.009

[20]L. Han, T. Xin-Feng, C. Wei-Qiang, and Z. Qing-Jie. Quick preparation and thermal transport properties of nanostructured -FeSi2 bulk material. Chinese Physics B, 18(1) :287–292, 2009.

[21] F. F. Jaldurgam, Z. Ahmad, and F. Touati. Low-toxic, earth-abundant nanostructured materials for thermoelectric applications. Nanomaterials, 11(4) :1–25, 2021.

[22] X. Yan, S. Zheng, Z. Zhou, H. Wu, B. Zhang, Y. Huang, X. Lu, G. Han, G. Wang, and X. Zhou. Melt-spun Sn1−x−ySbxMnyTe with unique multiscale microstructures approaching exceptional average thermoelectric zT. Nano Energy, 84(February), 2021

[23] L. Hu, H. Wu, T. Zhu, C. Fu, J. He, P. Ying, and X. Zhao. Tuning Multiscale Microstructures to Enhance Thermoelectric Performance of n-Type BismuthTelluride-Based Solid Solutions. Advanced Energy Materials, 5(17), 2015.

[24] O. Cherniushok, T. Parashchuk, J. Tobola, S. D.N. Luu, A. Pogodin, O. Kokhan, I. Studenyak, I. Barchiy, M. Piasecki, and K. T. Wojciechowski. EntropyInduced Multivalley Band Structures Improve Thermoelectric Performance in p-Cu7P(SxSe1−x)6 argyrodites. ACS Applied Materials and Interfaces, 13(33) :39606–39620, 2021.

[28] N. F. Hinsche, B. Yu. Yavorsky, M. Gradhand,M. Czerner, M. Winkler, J. K¨onig, H. B¨ottner, I. Mertig, and P. Zahn, Thermoelectric transport in Bi2Te3/Sb2Te3 superlattices, Condensed Matter, 18 Jun 2012, https://doi.org/10.48550/arXiv.1206.4078

[29] T. Fu et al., 'Enhanced thermoelectric performance of PbTe bulk materials with figure of merit zT >2 by multi-functional alloying', J. Materiomics, vol. 2, no. 2, pp. 141–149, Jun.2016

[30] K. F. Hsu, S. Loo, F. Guo, W. Chen, J. S. Dyck, C. Uher, T.Hogan, E. K. Polychroniadis, and M. G. Kanatzidis. CubicAgPb(m)SbTe(2þm): Bulk Thermoelectric Materials withHigh Figure of Merit. Science 2004,303, pp 818–821.

[31] H. J. Goldsmid, A. R. Sheard, and D. A. Wright. The Per-formance of Bismuth Telluride Thermojunctions. Br. J. Appl.Phys. 1958,9, pp 365–370.

[32] T. C. Harman, D. L. Spears, and M. J. Manfra. HighThermoelectric Figures of Merit in PbTe Quantum Wells.J. Electron. Mater. 1996,25, pp 1121–1127.

[33] D.-Y. Chung, T. Hogan, P. Brazis, M. Rocci-Lane, C.Kannewurf, M. Bastea, C. Uher, and M. G. Kanatzidis.CsBi(4)Te(6): A High-Performance Thermoelectric Materialfor Low-Temperature Applications. Science 2000,287,pp 1024–1027.

[34] A.I.Boukai,Y.Bunimovich,J.Tahir-Kheli,J.K.Yu,W.A.Goddard, and J. R. Heath. Silicon Nanowires asEfficient Thermoelectric Materials. Nature 2008,451,pp168–171

[35] A. I. Hochbaum, R. K. Chen, R. D. Delgado, W. J. Liang, E. C.Garnett, M. Najarian, A. Majumdar, and P. D. Yang.Enhanced Thermoelectric Performance of Rough SiliconNanowires. Nature 2008,451, pp 163–167.

[36] B. Poudel, Q. Hao, Y. Ma, Y. C. Lan, A. Minnich, B. Yu,X. Yan, D. Z. Wang, A. Muto, D. Vashaee, X. Y. Chen,J. M. Liu, M. S. Dresselhaus, G. Chen, and Z. Ren. High-Thermoelectric Performance of Nanostructured BismuthAntimony Telluride Bulk Alloys. Science 2008,320,pp 634–638.

[37] P. F. P. Poudeu, J. D'Angelo, A. D. Downey, J. L. Short,T. P. Hogan, and M. G. Kanatzidis. High ThermoelectricFigure of Merit and Nanostructuring in Bulk p-type Na1-xPbmSbyTem+2. Angew.Chem.Int. thermoelectric materials, 2006, DOI: 10.1002/anie.200600865

[38] J.-S. Rhyee, K. H. Lee, S. M. Lee, E. Cho, S. I. Kim, E. Lee,Y. S. Kwon, J. H. Shim, and G. Kotliar. Peierls Distortion as aRoute to High Thermoelectric Performance in In4Se3 □dCrystals. Nature 2009,459, pp 965–968.

[39] J. P. Heremans, V. Jovovic, E. S. Toberer, A. Saramat, K.Kurosaki, A. Charoenphakdee, S. Yamanaka, and G. J.Snyder. Enhancement of Thermoelectric Efficiency inPbTe by Distortion of the Electronic Density of States.Science 2008,321, pp 554–557.

[40] A. Saramat, G. Svensson, A. E. C. Palmqvist, C. Stiewe, E.Mueller, D. Platzek, S. G. K. Williams, D. M. Rowe, J. D.Bryan, and G. D. Stucky. Large Thermoelectric Figure ofMerit at High Temperature in Czochralski-Grown ClathrateBa8Ga16Ge30.J. Appl. Phys. 2006,99, pp 023708

[41] X. W. Wang, H. Lee, Y. C. Lan, G. H. Zhu, G. Joshi, D. Z.Wang, J. Yang, A. J. Muto, M. Y. Tang, J. Klatsky, S. Song,M. S. Dresselhaus, G. Chen, and Z. F. Ren. EnhancedThermoelectric Figure of Merit in Nanostructured n-Type Si-Ge Bulk Alloy. Appl. Phys. Lett. 2008,93,pp 193121.

[42] E. K. Lee, L. Yin, Y. Lee, J. W. Lee, S. J. Lee, J. Lee, S. N. Cha,D. Whang, G. S. Hwang, K. Hippalgaonkar, A. Majumdar, C.Yu, B. L. Choi, J. M. Kim, and K. Kim. Large Thermoelectric Figure-of-Merits from SiGe Nanowires by Simultaneously Measuring Electrical and Thermal Transport Properties.Nano Lett.2012,12, pp 2918–2923

[43] A. Sharma, J. Hyeong Lee, K. Heum Kim and Jae Pil Jung, Recent Advances in Thermoelectric Power Generation Technology, journal of Microelectron, 24(1), 9-16 (2017) https://doi.org/10.6117/kmeps.2017.24.1.009

[44] Bharti Gurunani, Dinesh C. Gupta, Half-metallicity and thermoelectric performance: A multifaceted investigation of Zr-based half-Heusler alloys, Materials Science and Engineering: B Volume 311, January 2025. https://doi.org/10.1016/j.mseb.2024.117783

[45] Kwang Yong LeeKwang Yong LeeTae Sung Oh, P-Type and N-Type Bi2Te3/PbTe Functional Gradient Materials for Thermoelectric Power Generation, Materials Science, January 2007. DOI: 10.4028/www.scientific.net/MSF.534-536.1493

[46] M. Khalil, A. Moll, M. Godfroy, A. Letrouit-Lebranchu, B. Villeroy, E. Alleno, R. Viennois, and M. Beaudhuin. Thermoelectric properties and stability of nanostructured chromium disilicide CrSi2. Journal of Applied Physics, 126(13), 2019.

[47] Svenja Mauthe, Yannick Baumgartner, Marilyne Sousa, Qian Ding, Marta D. Rossell, Andreas Schenk, Lukas Czornomaz & Kirsten E. Moselund, High-speed III-V nanowire photodetector monolithically integrated on Si, Nature Communications volume 11, Article number: 4565 (2020) https://doi.org/10.1038/s41467-020-18374-z

[49] https://www.nist.gov/image/quantumdotsjpg-0

[50] A. M. Rao, X. Ji, X and T. M.Tritt, Properties of Nanostructured One-Dimensional and Composite Thermoelectric Materials, J. MRS Bulletin, January 2011.

[51] A. Shakouri, Recent Developments in Semiconductor Thermoelectric Physics and Materials ,J. Annual Review of Materials Research, (2011).

[52] “A unified understanding of minimum lattice thermal conductivity”, Xia, Y.; Gaines Ii, D.; He, J. G.; Pal, K.; Li, Z.; Kanatzidis, M. G.; Ozolins, V.; Wolverton, C., Proceedings of the National Academy of Sciences of the United States of America 2023, 120 (26). DOI: 10.1073/pnas.2302541120.

[53] R. Venkatasubramanian, E. Siivola, T. Colpitts, and B. O'Quinn, Thin-film thermoelectric devices with high room-temperature figures of merit, Journal of Nature, 413, (2001).

[54] T. C. Harman, P. J. Taylor, M. P. Walsh, et B. E. LaForge, Quantum Dot Superlattice Thermoelectric Materials and Devices, Journal of Science, 297, (2002).

[55] B. Poudel, Q. Hao, Y. Ma, Y. Lan, A. Minnich, B. Yu, X. Yan, D. Wang, A. Muto, D. Vashaee, X. Chen, J. Liu, M. S. Dresselhaus, G. Chen, and Z. Ren, High-Thermoelectric Performance of Nanostructured Bismuth Antimony Telluride Bulk Alloys, J. Science, 320, 34-638 (2008). DOI:10.1126/science.1156446

[56] R. Venkatasubramanian, E. Siivola, et B. O'Quinn, "Thermoelectrics Handbook: macro to nano", CRC/Taylor & Francis, 49.1-49.15 (2006).

[57] D. G. Cahill, W. K. Ford, K. E. Goodson, G. D. Mahan, A. Majumdar, H. J. Maris, R. Merlin, S. R. Phillpot, Nanoscale thermal transport, J. Applied Physics, 93, (2003) https://doi.org/10.1063/1.1524305

[58] M. Kurkaa, M. Dyksika, S. Suomalainenb, E. Koivusalob, M. Guinab, M. Motykaa, GaInAsSb/AlGa(In)AsSb type I quantum wells emitting in 3 μm range for application in super luminescent diodes, Optical Materials 91 274–278 (2019).

[59] Sangmo Kim, Hoang Van Quy, Daegu Gyeongbuk, and Chung Wung Bark, Silicon-Based Technologies for Flexible Photovoltaic (PV) Devices: From Basic Mechanism to Manufacturing Technologies journal of Nanomaterials, November 202111(11):2944, DOI:10.3390/nano11112944

[60] A. Yoshizawa, H. Tsuchida, A 1550 nm Single-Photon Detector Using a Thermoelectrically Cooled InGaAs Avalanche Photodiode, Japanese Journal of Applied Physics, 40, 2001

[61] J. Yin, R. Paiella, "Limiting performance analysis of cascaded interband/intersubband thermophotovoltaic devices," Applied Physics Letters, 98, p. 041103, (2011).

[62] A. Rogalski, P. Martyniuk, M. Kopytko, "InAs/GaSb type-II superlattice infrared detectors: Future prospect," Applied Physics Reviews, 4, p. 031304, (2017).

[63] A. Delga, Quantum cascade detectors: A review, Mid-infrared Optoelectronics, Materials Devices and Applications, Woodhead Publishing Series in Electronic and Optical Materials, P337-377, 2020. https://doi.org/10.1016/B978-0-08-102709-7.00008-5

[63] C. A. Wang, H. K. Choi, S. L. Ransom, G. W. Charache, L. R. Danielson, D. M. DePoy, “High-quantum-efficiency 0.5 eV GaInAsSb/GaSb thermophotovoltaic devices,” Applied Physics Letters, 75, p. 1305, (1999).

[64] D. Cakiroglu, J. Perez, A. Evirgen, C. Lucchesi, P. Chapuis, T. Taliercio, E. Tournié, R. Vaillon, “Indium antimonide photovoltaic cells for near-field thermophotovoltaics,” Solar Energy Materials and Solar Cells, 203, p. 110190, (2019).

[65] Aslı Çakan, Cem Sevik and Ceyhun Bulutay Strained band edge characteristics from hybrid density functional theory and empirical pseudopotentials: GaAs, GaSb, InAs and InSb Journal of Physics D: Applied Physics 49(8):085104, January (2016) DOI:10.1088/0022-3727/49/8/085104

[66] A. Krier, M. Yin, A.R.J. Marshall, and S.E. Krier, “Low Bandgap InAs-Based Thermophotovoltaic Cells for Heat-Electricity Conversion”, Journal of Electronic Materials, 45, p. 2826, (2016).

[67] Q. Lu, X. Zhou, A. Krysa, A. Marshall, P. Carrington, C-H. Tan, A. Krier, “InAs thermophotovoltaic cells with high quantum efficiency for waste heat recovery applications below 1000 °C”, Solar Energy Materials and Solar Cells, 179, p. 334, (2018).

[68] P. Dutta, J. Borrego, H. Ehsani, G. Rajagopalan, I. Bhat, R. Gutmann, et al., "GaSb and Ga1-xInxSb thermophotovoltaic cells using diffused junction technology in bulk substrates," Fifth Conference on Thermophotovoltaic Generation of Electricity, pp. 392-401, (2003).

[69] O. V. Sulima, A. W. Bett, “Fabrication and simulation of GaSb thermophotovoltaic cells,” Solar Energy Materials and Solar Cells. 66, pp. 533-540, 2001.

[70] R. S. Tuley, J. M. S. Orr, R. J. Nicholas, D. C. Rogers, P. J. Cannard, S. Dosanjh, “Lattice-matched InGaAs on InP thermophotovoltaic cells,” Semiconductor Science and Technology, 28, p. 015013, 2012.

[71] P. Dutta, J. Borrego, H. Ehsani, G. Rajagopalan, I. Bhat, R. Gutmann, et al., "GaSb and Ga1-xInxSb thermophotovoltaic cells using diffused junction technology in bulk substrates," Fifth Conference on Thermophotovoltaic Generation of Electricity, pp. 392-401, 2003.

[72] M. Mauk, O. Sulima, J. Cox, R. Mueller, “Low-bandgap (0.3 to 0.5 eV) InAsSbP thermophotovoltaics: assessment for open-circuit voltage improvements,” 3rd World Conference on Photovoltaic Energy Conversion, 2003.

[73] A. Krier, M. Yin, A.R.J. Marshall, and S.E. Krier, “Low Bandgap InAs-Based Thermophotovoltaic Cells for Heat-Electricity Conversion”, Journal of Electronic Materials, 45, p. 2826, 2016.

[74] C. A. Wang, H. K. Choi, S. L. Ransom, G. W. Charache, L. R. Danielson, D. M. DePoy, “High-quantum-efficiency 0.5 eV GaInAsSb/GaSb thermophotovoltaic devices,” Applied Physics Letters, 75, p. 1305, 1999.

[75] R. M. Swanson, “Silicon photovoltaic cells in thermophotovoltaic energy conversion,” 1978 International Electron Devices Meeting, pp. 70-73, 1978.

[76] M. Shtern, A. Sherchenkov et al, Mechanical properties and thermal stability of nanostructured thermoelectric materials on the basis of PbTe and GeTe, Journal of Alloys and Compounds Volume 946, 15 June 2023, https://doi.org/10.1016/j.jallcom.2023.169364

[77] S. Kotamraju, M. Sukeerthi, S.E. Puthanveettil, Modeling of InGaP/InGaAs-GaAsP/ Ge multiple quantum well solar cell to improve efficiency for space applications, Sol. Energy 186 (2019) 328–334.

[78] M. Sukeerthi, Siva Kotamraju, Trap and carrier removal study of 4J InGaP/InGaAs-GaAsP MQW/InGaAsNSb/Ge high efficient space solar cell using advanced physical models, journal of Physica E: Low-dimensional Systems and Nanostructures, Volume 134, October 2021, 114914

[79] C.I. Cabrera, J.C. Rimada, J.P. Connolly, L. Hernandez, Modelling of GaAsP/InGaAs/GaAs strain-balanced multiple-quantum well solar cells, J. Appl. Phys. 113(2) (2013), 024512.

[80] K. Mamic, A. Bainbridge, et al, InGaAsSb for cut-off tuned SWIR detectors, Quantum Sensing and Nano Electronics and Photonics, Proceedings Volume 12430, 15 March 2023, https://doi.org/10.1117/12.2650772

[81] Chanon Pornrungroj, Virgil Andrei,and Erwin Reisner, Thermoelectric–Photoelectrochemical Water Splitting under Concentrated Solar Irradiation, Journal of the American Chemical society. juin 2023 145(25): 13709–13714, doi: 10.1021/jacs.3c01892

[82] Srabanti Ghosh, Dipendu Sarkar, Sweta Bastia and Yatendra S. Chaudhary, Band-structure tunability via the modulation of excitons in semiconductor nanostructures: manifestation in photocatalytic fuel generation, Royal scociety of chemistry, 15, 10939-10974, mai 2023. DOI: 10.1039/D3NR02116E

[83] Courel, Maykel; Rimada, Julio C; Hernàndez, Luis, GaAs/GaInNAs quantum well and superlattice solar cell. Applied Physics Letters, 100(7), 73508–0 (2012).

[84] S.M. Hubbard, C. Cress, C. Bailey, R. Raffaelle, S. Bailey, D. Wilt, Effect of Strain Compensation on Quantum Dot Enhanced GaAs, Solar Cells Appl. Phys. Lett. 92, 123512 (2008)

[85] Jie Chen, Fengwei Chen et all, Broadband Response and a Transformation between Dual- and Single-Wavelength Detection in Coupled Doped-Well Quantum Cascade Detector, journal of advanced electronic materials May 2023 https://doi.org/10.1002/aelm.202300084

[86] J. B. Héroux, C. W. Pei, and W. I. Wanga, Epitaxial growth of InGaAsSb/AlGaAsSb heterostructures for mid-infrared lasers based on strain engineering, Journal of Vacuum Science & Technology B 22, 2240 (2004).

[87] T. Unuma, M. Yoshita, T. Noda, H. Sakaki, H. Akiyama, Intersubband absorption linewidth in GaAs quantum wells due to scattering by interface roughness, phonons, alloy disorder, and impurities, Journal of Applied Physics 93 (3) (2003).

[88] I.Vurgaftman, J. R. Meyer, L. R. Ram-Mohan, journal of applied physics., Vol 89, No 11, 1 june (2001).

[89] A. Haddadi, G. Chen, R. Chevallier, A. M. Hoang, and M. Razeghi, InAs/InAs12xSbx type-II superlattices for high performance long wavelength infrared detection, APPLIED PHYSICS LETTERS 105, 121104 (2014).

[90] S. Adachi, Properties of Semiconductor Alloys: Group-IV, III–V and II–VI Semiconductors, John Wiley & Sons, Ltd. ISBN: 978-0-470-74369-0 (2009).

[91] J. B. He´ roux, C. W. Pei, and W. I. Wanga, Epitaxial growth of InGaAsSb/AlGaAsSb heterostructures for mid-infrared lasers based on strain engineering, Journal of Vacuum Science & Technology B 22, 2240 (2004).

[92] Jianbo Yu, Wenzhe Yao, Min Qiu and Qiang Li, Free-space high-Q nanophotonics, Light: Science & Applications (2025), https://doi.org/10.1038/s41377-025-01825-x

[93] R.R. Lunt, T.P. Osedach, P.R. Brown, J.A. Rowehl, V. Bulovi´c, Practical roadmap and limits to nanostructured photovoltaics, Adv. Mater. 23 (2011) https://doi.org/10.1002/adma.201103404.

[94] Chikara Onodera, Masaaki Yoshida, Effect of Dielectric Mismatch on Exciton Binding Energy in ZnS/MgxZn1−xS Quantum Wells, e-Journal of Surface Science and Nanotechnology 10 April (2010).

[95] H. Heidarzadeh, A. Rostami, S. Matloub, M. Dolatyari, G. Rostami, Analysis of the light trapping effect on the performance of silicon-based solar cells: absorption enhancement, journal of Appl Opt. 54 (2015). https://doi.org/10.1364/ao.54.003591.